Numerical Study of Droplet Impingement on Surfaces with Micro-scale Structures

Zhicheng Yuan

Numerical Study of Droplet Impingement on Surfaces with Micro-scale Structures

Zhicheng YUAN

A thesis submitted to Kyoto University
for the degree of Doctor of Engineering

2021

Acknowledgments

The research described in this thesis was carried out in the Department of Mechanical Engineering and Science, Graduate School of Engineering, Kyoto University under the supervision of Professor Ryoichi Kurose.

First, and most importantly, the author would like to express his heartfelt gratitude to Professor Ryoichi Kurose, whose continuous support, patient guidance, and valuable suggestions greatly helped him complete his studies at Kyoto University.

The author is also deeply grateful to Professor Mitsuhiro Matsumoto, Professor Hiroshi Iwai, and Professor Hideshi Hanazaki for their valuable and critical comments regarding his research.

The author would also like to show his appreciation to Dr. Naohisa Takagaki for the helpful discussions and suggestions.

In addition, the author would like to express his gratitude to Dr. Hu Yong, Dr. Abhishek Pillai, Mr. Wen Jian, Mr. Reo Kai, and Mr. Jun Nagao for their help with his research.

The author also extends his gratitude toward the wonderful members of the Thermal Science and Engineering Laboratory.

This work was partially supported by MEXT as a "Program for Promoting Researches on the Supercomputer Fugaku" (Digital Twins of Real World's Clean Energy Systems with Integrated Utilization of Super-simulation and AI). The author is also grateful to the China Scholarship Council (Project No. 20180260270) for its support.

Finally, the author would like to express his deepest appreciation to his parents, friends, relatives, and girlfriend for their infinite support and constant affection.

Contents

1 Introduction **1**

1.1 Background and motivation 1

1.2 Thesis outline 7

References 9

2 Numerical method and validation **17**

2.1 Introduction 17

2.2 Methodology 18

2.2.1 Governing equations 18

2.2.2 CLSVOF interface capturing scheme 19

2.2.2.1 VOF method 19

2.2.2.2 Level-set method 23

2.2.3 Surface tension 24

2.2.4 Contact angle implementation 25

2.2.5 Numerical procedure 29

2.3 Numerical validation 30

2.3.1 Domain size and grid independence study 30

2.3.1.1 Domain size validation 30

2.3.1.2 Grid independence examination 33

2.3.2 Comparison with experiment 34

2.3.2.1 Contact angle model validation 34

2.3.2.2 Droplet impinging on textured surfaces 35

2.3.3 Accuracy of the simulation 38
2.4 Conclusions 40
References 41

3 Enhancing the surface hydrophobicity by introducing micro-scale structures 47
3.1 Introduction 47
3.2 Problem statement 49
3.3 Results and discussion 50
3.3.1 Droplet shape comparison 50
3.3.2 Wetting state 52
3.3.3 Spreading factor 54
3.3.3.1 Groove width effect 54
3.3.3.2 Impact velocity effect 55
3.3.4 Contact time 56
3.3.5 Phase diagram 57
3.4 Conclusions 60
References 61

4 Manipulating the rebound direction of a droplet by surfaces with roughness gradient 65
4.1 Introduction 65
4.2 Problem statement 68
4.3 Results and discussion 70
4.3.1 Effect of Weber number 70
4.3.2 Effect of groove depth 77
4.3.3 Effect of groove width 79
4.3.4 Phase diagram 81
4.4 Conclusions 83
References 84

5 Suppressing the Cassie-to-Wenzel transition using surfaces with hierarchical structures 89

5.1 Introduction . . . 89

5.2 Problem statement . . . 92

5.3 Results and discussion . . . 94

5.3.1 Effect of secondary structure . . . 94

5.3.2 Effect of impingement center . . . 98

5.3.3 Effect of Weber number . . . 100

5.3.4 Theoretical analysis . . . 103

5.4 Conclusions . . . 109

References . . . 110

6 Stabilizing the Cassie state using surfaces with multiple holes 115

6.1 Introduction . . . 115

6.2 Problem statement . . . 118

6.3 Results and discussion . . . 122

6.3.1 Wetting state . . . 122

6.3.2 Pressure analysis . . . 127

6.3.3 Larger We effect . . . 131

6.3.4 Theoretical formulation of the maximum spreading factor . . . 133

6.4 Conclusions . . . 138

References . . . 139

7 Conclusions 147

7.1 Summary . . . 147

7.2 Suggestions for future research . . . 151

Chapter 1

Introduction

1.1 Background and motivation

The impingement of droplets on solid surfaces is a ubiquitous phenomenon in nature and the fields of engineering, including the falling raindrops [1], spray flames [2], and ink-jet printing [3]. Under the influence of numerous factors (e.g., the impingement velocity, droplet diameter, and surface wettability), the possible outcomes of droplet impingement on a dry solid surface are spreading, rebounding, fingering, and splashing [4]. Among these factors, the surface wettability (quantified by the contact angle) is most influential, which is controlled by the surface−free energy and geometric structures. The surface−free energy quantifies the disruption of intermolecular bonds that occurs when a surface is created. This is also called surface energy or interfacial−free energy. Surfaces with a low surface−free energy, or so-called hydrophobic surfaces (with a contact angle of larger than 90°), have attracted widespread attention owing to their promising applications, such as self-cleaning [5], anti-icing [6], drop-wise condensation [7], and drag reduction [8]. Many artificial hydrophobic surfaces have been fabricated by employing chemical coatings. However, such surfaces face challenges in terms of robustness and durability because the chemical layers are inevitably abraded or eroded in engineering projects, thus leading to a loss of surface hydrophobicity [9, 10]. Inspired by superhydrophobic surfaces in nature, such as the lotus leaf shown in Fig.1.1(a) and the butterfly

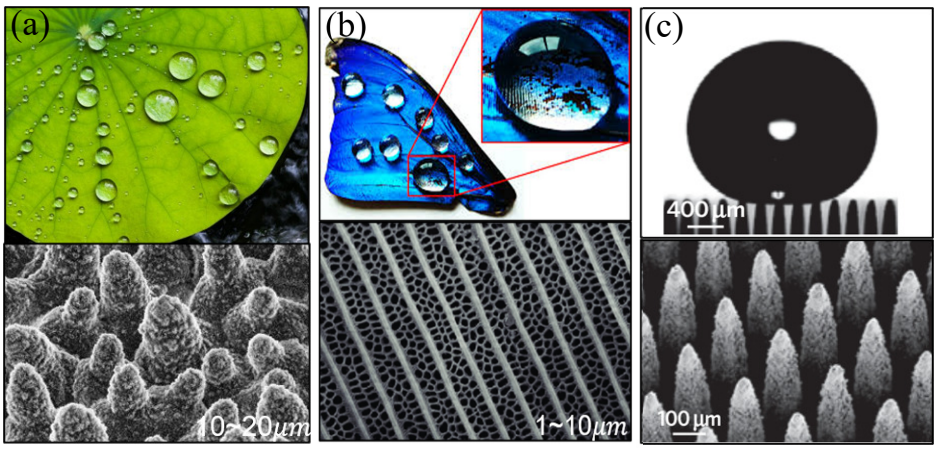

Figure 1.1: Droplets sitting on superhydrophobic surfaces: (a) lotus leaf and its micro-pillared structure [13]; (b) butterfly wing and its micro-grooved structure [14]; (c) artificial hydrophobic surface with micro pillars [11].

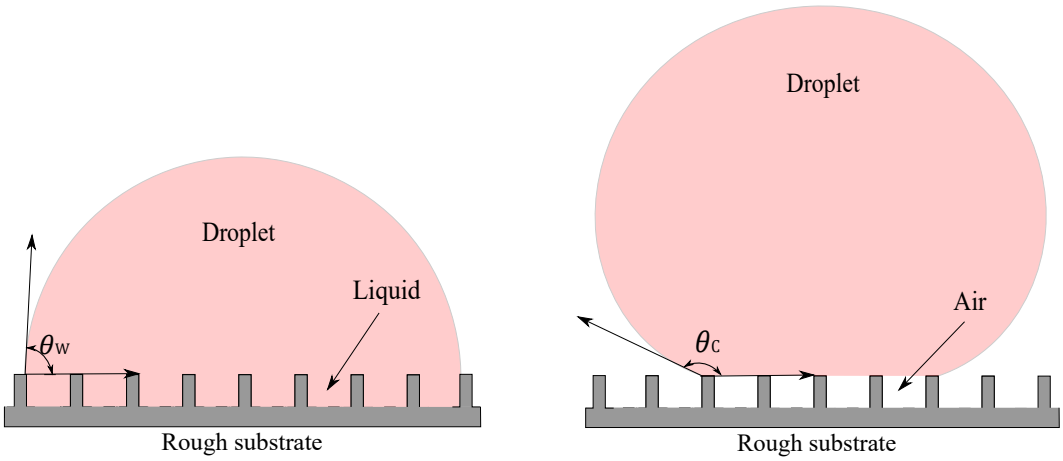

(a) Wenzel state (b) Cassie state

Figure 1.2: Wetting states of droplets on rough substrates: (a) Wenzel state; (b) Cassie state.

wing in Fig.1.1(b), higher hydrophobicity [11, 12] surfaces can also be produced through the combination of surface roughness with low energy surfaces, as shown in Fig.1.1(c).

Regarding the hydrophobicity caused by the surface roughness, two models have been proposed to describe the wetting state of a water droplet on a rough substrate, namely, the Wenzel [15] and Cassie models [16]. In general, the states that can be modelled by the

Wenzel and Cassie models are referred to as the Wenzel and Cassie states, respectively. As shown in Fig. 1.2, a Wenzel state is obtained when liquid wets the rough substrate completely, whereas the behavior of liquid contacting only the outermost tops of the micro-scale structures is called the Cassie state. The apparent contact angle (θ_{W}) of a droplet in the Wenzel state is computed by $\cos\theta_{\mathrm{W}} = r\cos\theta_{\mathrm{Y}}$, where r is the surface roughness factor defined as the ratio of the total surface area (including the sides and base) of the roughness elements to the projected surface area (not including the sides) of the roughness elements. Thus, r is always larger than 1 for rough surfaces. In addition, θ_{Y} is the Young's angle [17] or the intrinsic contact angle, when the thermodynamic equilibrium is reached on a smooth, homogeneous, and rigid horizontal solid surface, and $\cos\theta_{\mathrm{Y}} = (\sigma_{\mathrm{sa}} - \sigma_{\mathrm{sl}})/\sigma$, where σ_{sa}, σ_{sl} and σ are surface tension on the solid−air boundary, solid−liquid boundary, and liquid−air boundary, respectively.

For the Cassie state, however, the apparent contact angle (θ_{C}) is given by $\cos\theta_{\mathrm{C}} = f_{\mathrm{s}}\cos\theta_{\mathrm{Y}} + f_{\mathrm{s}} - 1$, where f_{s} is the area fraction of the solid−liquid interface in the apparent wetting region. From this equation, θ_{C} approaches 180° when f_{s} closes to zero. Therefore, by reducing f_{s}, superhydrophobic surfaces with an apparent contact angle (ACA) of larger than 150° and a roll-off angle (RA) of smaller than 10° can be manufactured [18]. These surfaces present a promising approach to realizing the easy-removal of water droplets for different industrial applications. In general, in industrial fields, droplets experience an impact, spread, and rebound. Thus, the impingement of a droplet on a textured surface has been a hot topic [9, 10, 19].

By means of experiments, impinging droplets show rapid removal on surfaces masked with pillars [11], grooves [20] and holes [21]. On a surface with micro-pillars, for instance, Liu et al. [11] found the pancake bouncing behavior (illustrating the superhydrophobicity of the surface) of an impinging droplet. This brings about a fourfold reduction in the contact time (t_{c}, the time period from when the droplet first touches the surface to when it leaves the surface [22]) compared with that of a conventional complete rebound. On surfaces with micro-scale grooves, Guo et al. [23] observed that impacting droplets bounced off the surface in a petal-like shape, and the contact time was reduced by

$\sim$70%. On these textured surfaces, however, a wetting transition from the Cassie state to the Wenzel state occurs under external factors such as large impinging velocities [24], imposed pressure [25], and vibration [26]. In the Wenzel state, the liquid in the structure space is arrested by the micro-scale structures, thereby weakening the hydrophobicity of a textured surface. To prevent this Cassie-to-Wenzel transition, efforts have been made to construct surfaces by introducing multi-scale structures [27], re-entrant topographies [28], T-shaped posts [29], and mushroom pillars [30]. Despite the employment of the above surfaces, a Cassie-to-Wenzel inevitably occurs when a droplet impinges on these surfaces with large velocities. In addition, these re-entrant and T-shaped structures are facing challenges in manufacturing owing to the complex profiles. Hence, further studies should be conducted on designing surfaces with a robust Cassie state.

Theoretical models for predicting the droplet-wall contact time (t_c) and the maximum spreading factor (β_{max}) have been proposed. Here, β_{max} is defined as the ratio of the maximum spreading diameter (D_{max}) to initial droplet diameter (D_0). For a droplet on a flat surface, t_c is yielded using a popular function proposed by Richard et al. [22] when balancing the inertia (on the order of $\rho_l D_0/2t_c^2$) with the capillarity ($4\sigma/{D_0}^2$), $t_c \approx ({\rho_l {D_0}^3}/{8\sigma})^{1/2}$, where ρ_l is the density of a liquid droplet, and D_0 is the initial droplet diameter. This equation illustrates that t_c is not dependent on the impinging velocity or properties of the surrounding air, but is expected to be a function of ρ_l, D_0, and σ. On textured surfaces, however, t_c behaves rather different, and it is greatly affected by the structure shape, the impinging velocity, and the wetting state. As for β_{max}, semiempirical correlations [31–33] and theoretical models [34–37] have been formulated on smooth and textured surfaces. It can be seen that β_{max} depends on liquid properties such as the density (ρ_l), viscosity (μ_l), and surface tension (σ), as well as solid properties including the intrinsic contact angle (θ_Y) and surface roughness. Accurately predicting the maximum spreading factor is important for understanding the deformation of an impinging droplet. However, current models make many different assumptions, which may lead to a larger error in β_{max}. For instance, although the droplet shape at the maximum spreading stage is assumed to be a cylinder [34, 37], or a central cylinder

wrapped by another semi-cylinder [20], experimental [38–40] and numerical [40, 41] evidence shows that an air cavity appears in the center of the droplet, forming a donut- or ring-like shape. In addition, the energy loss of the three-phase contact line (TPCL) depinning on micro-scale structures has yet to be considered in many existing models (A TPCL is formed when a liquid droplet in air meets a solid surface. In a 3D system, the TPCL is a 2D curve representing the intersection of the free surface with the surface of the geometry [42]).

A numerical simulation is a powerful and cost-effective tool for investigating the droplet−wall interaction. Undoubtedly, one of the most challenging tasks for such a simulation is how to correctly predict the evolution of the air−liquid interface. Selective (but not limited) studies have provided different models for interface tracking, i.e., Lagrangian (marker cell [43], deforming grid [44, 45],and front tracking [46, 47]), Eulerian (volume of fluid method (VOF) [48–51], level set method [52, 53], coupled level set and volume of fluid method (CLSVOF) [54, 55]), Eulerian−Lagrangian [56], Lattice−Boltzmann [57, 58], and lately the phase field approach (Cahn−Hillard equation) [59]. For example, Malgarinos et al. [60] performed simulations of a droplet impinging on a flat surface, and found that the evolution of the liquid−air interface was well predicated using the VOF method. Yokoi [61] conducted a study on a droplet−wall interaction using a CLSVOF method and found that free surface flows with complex interface geometries (droplet splashing) are well captured. Furthermore, numerical methods for both the air−liquid interface and the air−liquid−solid interface (the TPCL) should be employed. The sliding of the TPCL is largely affected by the wettability of the surface, thus leading to different behaviors of the water droplets. For example, a pancake bouncing behavior is obtained on superhydrophobic (contact angle of larger than 150°) surfaces [11], whereas the liquid spreads out and forms a thin film on superhydrophilic (contact angle of smaller than 5°) substrates [62]. Therefore, the contact angle should be implemented into the boundary condition. Three widely utilized methods for a contact angle implementation are (1) imposing the contact angle while calculating the interface vector and surface curvature [63], (2) considering the contact angle while projecting the

ghost value in the wall [64], and (3) implementing the contact angle directly while solving the CLSVOF functions [42]. However, methods (1) and (2) face a challenge of accurately locating the TPCL, which is typically represented by three or more cells in the computational fluid dynamics (CFD). Method (3), proposed by Sussman [42], implements the contact angle directly when computing the extension velocity in the level-set (LS) function, which is an effective approach, that brings about no extra labor for locating the specific position of the TPCL. This method was employed by Yokoi [54, 61] in studying the droplet impingement on a flat surface; however, its effectiveness in performing a droplet impinging on a textured surface remains unclear.

Based on the situation mentioned above, in this thesis, the droplet impingement on surfaces with micro-scale structures is investigated using a CLSVOF-based direct numerical simulation (DNS) method. The aim is to explore the dynamics and wetting sate of an impinging droplet on textured surfaces. First, the relationship between the groove structures and the surface hydrophobicity is quantitatively investigated. The findings provide guild lines for following works. Second, we study the effect of nonuniform structures on the dynamics of a water droplet. A nonuniform structure is obtained by gradually altering the groove width. Third, the issue of the wetting transition from the Cassie to the Wenzel state is considered because this wetting transition usually weakens the hydrophobicity of textured surfaces. Hence, we designed a novel surface with higher primary structures (to enhance the hydrophobicity) and a shorter secondary structure (to suppress the Cassie-to-Wenzel transition). To better stabilize the Cassie state even at a large impingement velocity, a surface with multiple holes is finally studied.

1.2 Thesis outline

This thesis consists of seven chapters, the outline of which is shown in Fig. 1.3.

Chapter 1, the present chapter, describes the background, motivation, and outline of this thesis.

Chapter 2 describes the numerical method, an examination of the grid independence, and a numerical validation. First, the CLSVOF method is described. We then show the strategy of how to implement the contact angle into the boundary condition. Prior to the main task, we first conduct a check of the domain size, followed by the grid independence examination, and a numerical validation by comparing the numerical results with existing experiments. Hence, such numerical method is used to model the deformation of an impinging droplet in this thesis.

Chapter 3 presents the relationship between the surface hydrophobicity and the groove structures. The effects of the groove width and the initial impacting velocity on the spreading factor and the contact time are investigated. A smaller spreading factor and a shorter contact time mean an enhanced surface hydrophobicity. Two phase diagrams summarising the droplet bouncing state and wetting state are provided.

Chapter 4 shows the droplet rebound behavior on surfaces with a roughness gradient, which can be utilized to control and manipulate the transport of liquid droplets. The effects of the Weber number, groove depth, and groove width on the rebound directions of a droplet are studied. A phase diagram, illustrating the distinct areas of the rebound direction, is then provided.

Chapter 5 presents a novel textured surface to amplify the surface hydrophobicity as much as possible and simultaneously stabilize the Cassie state. The surface is decorated by higher primary structures and shorter secondary structures. The deformation, penetration, and wetting transition of droplets on the novel surface are investigated. Inspired by the simulation results, a fractal-structured surface that can obtain a more stable Cassie state owing to the multi-level structures is proposed.

Chapter 6 shows the stability of the Cassie state on surfaces with multiple holes. The variation in the pressure in the holes is analyzed. In addition, a theoretical model

for predicting the maximum spreading factor is deduced, which considers the air cavity in the center of the droplet and the energy loss of the TPCL depinning.

Chapter 7 summaries all investigations carried out in this thesis. Recommendations for possible future extensions of the present study are also provided.

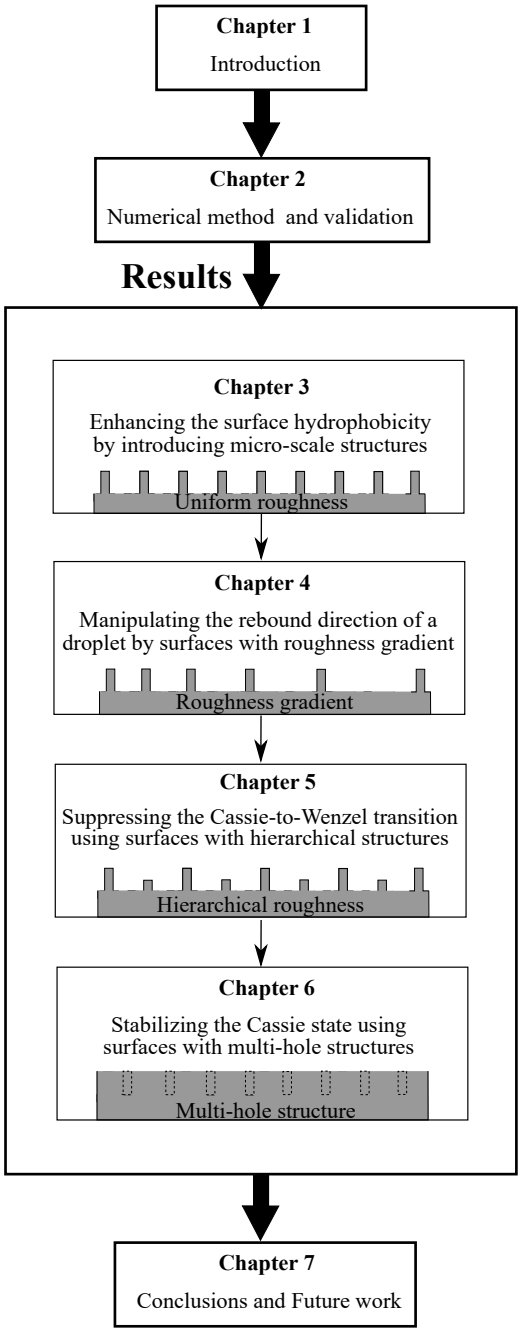

Figure 1.3: Outline of this thesis.

References

[1] Y. S. Joung and C. R. Buie. Aerosol generation by raindrop impact on soil. *Nat. Commun.*, 6(1):1–9, 2015.

[2] E. L. Schiavo, D. Laera, E. Riber, L. Gicquel, and T. Poinsot. Effects of liquid fuel/wall interaction on thermoacoustic instabilities in swirling spray flames. *Combust. Flame*, 219:86–101, 2020.

[3] J. Castrejón-Pita, G. Martin, S. Hoath, and I. Hutchings. A simple large-scale droplet generator for studies of inkjet printing. *Rev. Sci. Instrum.*, 79(7):075108, 2008.

[4] A. L. Yarin. Drop impact dynamics: splashing, spreading, receding, bouncing.... *Annu. Rev. Fluid Mech.*, 38:159–192, 2006.

[5] Y.-Y. Quan, L.-Z. Zhang, R.-H. Qi, and R.-R. Cai. Self-cleaning of surfaces: the role of surface wettability and dust types. *Sci. Rep.*, 6:38239, 2016.

[6] M. J. Kreder, J. Alvarenga, P. Kim, and J. Aizenberg. Design of anti-icing surfaces: smooth, textured or slippery? *Nat. Rev. Mater.*, 1(1):1–15, 2016.

[7] J. B. Boreyko and C.-H. Chen. Self-propelled dropwise condensate on superhydrophobic surfaces. *Phys. Rev. Lett.*, 103(18):184501, 2009.

[8] R. J. Daniello, N. E. Waterhouse, and J. P. Rothstein. Drag reduction in turbulent flows over superhydrophobic surfaces. *Phys. Fluids*, 21(8):085103, 2009.

[9] J. Jeevahan, M. Chandrasekaran, G. B. Joseph, R. Durairaj, and G. Mageshwaran. Superhydrophobic surfaces: A review on fundamentals, applications, and challenges. *J. Coat. Technol. Res.*, 15(2):231–250, 2018.

[10] L. R. Scarratt, U. Steiner, and C. Neto. A review on the mechanical and thermodynamic robustness of superhydrophobic surfaces. *Adv. Colloid Interface Sci.*, 246:133–152, 2017.

[11] Y. Liu, L. Moevius, X. Xu, T. Qian, J. M. Yeomans, and Z. Wang. Pancake bouncing on superhydrophobic surfaces. *Nat. Phys.*, 10(7):515–519, 2014.

[12] D. Khojasteh, M. Kazerooni, S. Salarian, and R. Kamali. Droplet impact on superhydrophobic surfaces: A review of recent developments. *J. Ind. Eng. Chem.*, 42:1–14, 2016.

[13] M. Costa, B. Veigas, J. Jacob, D. Santos, J. Gomes, P. Baptista, R. Martins, J. Inácio, and E. Fortunato. A low cost, safe, disposable, rapid and self-sustainable paper-based platform for diagnostic testing: lab-on-paper. *Nanotechnology*, 25(9):094006, 2014.

[14] B. A. Bober, J. K. Ogata, V. E. Martinez, J. J. Hallinan, T. A. Leach, and B. Negru. Investigating Nanoscopic Structures on a Butterfly Wing To Explore Solvation and Coloration. *J. Chem. Educ.*, 95(6):1004–1011, 2018.

[15] R. N. Wenzel. Resistance of solid surfaces to wetting by water. *Ind. Eng. Chem.*, 28(8):988–994, 1936.

[16] A. Cassie and S. Baxter. Wettability of porous surfaces. *Trans. Faraday Soc.*, 40:546–551, 1944.

[17] T. Young. III. An essay on the cohesion of fluids. *Phil. Trans. R. Soc. London*, 95:65–87, 1805.

[18] D. Wang, Q. Sun, M. J. Hokkanen, C. Zhang, F.-Y. Lin, Q. Liu, S.-P. Zhu, T. Zhou, Q. Chang, B. He, et al. Design of robust superhydrophobic surfaces. *Nature*, 582(7810):55–59, 2020.

[19] K. Ellinas, A. Tserepi, and E. Gogolides. Durable superhydrophobic and superamphiphobic polymeric surfaces and their applications: A review. *Adv. Colloid Interface Sci.*, 250:132–157, 2017.

[20] V. Vaikuntanathan and D. Sivakumar. Maximum spreading of liquid drops impacting on groove-textured surfaces: Effect of surface texture. *Langmuir*, 32(10):2399–2409, 2016.

[21] H. Mayama, T. Nishino, A. Sekiguchi, R. Nishimura, K. Uchida, S. Yokojima, S. Nakamura, and Y. Nonomura. Theoretical consideration of wetting in Cassie-Baxter state on multi-pillar and multi-hole surfaces: Thermodynamics and Laplace pressure. *J. Photopolym. Sci. Technol.*, 32(2):279–285, 2019.

[22] D. Richard, C. Clanet, and D. Quéré. Contact time of a bouncing drop. *Nature*, 417(6891):811–811, 2002.

[23] C. Guo, D. Zhao, Y. Sun, M. Wang, and Y. Liu. Droplet impact on anisotropic superhydrophobic surfaces. *Langmuir*, 34(11):3533–3540, 2018.

[24] D. Bartolo, F. Bouamrirene, E. Verneuil, A. Buguin, P. Silberzan, and S. Moulinet. Bouncing or sticky droplets: Impalement transitions on superhydrophobic micropatterned surfaces. *Europhys. Lett.*, 74(2):299, 2006.

[25] N. A. Patankar. Consolidation of hydrophobic transition criteria by using an approximate energy minimization approach. *Langmuir*, 26(11):8941–8945, 2010.

[26] E. Bormashenko, R. Pogreb, G. Whyman, Y. Bormashenko, and M. Erlich. Vibration-induced Cassie-Wenzel wetting transition on rough surfaces. *Appl. Phys. Lett.*, 90(20):201917, 2007.

[27] M. Nosonovsky. Multiscale roughness and stability of superhydrophobic biomimetic interfaces. *Langmuir*, 23(6):3157–3161, 2007.

[28] M. Nosonovsky and B. Bhushan. Why re-entrant surface topography is needed for robust oleophobicity. *Phil. Trans. R. Soc. A*, 374(2073):20160185, 2016.

[29] J. Wang, F. Liu, H. Chen, and D. Chen. Superhydrophobic behavior achieved from hydrophilic surfaces. *Appl. Phys. Lett.*, 95(8):084104, 2009.

[30] R. Hensel, R. Helbig, S. Aland, H.-G. Braun, A. Voigt, C. Neinhuis, and C. Werner. Wetting resistance at its topographical limit: The benefit of mushroom and serif T structures. *Langmuir*, 29(4):1100–1112, 2013.

[31] B. L. Scheller and D. W. Bousfield. Newtonian drop impact with a solid surface. *AIChE J.*, 41(6):1357–1367, 1995.

[32] I. S. Bayer and C. M. Megaridis. Contact angle dynamics in droplets impacting on flat surfaces with different wetting characteristics. *J. Fluid Mech.*, 558:415, 2006.

[33] I. V. Roisman. Inertia dominated drop collisions. II. An analytical solution of the Navier–Stokes equations for a spreading viscous film. *Phys. Fluids*, 21(5):052104, 2009.

[34] M. Pasandideh-Fard, Y. Qiao, S. Chandra, and J. Mostaghimi. Capillary effects during droplet impact on a solid surface. *Phys. Fluids*, 8(3):650–659, 1996.

[35] T. Mao, D. C. Kuhn, and H. Tran. Spread and rebound of liquid droplets upon impact on flat surfaces. *AIChE J.*, 43(9):2169–2179, 1997.

[36] C. Ukiwe and D. Y. Kwok. On the maximum spreading diameter of impacting droplets on well-prepared solid surfaces. *Langmuir*, 21(2):666–673, 2005.

[37] J. B. Lee and S. H. Lee. Dynamic wetting and spreading characteristics of a liquid droplet impinging on hydrophobic textured surfaces. *Langmuir*, 27(11):6565–6573, 2011.

[38] C. D. Modak, A. Kumar, A. Tripathy, and P. Sen. Drop impact printing. *Nat. Commun.*, 11(1):1–11, 2020.

[39] L. Chen, E. Bonaccurso, P. Deng, and H. Zhang. Droplet impact on soft viscoelastic surfaces. *Phys. Rev. E*, 94(6):063117, 2016.

[40] Y. Liu, M. Andrew, J. Li, J. M. Yeomans, and Z. Wang. Symmetry breaking in drop bouncing on curved surfaces. *Nat. Commun.*, 6(1):1–8, 2015.

[41] Z. Yuan, J. Wen, M. Matsumoto, and R. Kurose. Anti-wetting ability of the hydrophobic surface decorated by submillimeter grooves. *Int. J. Multiph. Flow*, 131:103404, 2020.

[42] M. Sussman. An adaptive mesh algorithm for free surface flows in general geometries. In *Adaptive method of lines*, 207–231. Chapman and Hall/CRC, 2001.

[43] F. H. Harlow and J. E. Welch. Numerical calculation of time-dependent viscous incompressible flow of fluid with free surface. *Phys. Fluids*, 8(12):2182–2189, 1965.

[44] J. Fukai, Y. Shiiba, T. Yamamoto, O. Miyatake, D. Poulikakos, C. M. Megaridis, and Z. Zhao. Wetting effects on the spreading of a liquid droplet colliding with a flat surface: experiment and modeling. *Phys. Fluids*, 7(2):236–247, 1995.

[45] Z. Zhao, D. Poulikakos, and J. Fukai. Heat transfer and fluid dynamics during the collision of a liquid droplet on a substrate—I. Modeling. *Int. J. Heat Mass Transf.*, 39(13):2771–2789, 1996.

[46] S. Manservisi and R. Scardovelli. A variational approach to the contact angle dynamics of spreading droplets. *Comput. Fluids*, 38(2):406–424, 2009.

[47] M. Muradoglu and S. Tasoglu. A front-tracking method for computational modeling of impact and spreading of viscous droplets on solid walls. *Comput. Fluids*, 39(4):615–625, 2010.

[48] Š. Šikalo, H.-D. Wilhelm, I. Roisman, S. Jakirlić, and C. Tropea. Dynamic contact angle of spreading droplets: Experiments and simulations. *Phys. Fluids*, 17(6):062103, 2005.

[49] S. F. Lunkad, V. V. Buwa, and K. Nigam. Numerical simulations of drop impact and spreading on horizontal and inclined surfaces. *Chem. Eng. Sci.*, 62(24):7214–7224, 2007.

[50] G. Strotos, G. Aleksis, M. Gavaises, K.-S. Nikas, N. Nikolopoulos, and A. Theodorakakos. Non-dimensionalisation parameters for predicting the cooling effectiveness

of droplets impinging on moderate temperature solid surfaces. *Int. J. Therm. Sci.*, 50(5):698–711, 2011.

[51] N. Nikolopoulos, A. Theodorakakos, and G. Bergeles. A numerical investigation of the evaporation process of a liquid droplet impinging onto a hot substrate. *Int. J. Heat Mass Transf.*, 50(1-2):303–319, 2007.

[52] D. Caviezel, C. Narayanan, and D. Lakehal. Adherence and bouncing of liquid droplets impacting on dry surfaces. *Microfluidic Nanofluidic*, 5(4):469–478, 2008.

[53] M. Griebel and M. Klitz. Simulation of droplet impact with dynamic contact angle boundary conditions. In *Singular Phenomena and Scaling in Mathematical Models*, 297–325. Springer, 2014.

[54] K. Yokoi, D. Vadillo, J. Hinch, and I. Hutchings. Numerical studies of the influence of the dynamic contact angle on a droplet impacting on a dry surface. *Phys. Fluids*, 21(7):072102, 2009.

[55] Z. Yuan, M. Matsumoto, and R. Kurose. Directional migration of an impinging droplet on a surface with wettability difference. *Phys. Rev. Fluids*, 5(11):113605, 2020.

[56] S. Ganesan. On the dynamic contact angle in simulation of impinging droplets with sharp interface methods. *Microfluidic Nanofluidic*, 14(3):615–625, 2013.

[57] S. Mukherjee and J. Abraham. Investigations of drop impact on dry walls with a lattice-Boltzmann model. *J. Colloid Interface Sci.*, 312(2):341–354, 2007.

[58] Y. Tanaka, Y. Washio, M. Yoshino, and T. Hirata. Numerical simulation of dynamic behavior of droplet on solid surface by the two-phase lattice Boltzmann method. *Comput. Fluids*, 40(1):68–78, 2011.

[59] S. Dong. On imposing dynamic contact-angle boundary conditions for wall-bounded liquid–gas flows. *Comput. Method. Appl. Mech. Eng.*, 247:179–200, 2012.

[60] I. Malgarinos, N. Nikolopoulos, M. Marengo, C. Antonini, and M. Gavaises. VOF simulations of the contact angle dynamics during the drop spreading: Standard models and a new wetting force model. *Adv. Colloid Interface Sci.*, 212:1–20, 2014.

[61] K. Yokoi. A practical numerical framework for free surface flows based on CLSVOF method, multi-moment methods and density-scaled CSF model: Numerical simulations of droplet splashing. *J. Comput. Phys.*, 232(1):252–271, 2013.

[62] T. Otitoju, A. Ahmad, and B. Ooi. Superhydrophilic (superwetting) surfaces: A review on fabrication and application. *J. Ind. Eng. Chem.*, 47:19–40, 2017.

[63] J. U. Brackbill, D. B. Kothe, and C. Zemach. A continuum method for modeling surface tension. *J. Comput. Phys.*, 100(2):335–354, 1992.

[64] S. Afkhami and M. Bussmann. Height functions for applying contact angles to 2D VOF simulations. *Int. J. Numer. Methods Fluids*, 57(4):453–472, 2008.

Chapter 2

Numerical method and validation

2.1 Introduction

In this chapter, the computational methodology used in this thesis is introduced. Considering the droplet size at the real scale and the accuracy of the calculation, a coupled level-set and volume of fluid (CLSVOF) method based direct numerical simulation (DNS) is employed to track the evolution of the liquid−air interface [1, 2]. When the liquid meets the substrate, the shape and the behavior of a droplet depend on the wettability (quantified by the contact angle) of the surface. For example, the pancake bouncing behavior is obtained on superhydrophobic (contact angle of larger than 150°) surfaces [3], whereas the liquid spreads out and forms a thin film on superhydrophilic (contact angle of smaller than 5°) substrates [4]. Therefore, the contact angle should be implemented into the boundary of the three-phase contact line (TPCL). We apply the method proposed by Sussman [5], which brings about no extra effort for locating the position of the TPCL. The contact angle is imposed into the boundary directly while we solve the CLSVOF function. The numerical discretization following the finite difference method (FDM) is then described. Prior to the main task, we conduct a domain size validation and a grid independence examination. The numerical validation is presented by comparing the numerical results with experiments. Thus, we confirm that the numerical method is applicable to the simulation of a droplet impinging on a textured surface.

2.2 Methodology

2.2.1 Governing equations

In this study, fluids are assumed to be incompressible. The deformation of an impinging droplet on a solid surface is examined using an in-house code FK^3 [1, 2], where a single set of governing equations are utilized within the entire computational domain. With this approach, the governing equations for mass conservation (continuity) and momentum conservation (Navier–Stokes) are written as

$$\nabla \cdot \boldsymbol{u} = 0 \tag{2.1}$$

$$\rho \left(\frac{\partial \boldsymbol{u}}{\partial t} + \boldsymbol{u} \cdot \nabla \boldsymbol{u} \right) = -\nabla P + \nabla \cdot \mu \left[\nabla \boldsymbol{u} + (\nabla \boldsymbol{u})^T \right] + \rho \boldsymbol{g} + \boldsymbol{F}_\sigma \tag{2.2}$$

where $\boldsymbol{u}$ is the velocity, t is the time step; t=2 $\times$ 10^{-6}s initially, which is dynamically controlled by the Courant number $C_{fl} = \boldsymbol{u}t/\Delta$ to enforce the stability of the calculation (C_{fl}=0.2), and Δ is the mesh size. In addition, P is the pressure, ρ and μ are the density and viscosity, respectively, whose jump values at the interface are smoothed by the Heaviside function $H_\Gamma(\varphi)$, $\boldsymbol{g}$ the gravitational acceleration ($|\boldsymbol{g}|$= 9.8 m/s^2), and the surface tension force ($\boldsymbol{F}_\sigma$) is interpreted as a body force localized on the interface based on the continuum surface force (CSF) method [6]. The density (ρ) and the viscosity (μ) in Eq. (2.2) are smoothed by the Heaviside function $H_\Gamma(\varphi)$ (see Fig. 2.1) and are defined as

$$\rho = \rho_l H_\Gamma(\varphi) + \rho_a [1 - H_\Gamma(\varphi)] \tag{2.3}$$

$$\mu = \mu_l H_\Gamma(\varphi) + \mu_a [1 - H_\Gamma(\varphi)] \tag{2.4}$$

$$H_\Gamma(\varphi) = \begin{cases} 0 & (\varphi < -\Gamma) \\ \frac{1}{2} \left[1 + \frac{\varphi}{\Gamma} + \frac{1}{\pi} \sin \left(\frac{\pi \varphi}{\Gamma} \right) \right] & (|\varphi| \leq \Gamma) \\ 1 & (\varphi > \Gamma) \end{cases} \tag{2.5}$$

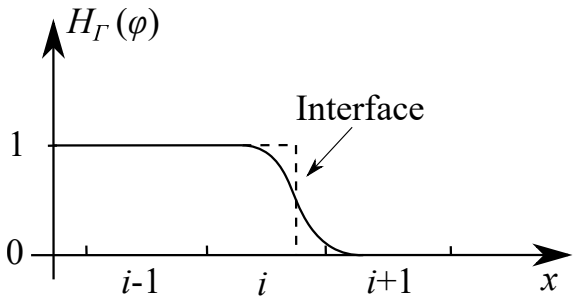

Figure 2.1: One-dimensional schematic figure of the Heaviside function (bold line) [7]. The dotted line represents the characteristic function of VOF method.

where a and l represent the air and the liquid, respectively, φ is the level-set function, Δ is the mesh size, and $\Gamma = 1.5\ \Delta$ selected in the present the study represents the half-thickness of the air−liquid interface.

2.2.2 CLSVOF interface capturing scheme

As mentioned in Chapter 1, one challenge in the numerical modelling of two-phase flows is to accurately track the evolution of the dynamic interface, particularly when the density and viscosity ratios between the two fluids are high. The volume of fluid (VOF) method has the advantage of mass conservation, whereas with the level-set (LS) method, the surface tension force can be calculated more accurately. Hence, a CLSVOF method is employed in this study. In the numerical framework, the VOF method is a conservative interpolation scheme for interface tracking. Based on the location of the interface calculated from the VOF function, the LS function is obtained by solving the equation used with the LS method for re-initialization without needing to solve its advection equation. In addition, the CLSVOF method is shown to be less computationally expensive.

2.2.2.1 VOF method

With the VOF method, the interface is localized based on the VOF function (C), which represents the volume fraction occupied by the liquid phase in each computational cell. We define $C = 0$ representing a control volume completely filled with air, whereas a

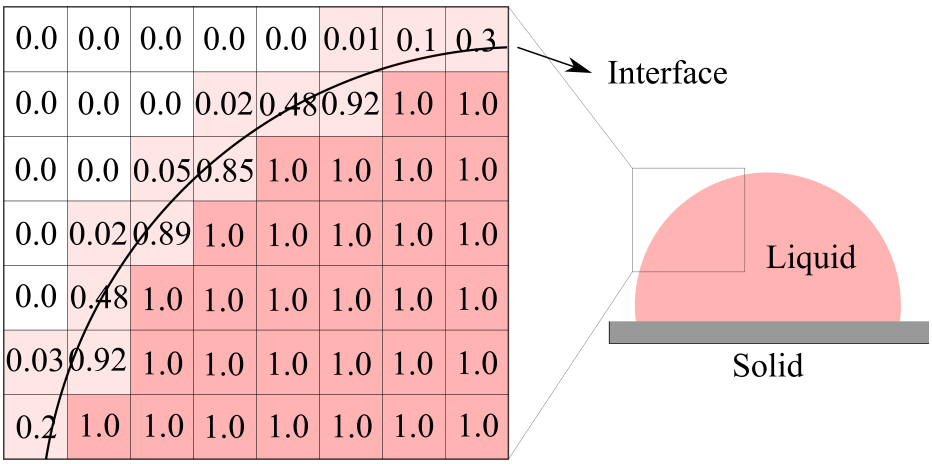

Figure 2.2: Surface representation of VOF method. The fraction number indicates the ratio of volume occupied by the liquid. The deep pink area represents the liquid phase with $C = 1$, whereas the white area represents the air phase with $C = 0$. The area colored by light pink represents the air−liquid interface with $0 < C < 1$. The black solid line represents the air-liquid interface.

value of $C = 1$ corresponds to a volume filled with liquid. Therefore the position of the air-liquid interface is described by cells with a value of $0 < C < 1$ as shown in Fig. 2.2.

The advection equation of the VOF function for three-dimensional cases is expressed as [7, 8]

$$\frac{\partial C_{i,j,k}}{\partial t} + \nabla \cdot (C_{i,j,k}\boldsymbol{u}_{i,j,k}) - C_{i,j,k}\nabla \cdot \boldsymbol{u}_{i,j,k} = 0 \tag{2.6}$$

Taking a 2-D case for example, Eq. (2.6) is discretized as follows [7],

$$C^*_{i,j} = C^n_{i,j} - \frac{F^n_{x,i+1/2,j} - F^n_{x,i-1/2,j}}{\Delta x}\Delta t + C^n_{i,j}\frac{u_{i+1/2j} - u_{i-1/2,j}}{\Delta x}\Delta t \tag{2.7}$$

$$C^{n+1}_{i,j} = C^*_{i,j} - \frac{F^*_{y,i,j+1/2} - F^*_{y,i,j-1/2}}{\Delta y}\Delta t + C^*_{i,j}\frac{v_{i,j+1/2} - v_{i,j-1/2}}{\Delta y}\Delta t \tag{2.8}$$

$$F_{x,i+1/2,j} = \begin{cases} \left(\omega_{x,i,j} \min\left(u_{i+1/2,j}\Delta t, C_{i,j}\Delta x\right) + \omega_{y,i,j} C_{i,j} u_{i+1/2,j}\Delta t\right) \frac{1}{\Delta t} \\ \qquad\qquad \text{(if } u_{i+1/2,j} \geq 0 \text{ and } \ n_{x,i,j} \geq 0) \\ \left(\omega_{x,i+1,j} \max\left(u_{i+1/2,j}\Delta t, -C_{i+1,j}\Delta x\right) + \omega_{y,i+1,j} C_{i+1,j} u_{i+1/2,j}\Delta t\right) \frac{1}{\Delta t} \\ \qquad\qquad \text{(if } u_{i+1/2,j} < 0 \text{ and } \ n_{x,i+1,j} < 0) \\ \left(\omega_{x,i,j} \max\left(0, u_{i+1/2,j}\Delta t - (1 - C_{i,j})\Delta x\right) + \omega_{y,i,j} C_{i,j} u_{i+1/2,j}\Delta t\right) \frac{1}{\Delta t} \\ \qquad\qquad \text{(if } u_{i+1/2,j} \geq 0 \text{ and } \ n_{x,i,j} < 0) \\ \left(\omega_{x,i+1,j} \min\left(0, u_{i+1/2,j}\Delta t + (1 - C_{i+1,j})\Delta x\right) + \omega_{y,i+1,j} C_{i+1,j} u_{i+1/2,j}\Delta t\right) \frac{1}{\Delta t} \\ \qquad\qquad \text{(if } u_{i+1/2,j} < 0 \text{ and } \ n_{x,i+1,j} \geq 0) \end{cases} \tag{2.9}$$

$$F_{y,i,j+1/2} = \begin{cases} \left(\omega_{y,i,j} \min\left(v_{i,j+1/2}\Delta t, C_{i,j}\Delta y\right) + \omega_{x,i,j} C_{i,j} v_{i,j+1/2}\Delta t\right) \frac{1}{\Delta t} \\ \qquad\qquad \left(\text{ if } v_{i,j+1/2} \geq 0 \text{ and } n_{y,i,j} \geq 0\right) \\ \left(\omega_{y,i,j+1} \max\left(v_{i,j+1/2}\Delta t, -C_{i,j+1/2}\Delta y\right) + \omega_{x,i,j+1/2} C_{i,j+1/2} v_{i,j+1/2}\Delta t\right) \frac{1}{\Delta t} \\ \qquad\qquad \left(\text{ if } v_{i,j+1/2} < 0 \text{ and } n_{y,i,j+1} < 0\right) \\ \left(\omega_{y,i,j} \max\left(0, v_{i,j+1/2}\Delta t - (1 - C_{i,j})\Delta y\right) + \omega_{x,i,j} C_{i,j} v_{i,j+1/2}\Delta t\right) \frac{1}{\Delta t} \\ \qquad\qquad \left(\text{ if } v_{i,j+1/2} \geq 0 \text{ and } n_{y,i,j} < 0\right) \\ \left(\omega_{y,i,j+1} \min\left(0, v_{i,j+1/2}\Delta t + (1 - C_{i,j+1})\Delta y\right) + \omega_{y,i,j+1} C_{i,j+1} v_{i,j+1/2}\Delta t\right) \frac{1}{\Delta t} \\ \qquad\qquad \left(\text{ if } v_{i,j+1/2} < 0 \text{ and } n_{y,i,j+1} \geq 0\right) \end{cases} \tag{2.10}$$

Here, $\omega_{x,i,j}$, and $\omega_{y,i,j}$ are weight functions, and are obtained from the interface normal vector as follows:

$$\omega_{x,i,j} = \frac{|n_{x,i,j}|}{|n_{x,i,j}| + |n_{y,i,j}|} \tag{2.11}$$

$$\omega_{y,i,j} = \frac{|n_{y,i,j}|}{|n_{x,i,j}| + |n_{y,i,j}|} \tag{2.12}$$

where the subscript n represents the time step, and $*$ represents the intermediate physical quantity after the advection calculation in the x- direction. In addition, $F_{x,i+1/2,j}$ and $F_{y,i,j+1/2}$ are advection fluxes in the x- and y- directions, respectively. Considering

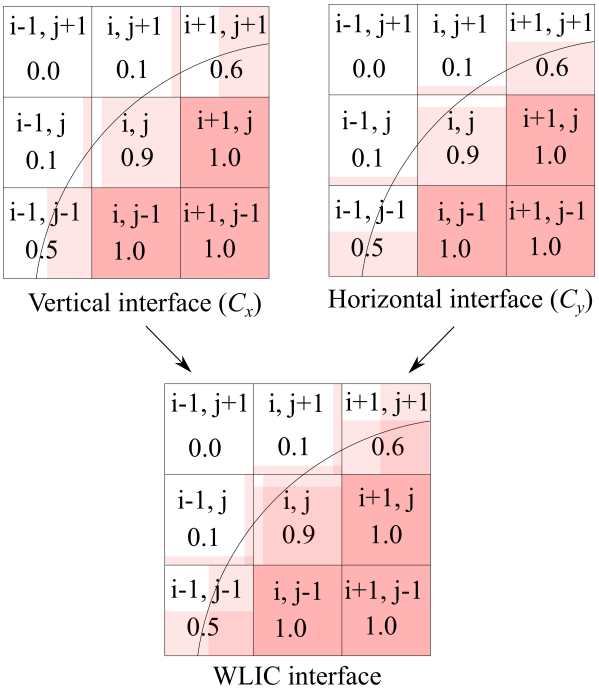

Figure 2.3: Schematic figure of WLIC algorithm [7].

the volume conservation of the fluid, the weighted linear interface calculation (WLIC) method as shown in Fig. 2.3 is utilized to weight the interface [7, 9]. Moreover, $n_{x,i,j}$ and $n_{y,i,j}$ are x- and y- components of the surface normal ($\boldsymbol{n}$), which are calculated using the values in a 3 $\times$ 3 lattice as follows:

$$n_{x,i,j} = \frac{1}{4}(n_{x,i+1/2,j+1/2} + n_{x,i-1/2,j+1/2} + n_{x,i+1/2,j-1/2} + n_{x,i-1/2,j-1/2}) \tag{2.13}$$

$$n_{y,i,j} = \frac{1}{4}(n_{y,i+1/2,j+1/2} + n_{y,i-1/2,j+1/2} + n_{y,i+1/2,j-1/2} + n_{y,i-1/2,j-1/2}) \tag{2.14}$$

where the surface normal $\boldsymbol{n}$ is estimated using a VOF function

$$n_{x,i+1/2,j+1/2} = \frac{1}{2\Delta x}(C_{i+1,j} - C_{i,j} + C_{i+1,j+1} - C_{i,j+1}) \tag{2.15}$$

$$n_{y,i+1/2,j+1/2} = \frac{1}{2\Delta y}(C_{i,j+1} - C_{i,j} + C_{i+1,j+1} - C_{i+1,j}) \tag{2.16}$$

Although the VOF method shows excellent mass conservation for the interface tracking, it lacks accuracy for the direct calculations of the normal vectors and the curvature at the interface owing to the discontinuous spatial derivatives of the VOF function. To obtain accurate interface parameters, LS method is introduced hereafter.

2.2.2.2 Level-set method

The LS method is an approach used to identify air and liquid phases by defining an LS function (φ), which indicates the signed-distance from the interface in each grid as shown in Fig. 2.4. Hence, the normal vector and the surface curvature can be accurately calculated from the continuous and smooth distance function. In addition, the surface tension term and the physical property values ρ and μ in Eqs. (2.3) and (2.4) are calculated using φ. In this calculation, the initial value of φ is constructed from the advected VOF function (C) every step [10]. For instance, the LS function ($\varphi^n_{i,j,k}$) at the nth step is calculated as follows,

$$\varphi^n_{i,j,k} = \left(C^n_{i,j,k} - C_{int}\right) \cdot \Gamma (\equiv \varphi^n_{0,i,j,k}) \tag{2.17}$$

where $\Gamma = 1.5\Delta$ represents the half-thickness of the air−liquid interface, $C^n_{i,j,k}$ is the VOF value at the nth step, and C_{int} is the VOF value at the interface, for which 0.5 is

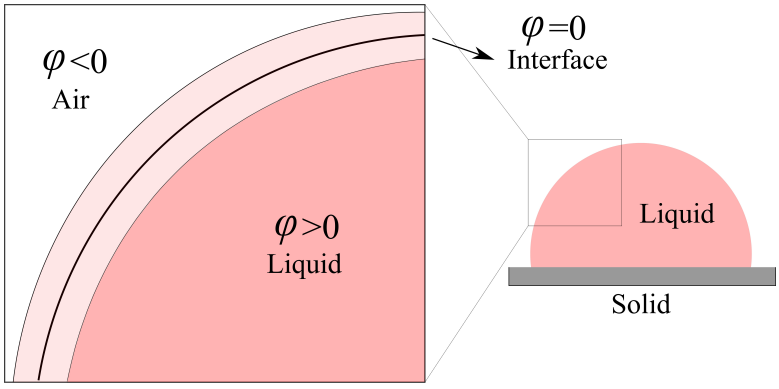

Figure 2.4: Surface representation in LS method. The deep pink area represents the liquid phase with $\varphi > 0$, whereas the white area represents the air phase with $\varphi < 0$. The area colored by light pink represents the air−liquid interface.

chosen.

In general, the direct transport of the LS function in Eq. (2.17) will destroy the signed-distance property. In addition, a transported LS function should not be utilized for an estimation of the normal vector and the surface curvature. Hence, a reinitialization process must be employed to obtain a valid signed-distance function.

The LS value ($\varphi^n_{i,j,k}$) in Eq. (2.17) is first re-distanced by solving the reinitialization equation:

$$\frac{\partial \varphi^n_{i,j,k}}{\partial \tau} + S\left(\varphi^n_{0,i,j,k}\right) \frac{\nabla \varphi^n_{0,i,j,k}}{\left|\nabla \varphi^n_{i,j,k}\right|} \cdot \nabla \varphi^n_{i,j,k} = S\left(\varphi^n_{0,i,j,k}\right) \tag{2.18}$$

$$\varphi^n_{i,j,k}\big|_{\tau=0} = \varphi^n_{0,i,j,k} \tag{2.19}$$

$$S\left(\varphi^n_{0,i,j,k}\right) = \frac{\varphi^n_{0,i,j,k}}{\sqrt{{\varphi^n_{0,i,j,k}}^2 + \Gamma^2}} \tag{2.20}$$

where τ is the artificial time step, $S\left(\varphi^n_{0,i,j,k}\right)$ is a sign function, and n denotes the time step. A secondary accuracy essentially non-oscillatory (ENO) scheme [11] is used for the discretization of Eq. (2.18).

Compared to the VOF method, the LS method brings about a smoother interface, and thus the calculation accuracy of the curvature and the normal vector at the interface is higher. Considering the merits and drawbacks of VOF and LS, we therefore select the CLSVOF method to accurately capture the liquid−air interface with a good mass conservation.

2.2.3 Surface tension

After the reinitialization process, the surface tension is calculated using Eq. (2.21) based on the continuum surface force (CSF) method [6].

$$\boldsymbol{F}_\sigma = \sigma \kappa \boldsymbol{n}_\varphi \delta_\Gamma(\varphi) \tag{2.21}$$

Here, κ is the curvature of the interface, $\boldsymbol{n}_\varphi$ is the normal vector, and $\delta_\Gamma(\varphi)$ is the smoothed Delta function (see Fig. 2.5) used to limit the effect of the surface tension to

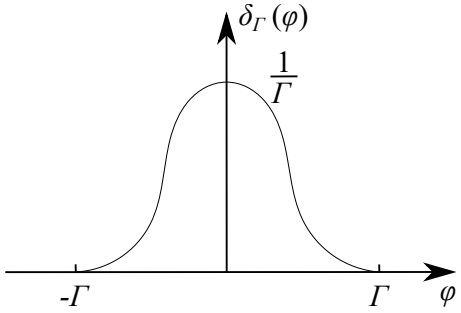

Figure 2.5: Schematic of the smoothed Delta function [7].

a narrow region around the interface [7], which can be estimated by

$$\delta_\Gamma(\varphi) = \begin{cases} 0 & (|\varphi| \geq \Gamma) \\ \frac{1}{2\Gamma}\left[1+\cos(\frac{\pi\varphi}{\Gamma})\right]\left[1+\frac{\varphi}{\Gamma}+\frac{1}{\pi}\sin\left(\frac{\pi\varphi}{\Gamma}\right)\right] & (|\varphi| < \Gamma) \end{cases} \tag{2.22}$$

$$\boldsymbol{n}_\varphi = \frac{\nabla\varphi}{|\nabla\varphi|} \tag{2.23}$$

$$\kappa = \nabla\cdot\boldsymbol{n}_\varphi = \frac{1}{|\nabla\varphi|}\left(\frac{\nabla\varphi}{|\nabla\varphi|}\cdot\nabla|\nabla\varphi| - \nabla\cdot\nabla\varphi\right) \tag{2.24}$$

For the present calculation, the surface tension is only considered on the interface where the smoothed Delta function $\delta_\Gamma(\varphi)$ in Eq. (2.22) is used, for which a modified standard CSF model is applied to improve the stability [7].

2.2.4 Contact angle implementation

In the simulations, the contact angle should be implemented near a solid surface, where a liquid meets a solid and air. A notable method proposed by Brackbill [6] effectively imposes the contact angle into the boundary condition while calculating the interface vector ($\boldsymbol{n}_\varphi$), $\boldsymbol{n}_\varphi = \boldsymbol{n}_\perp\cos\theta_\mathrm{Y} + \boldsymbol{n}_\parallel\sin\theta_\mathrm{Y}$, where $\boldsymbol{n}_\perp$ denotes the normal vector of the wall surface, and $\boldsymbol{n}_\parallel$ is the parallel vector to the wall surface. In another study [12], the contact angle is implemented in the height function (HF) of $h_{j-1} = h_j + \Delta/\tan\theta_\mathrm{Y}$ while projecting the ghost value of the height (h_{j-1}) in the wall, where Δ is the mesh size, and h is the height value. With these methods [6, 12], all cells with the TPCL

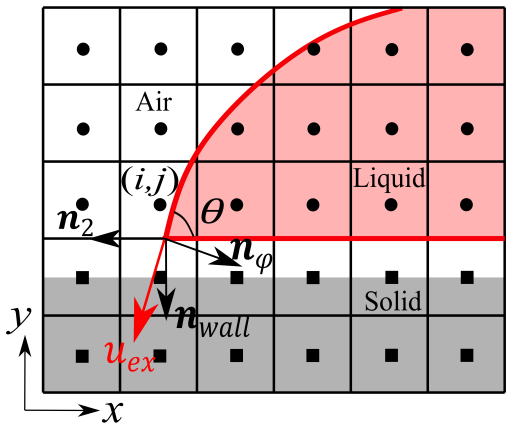

Figure 2.6: Contact angle implementation (a 2-D case) based on the method proposed by Sussman [5], and staggered grid near the wall. TPCL is in the cell (i, j) with a contact angle θ. Black circles and squares represent the solid and fluid phases, respectively. Red solid arrow $\boldsymbol{u}_{ex}$ denotes the extension velocity in the wall.

should be accurately identified to compute $\boldsymbol{n}_\varphi$ and κ, which is not an easy task because the interface of liquid is typically represented by three or more cells (such as Γ in this thesis). Given this background, an alternative approach developed by Sussman [5] is utilized here, which requires no extra effort in locating the specific position of TPCL. The contact angle is considered while computing the extension velocity (see the 2-D case in Fig. 2.6) in the VOF and the LS function [13, 14],

$$\frac{\partial \varphi^n_{i,j,k}}{\partial \tau} + \boldsymbol{u}_{ex} \cdot \nabla \varphi^n_{i,j,k} = 0 \tag{2.25}$$

where τ is the artificial time, and $\boldsymbol{u}_{ex}$ is the extension velocity depending on the contact angle between the liquid and the wall. Specifically, for a surface with a contact angle of 90°, $\boldsymbol{u}_{ex}$=$\boldsymbol{n}_{\text{wall}}$ (ignoring the dimensions) is satisfied. For surfaces with other contact angles, $\boldsymbol{u}_{ex}$ is estimated by,

$$\boldsymbol{u}_{ex} = \begin{cases} \frac{\boldsymbol{n}_{\text{wall}} - \cot(\pi - \theta_{\text{num}})\boldsymbol{n}_2}{|\boldsymbol{n}_{\text{wall}} - \cot(\pi - \theta_{\text{num}})\boldsymbol{n}_2|} & (\text{ if } \Omega < 0) \\ \boldsymbol{n}_{\text{wall}} & (\text{ if } \Omega = 0) \\ \frac{\boldsymbol{n}_{\text{wall}} + \cot(\pi - \theta_{\text{num}})\boldsymbol{n}_2}{|\boldsymbol{n}_{\text{wall}} + \cot(\pi - \theta_{\text{num}})\boldsymbol{n}_2|} & (\text{ if } \Omega > 0) \end{cases} \tag{2.26}$$

$$\boldsymbol{n}_{\text{wall}} = (0, -1, 0) \tag{2.27}$$

$$\boldsymbol{n}_1 = -\frac{\boldsymbol{n}_\varphi \times \boldsymbol{n}_{\text{wall}}}{|\boldsymbol{n}_\varphi \times \boldsymbol{n}_{\text{wall}}|} \tag{2.28}$$

$$\boldsymbol{n}_2 = -\frac{\boldsymbol{n}_1 \times \boldsymbol{n}_{\text{wall}}}{|\boldsymbol{n}_1 \times \boldsymbol{n}_{\text{wall}}|} \tag{2.29}$$

$$\Omega = \boldsymbol{n}_\varphi \cdot \boldsymbol{n}_2 \tag{2.30}$$

In 3-D cases, the TPCL is a 2-D curve, which represents the intersection of the free liquid surface with the geometry surface. The vector $\boldsymbol{n}_2$ is orthogonal to the TPCL and lies within the tangent plane of the geometry surface.

In Eq. (2.26), a numeric contact angle (θ_{num}) is introduced, which varies and depends on the combined effect of the solid material (characterized as the intrinsic contact angle, θ_{Y}), contact line velocity (u_{cl}), and surface roughness. Cox [15] divided the contact region near the TPCL into three distinct regions, as shown in Fig. 2.7: (1) the inner

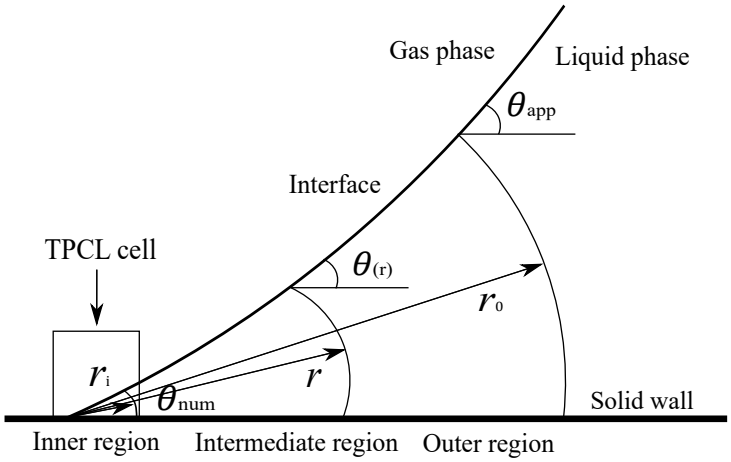

Figure 2.7: Three regions near the TPCL and the corresponding contact angles [15]: inner region with interface slope θ_{num}; intermediate region with interface slope $\theta_{(\text{r})}$; and outer region with interface slope θ_{app}.

region close to the molecular size with characteristic length r_{i} and interface slope θ_{num}, (2) the intermediate region with characteristic length r, where the interface slope $\theta_{(\mathrm{r})}$ changes sharply under the influences of viscous and surface tension forces, and (3) the outer macroscopic region with characteristic length r_{o}, where the so-called apparent contact angle (θ_{app}) is measured at distances of above $\sim$100μm during the experiments. Hence, the mesh size should be smaller than 100μm in the simulation to capture the evolution of TPCL [16]. The value of θ_{app} is often formulated as a function of θ_{Y} and Capillary number $Ca{=}\mu u_{cl}/\sigma$, where u_{cl} is the velocity of the TPCL, which is calculated based on the actual velocity at each computational cell. Equation (2.31), which is further developed by Kistler [17] based on the Hoffman's empirical correlation f_{H} [18], is utilized in this study.

$$\theta_{\mathrm{app}} = f_{\mathrm{H}}[Ca + f_{\mathrm{H}}^{-1}(\theta_{\mathrm{Y}})] \tag{2.31}$$

$$f_H(x) = \arccos\left\{1 - 2\tanh\left[5.16\left(\frac{x}{1+1.31x^{0.99}}\right)^{0.706}\right]\right\} \tag{2.32}$$

Although some studies [19, 20] have obtained good results by inserting θ_{app} into the boundary condition, the interface slope in the inner regions is not resolved. Considering the mesh size and computational cost, the numeric contact angle (θ_{num}) developed by Voinov [21] is employed

$$\theta_{\mathrm{num}}^3 = \begin{cases} \theta_{\mathrm{app}}^3 - 9Ca\ln(\frac{K}{\Delta/2}), & \text{if } 0 \le \theta_{\mathrm{app}} \le \frac{3\pi}{4}. \\ \pi - \theta_{\mathrm{app}}^3 + 2.25\pi\ln(\frac{1-\cos(\theta_{\mathrm{app}})}{1+\cos(\theta_{\mathrm{app}})}) - 9Ca\ln(\frac{K}{\Delta/2}), & \text{if } \frac{3\pi}{4} < \theta_{\mathrm{app}} \le \pi. \end{cases} \tag{2.33}$$

where K represents the macroscopic length scale, for which Voinov [21] adopted the capillary length $K = \sqrt{\sigma/\rho g}$; $\Delta/2$ is the slip length due to the staggered grid as shown in Fig. 2.6, and the surface tension force is applied a half cell width away from the substrate. Thus, the singularity problem is numerically avoided in this study.

2.2.5 Numerical procedure

The governing equations are discretized using the FDM adopting a staggered Cartesian grid. The code solver [2, 13, 14] employs a pressure-based semi-implicit (fractional-step) algorithm for incompressible flows. The nonlinear term in the momentum equation in Eq. (2.2) is approximated using a fourth-order central difference scheme, and a weighted essentially non-oscillatory (WENO) scheme [22] is applied to the convection terms of the scalar quantities. The scalar C in Eq. (2.6) is evolved using an approximation through a dimensional splitting algorithm [8], whereas a third-order accurate total variation diminishing (TVD) Runge–Kutta scheme is employed for the time integration of the convection terms in Eq. (2.2). In addition, no additional momentum source term is considered in this modelling framework.

2.3 Numerical validation

2.3.1 Domain size and grid independence study

In a numerical study on the droplet−wall interaction, effective simulation models play a vital role. Furthermore, several parameters (the mesh size, computation domain size, initial velocity, and interface thickness) should be tested and validated. In our study, over 100 test cases were applied to find the best combination, leading to stable and economic calculations. In this section, we first discuss cases with different computational domain sizes to find the optimal computational domain. Subsequently, the results with three different mesh schemes are compared to check the mesh independence. The validated computational domain and the mesh scheme are used in subsequent studies.

2.3.1.1 Domain size validation

For the size of the computational domain in droplet-wall interaction simulations, the commonly utilized schemes in existing studies (some of which are listed in Table 2.1) apply values of $(2D_0)^3$ to $(5D_0)^3$, where D_0 is the droplet diameter. If the computational domain is excessively small, the boundary conditions will bring about artifacts in the results, leading to a divergence in the pressure. An overly large domain unnecessarily increases the computational cost. Hence, to limit the artifacts to within an acceptable

Table 2.1: Computational domains in existing studies.

Author	Target	Velocity	Domain size
U. Olgac et al. [23]	Flat surface	0m/s	$1.25D_0 \times 1.875D_0$
C. Shao, et al. [24]	Flat surface	0.746m/s	$(2D_0)^3$
M. Moradi, et al. [25]	Vibrating surface	4.36m/s	$2D_0 \times 3D_0$
A.Fath, et al. [16]	Flat surface	$1.04 - 4.1$m/s	$2D_0 \times 4D_0$
S. Shin, et al. [26]	A cylinder	0.75m/s	$3D_0 \times 3D_0 \times 6D_0$
W. Li, et al. [27]	Gradient surface	2.21m/s	$(5D_0)^3$

level, the size of the domain is optimized prior to our study.

A mesh with $\Delta = 32$ μm is selected in the domain size validation. As shown in Table 2.2, five cases with a domain size ranging roughly from $(2D_0)^3$ to $(6D_0)^3$ are applied and compared to obtain a suitable size. The droplet is represented by $(63\Delta)^3$, and heads toward a the flat surface with an initial velocity of u_0=0.6m/s. The gravitational force is considered as $\boldsymbol{g} = -9.8\text{m/s}^2$. Other physical properties are listed in Table 2.3, in which an unrealistically high air density is utilized in our simulation (density ratio ρ_l/ρ_a is greater than 30) to enhance the numerical stability. Note that the effects of the viscosity and density ratios decrease rapidly and become insignificant when $\rho_l/\rho_a \geq 10$ [23, 28]. In addition, according to the existing equations [29], the droplet spreading diameter is

Table 2.2: Cases set for a validation of the domain size.

Domain size	Mesh (cells)	Cores	Time (h) /1000 steps
$(2D_0)^3$	$120 \times 120 \times 120$	$4 \times 4 \times 4$	3.0
$(3D_0)^3$	$200 \times 180 \times 200$	$5 \times 6 \times 5$	5.0
$(4D_0)^3$	$250 \times 250 \times 250$	$5 \times 10 \times 5$	5.5
$(5D_0)^3$	$320 \times 300 \times 320$	$8 \times 6 \times 8$	5.5
$(6D_0)^3$	$360 \times 360 \times 360$	$10 \times 6 \times 10$	8.0

Table 2.3: Physical properties for droplet, surrounding air, and substrate.

Parameter	Symbol	Value
Initial droplet diameter	D_0	63Δ
Intrinsic contact angle	θ_{Y} (°)	100
Surface tension coefficient	σ (N/m)	0.0728
Water density	ρ_l (kg/m^3)	1000
Water viscosity	μ_l (mPa·s)	1.0
Air density	ρ_a (kg/m^3)	30
Air viscosity	μ_a (mPa·s)	0.0183

the relation of the Reynolds number Re, Weber number We, and contact angle, and the liquid−wall contact time [30] is expected to be a function of D_0, ρ_l, and σ. Therefore, the density ratio $\rho_l/\rho_a > 30$ used herein is acceptable for studying the droplet deformation on a substrate.

A comparison of the droplet shape evolution is shown in Fig. 2.8 with the domain size equal to $(4D_0)^3$, $(5D_0)^3$, and $(6D_0)^3$. Evidently, no significant difference can be

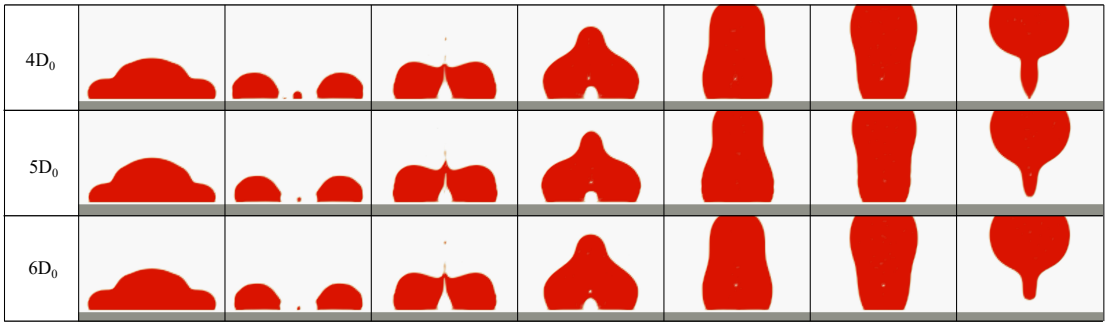

Figure 2.8: Comparison of the droplet shape evolution with the domain size at $(4D_0)^3$, $(5D_0)^3$, and $(6D_0)^3$ (cross-sectional view at the same time step).

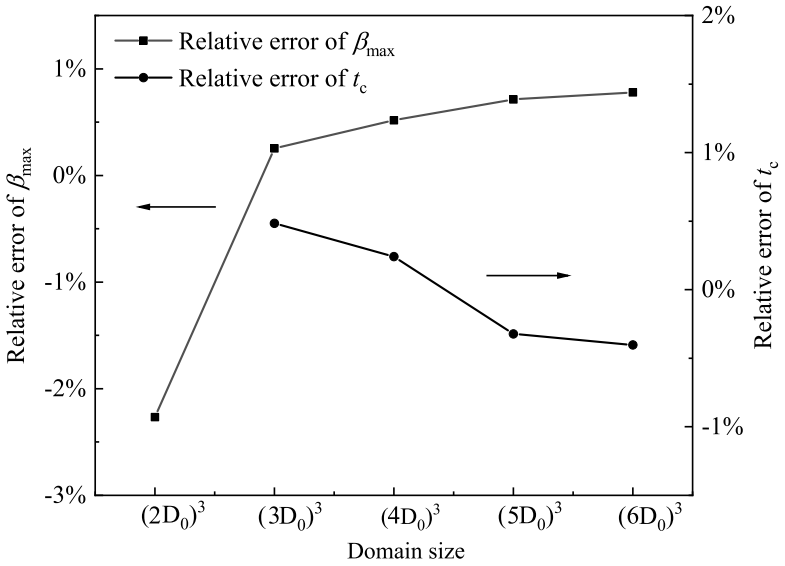

Figure 2.9: Effect of domain size on the maximum spreading factor ($\beta_{\max}$) and the contact time (t_c) of a droplet impinging on a flat surface.

found during the spreading stage, the retracting stage, or the rebounding stage.

In addition, we compare the relative errors of the maximum spreading diameter ($\beta_{\max}$) and the contact time (t_c) with respect to the values for domain size at $(5D_0)^3$, as shown in Fig. 2.9. Here, the error of $\beta_{\max}$ slightly increases with an increase in the domain size, but shows no significant difference when the domain size is larger than $(3D_0)^3$. For t_c, although its relative error slowly decreases with an increase in the domain size, the difference is quite small. The relative error of t_c with the domain size at $(2D_0)^3$ is not obtained because the calculation diverges during the retracting stage, which is caused by the small domain size and the high-speed jet injection [31]. Based on the above results, the computational domain size of $(5D_0)^3$ is selected in the following study for accurate calculations and better computational cost.

2.3.1.2 Grid independence examination

To check the mesh convergence, three cases with different grid sizes of $\Delta = 50\mu$m, 32μm, and 25μm in Table 2.4, are employed to examine the grid independence by comparing the maximum spreading factor (β_m) and the relative error with respect to the experiment

Table 2.4: Cases for grid independence examination.

Mesh	Grid size (μm)	Domain size	Time (h) /1000 steps
Coarse	50	$5D_0$	3.6
Moderate	32	$5D_0$	5.5
Dense	25	$5D_0$	11.5

Table 2.5: Maximum spreading factor ($\beta_{\max}$) and relative error with respect to the experiment [32] for three different grid sizes.

Grid size	Δ=50μm	Δ=32μm	Δ=25μm
$\beta_{\max}$	1.610	1.628	1.632
Relative error	3.07%	1.95%	1.72%

[32]. In all simulations, a droplet with diameter D_0 = 2.1mm and initial velocity u_0= 0.5m/s impacts the neutrally wet surface at θ_Y= 90°. Based on the grid independence test in Table 2.5, the grid size is set to Δ=32μm for the simulations conducted hereafter.

2.3.2 Comparison with experiment

2.3.2.1 Contact angle model validation

To further validate the numerical models, we apply other three other cases of a water droplet impacting a flat surface with a different wettability namely θ_Y = 50°, 90°, and 180°, and then compare the results with those of the previous experiment [32]. Except for the density ratio, other impact conditions such as the droplet diameter and the impact velocity are same as those in the experiment. The comparison in Fig. 2.10 illustrates a good agreement in terms of the droplet shape evolution between the simulations and experiments. Here, We is given by We= $\rho_l u_0^2 D_0/\sigma$.

Figure 2.11 compares the spreading factor (β) and apparent contact angle (θ_{app}).

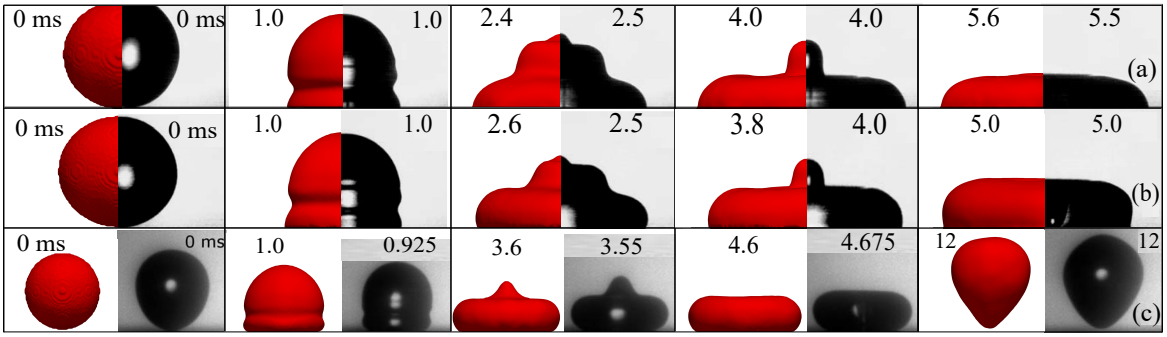

Figure 2.10: Droplet shape comparison between the simulation results (in red) and the experimental results [32] (in black): (a) droplet impinging on a strongly wetting surface with θ_Y = 50°; (b) droplet impinging on a neutrally wetting surface with θ_Y =90°; (c) droplet impinging on a completely nonwetting surface with θ_Y = 180°. The initial droplet diameter D_0 = 2.28mm and impact velocity u_0 = 0.35 m/s, corresponding to We = 3.84.

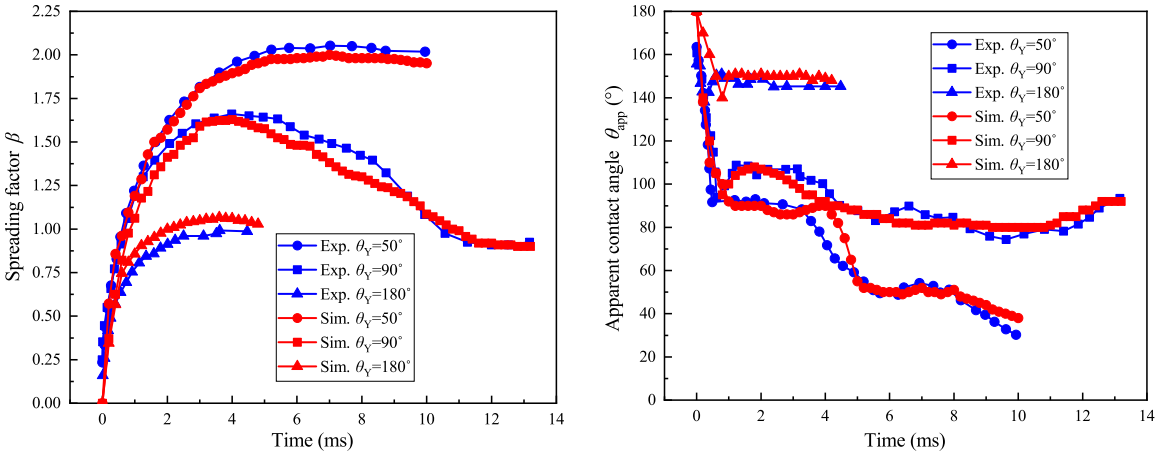

(a) Variation of spreading factor (b) Variation of apparent contact angle

Figure 2.11: Variation of spreading factor (β) and apparent contact angle (θ_{app}) for a droplet impinging on different surfaces: (a) evolution of β against time; (b) evolution of θ_{app} against time. Red lines represent the simulation results, and blue lines are the experimental results [32]. The droplet diameter $D_0 = 2.1$ mm and impact velocity $u_0 = 0.5$ m/s, corresponding to We=7.21.

These comparisons show that, despite the simulations capture the primary features of a droplet deformation on a solid surface well. Therefore, the present numerical method can be used to investigate the dynamics of an impacting droplet on a substrate with a difference in the wettability .

2.3.2.2 Droplet impinging on textured surfaces

Because our objective is focusing on the interaction between droplets and textured surfaces, prior to the simulations, cases with different impinging velocities are tested by comparing the numerical results with the experiments [29]. The experiment [29] studied the droplet impact on a micro-groove-textured substrate. Here, experimental results from a substrate of TS220 and distilled water (see Fig. 2.12) are chosen to validate the simulation because the ridge and groove section are extremely close to a rectangular shape. The cell sizes Δ utilized is 32 μm, and the droplet diameter D_0 is approximately 2.6mm.

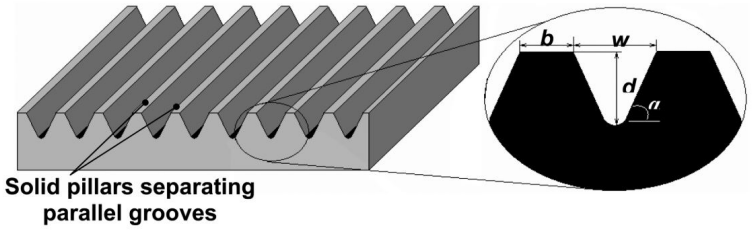

				Surface texture geometry						Surface wetting		
Sl. No.	**Target surface**	**Experimental liquid**	***We* range**	***w*** **(μm)**	***b*** **(μm)**	***d*** **(μm)**	***α*** **(deg.)**	***ϕ***	***r***	θ_Y **(deg.)**	θ_e **(deg.)**	θ_a **(deg.)**
1	*TS11*	Distilled water (W)	4 to 74	180	116	54	42	0.39	1.14	76	124	131
2	*TS140*	Distilled water (W)	1 to 74	173	126	140	80	0.42	1.79	76	137	147
3	*TS220*	Distilled water (W)	4 to 73	173	126	220	89	0.42	2.45	76	135	161
4	*TS12*	Distilled water (W)	4 to 84	177	22	53	43	0.11	1.21	76	121	134
5	*TP300*	Distilled water (W)	3 to 55	125	300	300	90	0.71	2.41	105	125	135
6	*TS220*	Ethanol-water (E05)	8 to 83	173	126	220	89	0.42	2.45	71	136	160
7	*TP300*	Ethanol-water (E05)	8 to 84	125	300	300	90	0.71	2.41	100	125	135

Figure 2.12: Textured surfaces used in the experiment [29], from which a substrate of TS220 and distilled water are chosen to validate our simulations.

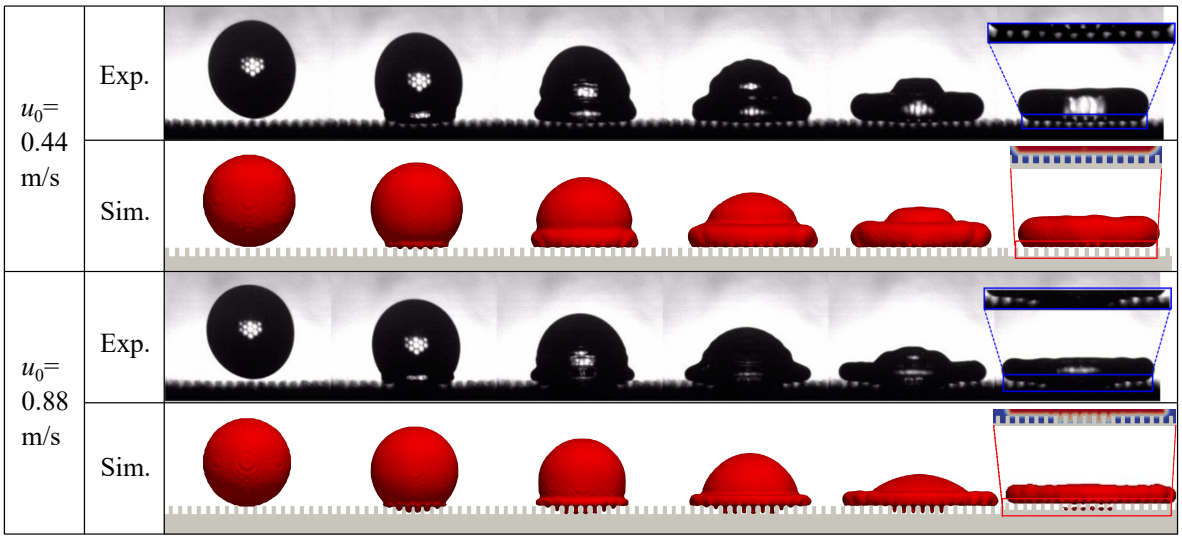

Figure 2.13: Comparison of the droplet shape between experimental results [29] (in black) and simulation results (in red).

A comparison of the droplet shape between the experiment [29] and simulation results is shown in Fig. 2.13. The first and third rows (Exp.) are from the experiment [29], whereas the second and fourth rows (Sim.) are predications of our simulation. Although small differences are seen, such as a surface wave caused by the coarse mesh, the numerical model utilized captures the main features of a droplet deformation well on a groove decorated surface. In addition, a Cassie state with $u_0 = 0.44$ m/s and a Transition state (partially impaled state [33, 34]) with $u_0 = 0.88$ m/s observed in the experiment are successfully projected by our simulations.

To further support this claim, comparisons of the maximum spreading factor in the parallel ($\beta_{\max,\parallel}$) and perpendicular ($\beta_{\max,\perp}$) groove directions are plotted against We in Fig. 2.14. In the parallel groove direction, the liquid spreads freely, whereas the liquid

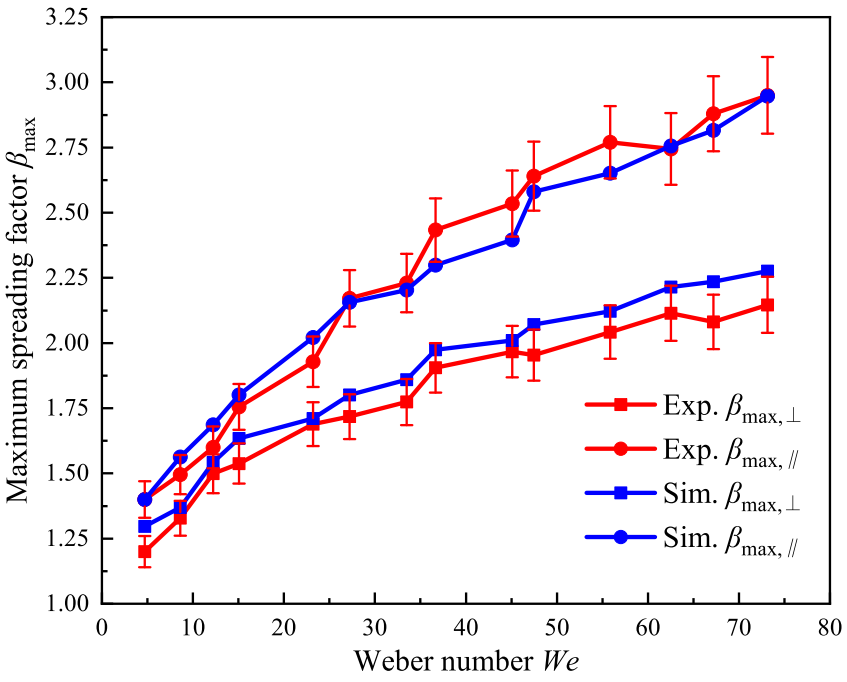

Figure 2.14: Comparison of the maximum spreading factor ($\beta_{\max}$) between experimental results [29] (in red) and simulation results (in blue). In addition, $\beta_{\max,\parallel}$ and $\beta_{\max,\perp}$ are the maximum spreading factor in the parallel and perpendicular groove directions, respectively.

meets grooves or ridges in the perpendicular groove direction. Red lines (Exp.) show the experimental data, and blue lines (Sim.) show the simulation results. It is clear that the numerical projections match well with the experiments for an error of within 5%. The error may be caused by the small difference in the groove structures between our simulations and the experiments.

2.3.3 Accuracy of the simulation

Although the DNS has been proven to be effective in studies on droplet−wall interactions, it still cannot resolve all scales involved in this problem. Here, the limitations of the present simulation are discussed to judge the simulation accuracy and the outcomes. The greatest discrepancy between the simulations and experiments is the rupture of the liquid film on a solid surface as shown at 4.8ms in Fig. 2.15, which is likely caused by the grid size, and the VOF method associated with WLIC interface reconstruction scheme. Indeed, this problem can be prevented by refining the grid such as in a thickness-based adaptive mesh refinement scheme [35], by which the thin film near the wall was efficiently resolved with a minimum grid size of approximately 0.02 μm. Many studies [16, 36] using DNS have shown good agreement with experimental results although the rupture of a thin film has not been considered. Thus, the simulation in the present study is acceptable. In addition, the numerical capability of the mass conservation is evaluated based

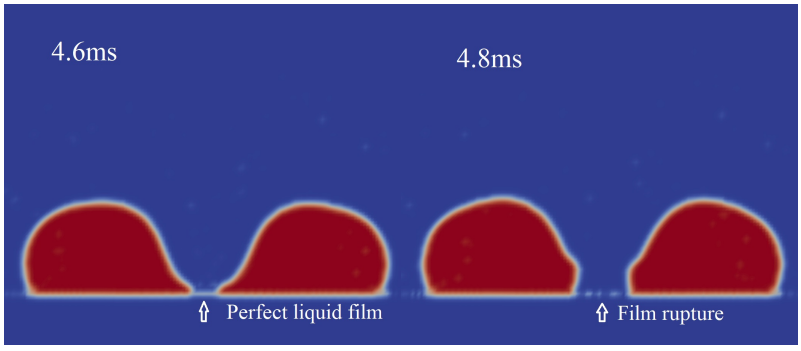

Figure 2.15: Thin liquid film rupture near a solid. The solid is suppressed to make the film visible.

on the relative mass error, $E_m = \frac{m_t - m_0}{m_0}$, where m_t is the total mass at time t , and m_0 is the initial mass. For the computations, the maximum mass error (E_m) is always smaller than 2.5 $\times 10^{-6}$. The negligibly small error proves the accurate mass conservation ability of the present simulation. Therefore, in this thesis, the simulation method is extended to predict the wetting states and deformation of droplets on substrates with micro-scale structures.

2.4 Conclusions

In this chapter, a CLSVOF-based DNS was introduced to study the dynamics of a droplet. A mesh-dependent contact angle model was implemented into the boundary condition to evaluate the effect of the surface wettability. In addition, the computational domain size was checked, and the independence of the mesh size was confirmed. The model was validated by comparing the present simulation results with experimental results. The main results obtained in this chapter are summarized as follows.

1. Mesh size $\Delta = 32$ μm and a computational domain size of $(5D_0)^3$ are adequate in the following study based on a trade-off between the accuracy and computational cost.

2. Using the CLSVOF method, a contact angle model, and an implementation scheme of the contact angle, numerical results show good agreements with the experiments. This suggests that the current numerical method is applicable to the following main tasks.

References

[1] R. Kurose. `http://www.tse.me.kyoto-u.ac.jp/members/kurose/link_e.php`.

[2] J. Wen, Y. Hu, A. Nakanishi, and R. Kurose. Atomization and evaporation process of liquid fuel jets in crossflows: A numerical study using Eulerian/Lagrangian method. *Int. J. Multiph. Flow*, 129:103331, 2020.

[3] Y. Liu, L. Moevius, X. Xu, T. Qian, J. M. Yeomans, and Z. Wang. Pancake bouncing on superhydrophobic surfaces. *Nat. Phys.*, 10(7):515–519, 2014.

[4] T. Otitoju, A. Ahmad, and B. Ooi. Superhydrophilic (superwetting) surfaces: A review on fabrication and application. *J. Ind. Eng. Chem.*, 47:19–40, 2017.

[5] M. Sussman. An adaptive mesh algorithm for free surface flows in general geometries. In *Adaptive method of lines*, 207–231. Chapman and Hall/CRC, 2001.

[6] J. U. Brackbill, D. B. Kothe, and C. Zemach. A continuum method for modeling surface tension. *J. Comput. Phys.*, 100(2):335–354, 1992.

[7] K. Yokoi. A practical numerical framework for free surface flows based on CLSVOF method, multi-moment methods and density-scaled CSF model: Numerical simulations of droplet splashing. *J. Comput. Phys.*, 232(1):252–271, 2013.

[8] K. Yokoi. A numerical method for free-surface flows and its application to droplet impact on a thin liquid layer. *J. Sci. Comput.*, 35(2-3):372–396, 2008.

[9] C. W. Hirt and B. D. Nichols. Volume of fluid (VOF) method for the dynamics of free boundaries. *J. Comput. Phys.*, 39(1):201–225, 1981.

[10] A. Albadawi, D. Donoghue, A. Robinson, D. Murray, and Y. Delauré. Influence of surface tension implementation in volume of fluid and coupled volume of fluid with level set methods for bubble growth and detachment. *Int. J. Multiph. Flow*, 53:11–28, 2013.

[11] W. Yue, C.-L. Lin, and V. C. Patel. Numerical simulation of unsteady multidimensional free surface motions by level set method. *Int. J. Numer. Methods Fluids*, 42(8):853–884, 2003.

[12] S. Afkhami and M. Bussmann. Height functions for applying contact angles to 2D VOF simulations. *Int. J. Numer. Methods Fluids*, 57(4):453–472, 2008.

[13] Z. Yuan, M. Matsumoto, and R. Kurose. Directional migration of an impinging droplet on a surface with wettability difference. *Phys. Rev. Fluids*, 5(11):113605, 2020.

[14] Z. Yuan, J. Wen, M. Matsumoto, and R. Kurose. Anti-wetting ability of the hydrophobic surface decorated by submillimeter grooves. *Int. J. Multiph. Flow*, 131:103404, 2020.

[15] R. Cox. The dynamics of the spreading of liquids on a solid surface. Part 1. Viscous flow. *J. Fluid Mech.*, 168:169–194, 1986.

[16] A. Fath and D. Bothe. Direct numerical simulations of thermocapillary migration of a droplet attached to a solid wall. *Int. J. Multiph. Flow*, 77:209–221, 2015.

[17] S. F. Kistler. Hydrodynamics of wetting. In J. C. Berg, editor, *Wettability*, 311–430. Marcel Dekker New York, 1993.

[18] R. L. Hoffman. A study of the advancing interface. I. Interface shape in liquid—gas systems. *J. Colloid Interface Sci.*, 50(2):228–241, 1975.

[19] Š. Šikalo, H.-D. Wilhelm, I. Roisman, S. Jakirlić, and C. Tropea. Dynamic contact angle of spreading droplets: Experiments and simulations. *Phys. Fluids*, 17(6):062103, 2005.

[20] P. Xie, H. Ding, D. B. Ingham, L. Ma, and M. Pourkashanian. Analysis and prediction of the gas-liquid interfacial area for droplets impact on solid surfaces. *Appl. Therm. Eng.*, 178:115583, 2020.

[21] O. Voinov. Hydrodynamics of wetting. *Fluid dynamics*, 11(5):714–721, 1976.

[22] G.-S. Jiang and C.-W. Shu. Efficient implementation of weighted ENO schemes. *J. comput. phys.*, 126(1):202–228, 1996.

[23] U. Olgac, D. Izbassarov, and M. Muradoglu. Direct numerical simulation of an oscillating droplet in partial contact with a substrate. *Comput. Fluids*, 77:152–158, 2013.

[24] C. Shao, K. Luo, Y. Yang, and J. Fan. Direct numerical simulation of droplet breakup in homogeneous isotropic turbulence: the effect of the weber number. *Int. J. Multiph. Flow*, 107:263–274, 2018.

[25] M. Moradi, M. H. Rahimian, and S. F. Chini. Numerical simulation of droplet impact on vibrating low-adhesion surfaces. *Phys. Fluids*, 32(6):062110, 2020.

[26] S. Shin, J. Chergui, and D. Juric. Direct simulation of multiphase flows with modeling of dynamic interface contact angle. *Theor. Comput. Fluid. Dyn.*, 32(5):655–687, 2018.

[27] W. Li, J. Lu, G. Tryggvason, and Y. Zhang. Numerical study of droplet motion on discontinuous wetting gradient surface with rough strip. *Phys. Fluids*, 33(1):012111, 2021.

[28] D. Izbassarov and M. Muradoglu. Effects of viscoelasticity on drop impact and spreading on a solid surface. *Phys. Rev. Fluids*, 1(2):023302, 2016.

[29] V. Vaikuntanathan and D. Sivakumar. Maximum spreading of liquid drops impacting on groove-textured surfaces: Effect of surface texture. *Langmuir*, 32(10):2399–2409, 2016.

[30] D. Richard, C. Clanet, and D. Quéré. Contact time of a bouncing drop. *Nature*, 417(6891):811–811, 2002.

[31] A. U. Siddique, M. Trimble, F. Zhao, M. M. Weislogel, and H. Tan. Jet ejection following drop impact on micropillared hydrophilic substrates. *Phys. Rev. Fluids*, 5(6):063606, 2020.

[32] D. Vadillo, A. Soucemarianadin, C. Delattre, and D. Roux. Dynamic contact angle effects onto the maximum drop impact spreading on solid surfaces. *Phys. Fluids*, 21(12):122002, 2009.

[33] M. Gross, F. Varnik, and D. Raabe. Fall and rise of small droplets on rough hydrophobic substrates. *EPL (Europhys. Lett.)*, 88(2):26002, 2009.

[34] D. Hee Kwon and S. Joon Lee. Impact and wetting behaviors of impinging micro-droplets on superhydrophobic textured surfaces. *Appl. Phys. Lett.*, 100(17):171601, 2012.

[35] X. Chen and V. Yang. Thickness-based adaptive mesh refinement methods for multi-phase flow simulations with thin regions. *J. Comput. Physics*, 269:22–39, 2014.

[36] M. Baggio and B. Weigand. Numerical simulation of a drop impact on a superhydrophobic surface with a wire. *Phys. Fluids*, 31(11):112107, 2019.

Nomenclature

C	: VOF function [-]	β	: Spreading factor [-]
Ca	: Capillary number [-]	$\beta_{\max}$	: Maximum spreading factor [-]
D_0	: Initial droplet diameter [m]	Γ	: Half-thickness of the interface [-]
E_{m}	: Mass error [-]	Δ	: Mesh size [-]
$\boldsymbol{F}$	: Advection flux [-]	δ_Γ	: Delta function [-]
$\boldsymbol{F}_\sigma$	: Surface tension [N/m]	θ_{app}	: Apparent contact angle [°]
F_{H}	: Surface tension [N/m]	θ_{num}	: Numeric contact angle [°]
$\boldsymbol{g}$	: Gravitational acceleration [m/s^2]	θ_{Y}	: Young's contact angle [°]
K	: Microscopic length scale [m]	κ	: Surface curvature [1/m]
H_Γ	: Heaviside function [-]	μ	: Viscosity [mPa $\cdot$ s]
m_0	: Initial mass [kg]	ρ	: Density [kg/m^3]
m_{t}	: Mass at time t [kg]	σ	: Surface tension coefficient [N/m]
$\boldsymbol{n}$	: Normal vector [-]	τ	: Time step [s]
P	: Pressure [Pa]	φ	: Level-set function [-]
r	: Characteristic length [m]	ω	: Weight function [-]
$S_{(\varphi)}$	: Sign function [-]	**Subscripts**	
t	: Time [s]	a	Air
u	: Velocity in x- direction [m/s]	l	Liquid
$\boldsymbol{u}_{cl}$	: Contact line velocity [m/s]	$\parallel$	Parallel direction of groove
$\boldsymbol{u}_{ex}$	: Extension velocity [m/s]	$\perp$	Perpendicular direction of groove
v	: Velocity in y- direction [m/s]		
We	: Weber number [-]		

Chapter 3

Enhancing the surface hydrophobicity by introducing micro-scale structures

3.1 Introduction

In this chapter, the effect of micro-scale structures on the hydrophobicity of a surface is investigated using direct numerical simulation (DNS). The dynamcis of the air−liquid interface is captured by the coupled level-set and volume of fluid (CLSVOF) method proposed in chapter 2.

Hydrophobic surfaces have a wide range of applications, including self-cleaning [1], anti-icing [2, 3], and drag reduction [4]. By covering surfaces with chemical coatings having a low surface−free energy, artificial hydrophobic surfaces are fabricated [5]. However, these chemical layers are inevitably damaged in engineering projects and thus lead to the loss of surface hydrophobicity [5–7].

Hydrophobicity can also be amplified by masking surfaces with micro-scale pillars [8, 9] and grooves [10, 11]. For example, Patil et al. [12] found droplets undergo complete bouncing by masking a flat with pillars (pillar interval of between 0 μm and 76 μm). Liu et al. [13] reported the impinging droplet show a pancake bouncing behavior (behave

as superhydrophobic) on surfaces with micro-scale pillars (diameter of between 20 μm and 90 μm). This surface brings a fourfold reduction in the droplet-wall contact time compared with a conventional complete rebound. Malla et al. [14] showed the behavior of droplets changes from a non-bouncing to a complete bouncing when masking a flat with grooves (groove interval of between 0 μm and 76 μm). Guo et al. [15] observed that impacting droplets bounce off the surface (with 100 μm ridges and grooves) immediately in a petal-like shape, and the absence of a horizontal retraction process leads to $\sim$70% reduction in the contact time. These studies show that the surface hydrophobicity is largely enhanced by decorating with micro-scale pillars and grooves.

Some recent experimental studies demonstrate that larger rough structures enhance not only the hydrophobicity but also the robustness of surfaces. For example, Liu et al. [16] experimentally showed the robustness of the superhydrophobic surface with large pillars (pillar diameter of 150 μm $\sim$ 350 μm, and pillar interval of between 100 μm and 500 μm). Song et al. [17] also proved the robustness of surfaces masked with larger pillars (pillar diameter of between 200 μm and 1200 μm, and pillar space of between 100 μm and 500 μm). On these surface, liquid tends to impale the rough structures [12, 14], forming the Wenzel states [18] because of the large structures. It is generally agreed that the wetting in the Wenzel state weakens the water repellency of a textured surface. A better understanding of the factors (e.g., structure shape, structure size, and impact velocity) involved in the wetting state will enable the researchers and manufacturers to develop more robust hydrophobic surfaces with a broader range of emerging applications in the future.

In this chapter, therefore, the droplet dynamics on textured surfaces with micro-scale grooves are studied through a three-dimensional DNS. We aims to investigate the effect of the groove width (between 0μm and 400μm) and the impacting velocity (between 0m/s and 0.8m/s) on the surface hydrophobicity and the wetting state on a surface masked with larger micro-scale grooves. The results provide information for the study in the following chapters.

3.2 Problem statement

A schematic of the computational domain is shown in Fig. 3.1. A spherical water droplet with an initial diameter of $D_0 = 2$ mm is released on top of the substrate center with a droplet−wall distance of $D_0/2$ (release height) to make the droplet develop in a physical manner prior to touching the solid [19]. In the section of the substrate considered, W_G is the groove width ranging from 0 to 400 μm. The ridge width and groove depth are fixed at $W_R = 200$ μm and $D_G = 600$ μm, respectively. In addition, $\gamma = W_G/W_R$ is defined as the ratio of groove width. Thus, $\gamma = 0$ denotes the plain substrate with no groove decorations. The initial velocity (u_0) of the droplet varies between 0 to 0.8 m/s. Considering the large structure size and computational cost, the DNS is conducted on a uniform staggered Cartesian grid (grid size of $\Delta = 50$ μm) consisting of 320×240×320 grid points in the x-, y- and z- directions, respectively. In addition, the bottom boundary, which is regarded as the substrate, is set as a wall, and the surroundings are considered as shear-free surfaces. The gravitational force is considered as $\boldsymbol{g} = -9.8$ m/s^2 in the y-direction. Other physical properties [20] used are listed in Table 3.1.

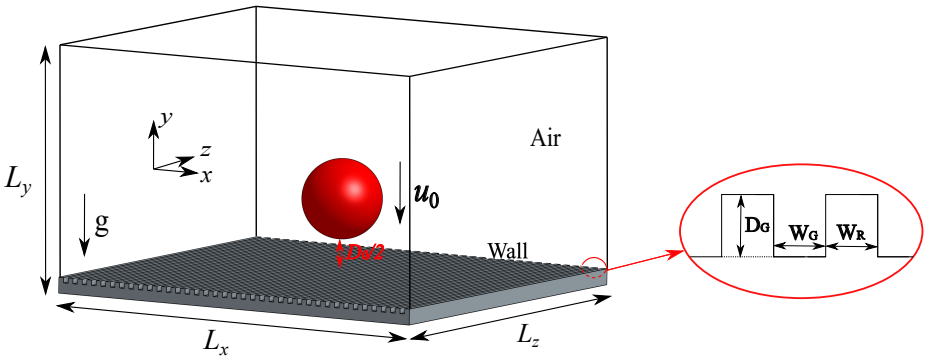

Figure 3.1: Schematic of computational domain and groove section.

Table 3.1: Physical properties of the droplet, surrounding air and the substrate.

D_0 (mm)	ρ_l (kg/m^3)	μ_l (mPa·s)	ρ_a (kg/m^3)	μ_a (mPa·s)	θ_Y (°)	σ (N/m)
2.0	1000	1.0	30	0.0183	$\pi/2$	0.0728

3.3 Results and discussion

3.3.1 Droplet shape comparison

The evolution of the droplet on surfaces with different values of γ is shown in Fig. 3.2. The first image for all cases is chosen at 2 ms owing to the release height. With an impact velocity of $u_0 = 0.6$m/s, the first touch between the droplet and the wall is at approximately $D_0/(2u_0) = 1.677$ ms. Hence, the images commence from 2 ms. From 2 to 13.5 ms, all droplets show impacting, spreading, retracting and bouncing behaviors. At the initial impacting and spreading stage from 2 to 5ms, the liquid expands radially and forms a droplet in a donut-like shape (see Fig. 3.3), reaching its maximum spreading state, when the maximum spreading diameter (D_m) is achieved. From 5 to 8 ms, the expanded liquid retracts to the impact center and tends to bounce off the surface after 8ms. At 13.5 ms, the droplets on surfaces with $\gamma = 1.5$ and $\gamma = 2.0$ have already left the substrate, whereas the liquid still touches the wall for surfaces with small grooves ($\gamma = 0.5$ and 1.0) and no grooves (plane surface with $\gamma = 0$). On surfaces with $\theta_Y \geq$

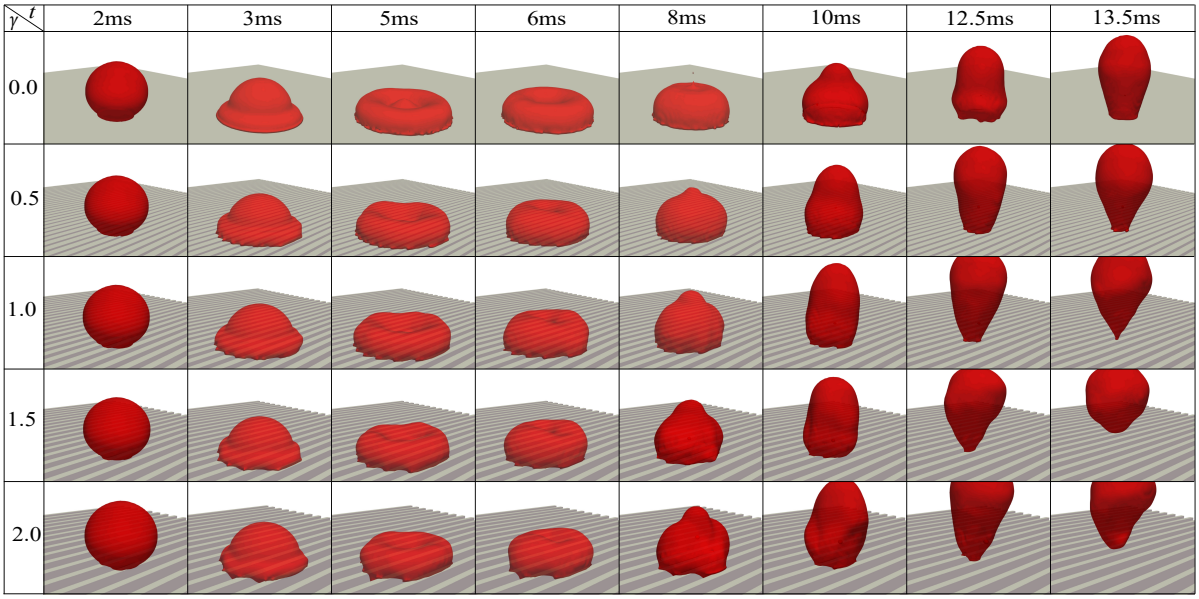

Figure 3.2: Comparison of time-elapsed droplet shape with different groove width ratios from $\gamma = 0.0$ to $\gamma = 2.0$ at a fixed initial impact velocity of u_0=0.6 m/s.

90°, theoretically, the Cassie model [21] (see Eq. (6.1)) shows that the apparent contact angle (θ_{app}) can be amplified by minimizing the solid fraction (increasing to γ in this work),

$$\cos\theta_{\text{app}} = f_{\text{s}}(1 + \cos\theta_{\text{Y}}) - 1 \tag{3.1}$$

where f_{s} is the liquid-solid fraction in the contact area. However, if f_{s} decreases excessively to zero, it will result in liquid penetration into the grooves, leading to a fully wet Wenzel state [18] on the textured surfaces. At 13.5 ms, compared with the droplet impinging on a surface with $\gamma = 1.5$, a larger tail is observed for a droplet on a surface with $\gamma = 2.0$. This is because, on a surface with large groove width ($\gamma = 2.0$), liquid penetrates into grooves and wets the surface completely (the Wenzel state [18]). The tail is formed when the submerged liquid leaves the surface. In summary, the hydrophobicity is enhanced with the increase in the groove width, but it is suppressed with a further increase in the groove width owing to the forming of the Wenzel state.

Symmetric spreading on a flat surface and asymmetric spreading on a groove structure are shown in Fig. 3.3. To characterize the spreading behavior of the droplet, we define β as the spreading factor, which is estimated by $\beta = D/D_0$, where D is the instantaneous spreading diameter. The maximum spreading factor (β_{max}) is obtained when liquid is at the maximum spreading stage with $D = D_{\text{max}}$. Here, $\beta_{\parallel}$ represents the spreading factor in the parallel groove direction, and $\beta_{\perp}$ is the spreading factor in

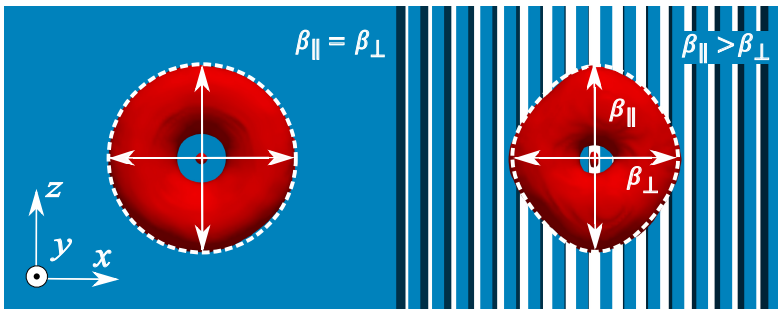

Figure 3.3: Comparison of the top view of droplets impinging on a flat surface (left, $\gamma = 0.0$) and the textured surface (right, $\gamma = 1.0$). Both surfaces exhibit a donut-like shape at approximately 6ms with initial velocity $u_0 = 0.6$ m/s.

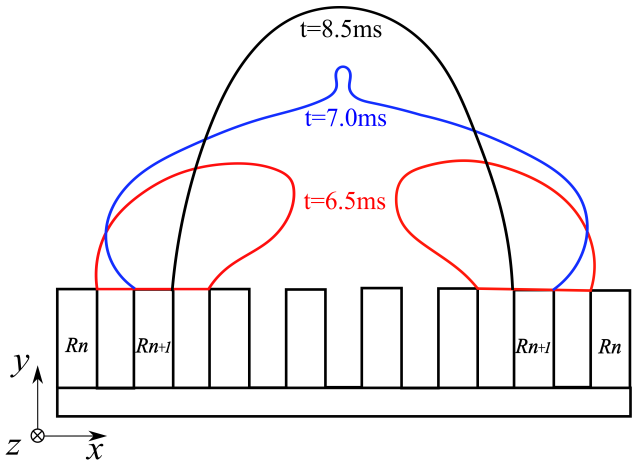

Figure 3.4: "Jump-stick" behavior of the droplet in the perpendicular groove direction with $\gamma = 1.0$ and $u_0 = 0.6$ m/s.

the perpendicular groove direction. On a flat surface ($\gamma = 0.0$), the appearance of the droplet is close to a perfect circle ($\beta_{\parallel} = \beta_{\perp}$). On the surface with groove structures ($\gamma = 1.0$), however, the droplet exhibits an elliptical shape, wherein the spreading factor in the parallel groove direction exceeds that in the perpendicular direction ($\beta_{\parallel} > \beta_{\perp}$). This occurs because the liquid spreads freely on solid ridges and grooves, whereas the spreading is hindered by the ridges in the perpendicular direction. The behavior of a liquid in the perpendicular direction is called a "jump-stick" [10] as shown in Fig.3.4. Three-phase contact line (TPCL) jumps from the touching ridge R_n to the next ridge R_{n+1} in the perpendicular direction from 6.5 ms (in red) to 7.0 ms (in blue) within only 0.5 ms. However, from the state in blue to the state in black (at 8.5 ms), much more time (1.5 ms) is needed, although the groove width W_G is equal to the ridge width W_R.

3.3.2 Wetting state

To study the effect of groove width on the wetting state of a droplet, the sectional images shown in Fig. 3.5 are compared, in which the Cassie state [21], the transition state (partially impaled state [22, 23]), and the Wenzel state [18] can be observed. For cases with $\gamma \leq 1.0$, a droplet simply spreads on the solid ridges with no liquid going into

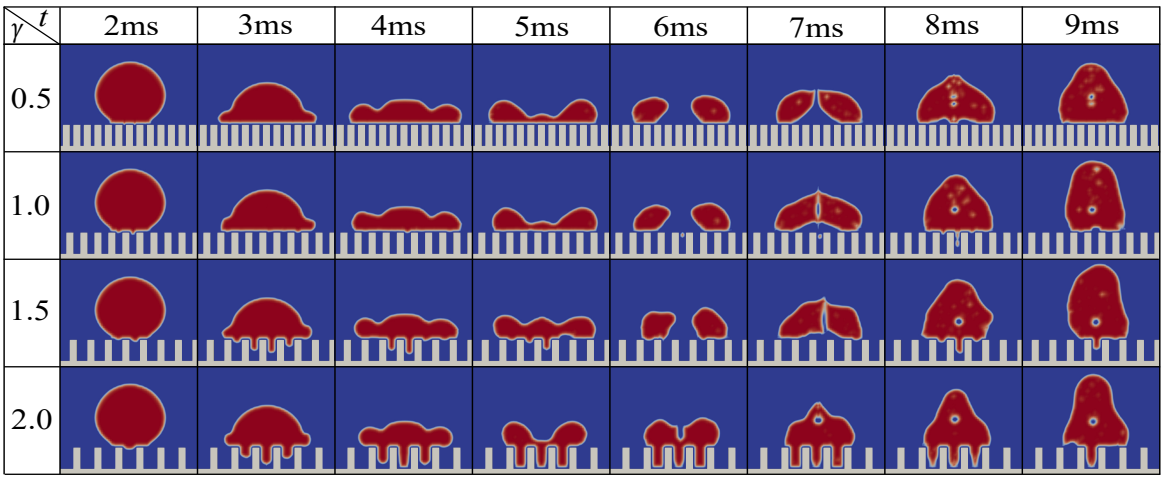

Figure 3.5: Cross-sectional view of droplet wetting states on textured substrates with $0.5 \leq \gamma \leq 2.0$ and $u_0 = 0.6$ m/s.

the grooves, exhibiting a Cassie state. When $\gamma = 1.5$, liquid penetrates into grooves and a transition state is formed at 3 and 4 ms. When the groove width ratio (γ) increases to 2.0, a significant amount of liquid falls into the groove and wets the structure completely, thereby leading to a Wenzel sate. This suggests that wetting states change gradually with an increase in the groove width. In particular, from 7 to 9 ms, the entrapment of a small air bubble is observed, which is caused by a retraction and convergence of an expanded liquid. This mechanism has been experimentally demonstrated [24], in which two compulsory conditions are proposed when achieving a bubble entrapment: formation of a deep air cavity close to the surface, and a fast recoiling of the liquid to seal the cavity at its center or top.

Figure 3.6 illustrates the two bubble entrapment mechanisms found in the present work. Prior to the bubble entrapment, at the maximum spreading stage, a deep air cavity in the center of the droplet is formed (see Fig. 3.5, at 6ms), and the liquid then starts to retract to the impact center. For the droplet impinging on the surface with $\gamma = 1.0$, the fast-retracting flows located at the top (1) and bottom (2) of the cavity entrap the air bubble in the cavity center. However, on the surface with $\gamma = 2.0$, the liquid (2) in grooves is arrested by structures. The fast-retracting flow (1) on the top captures

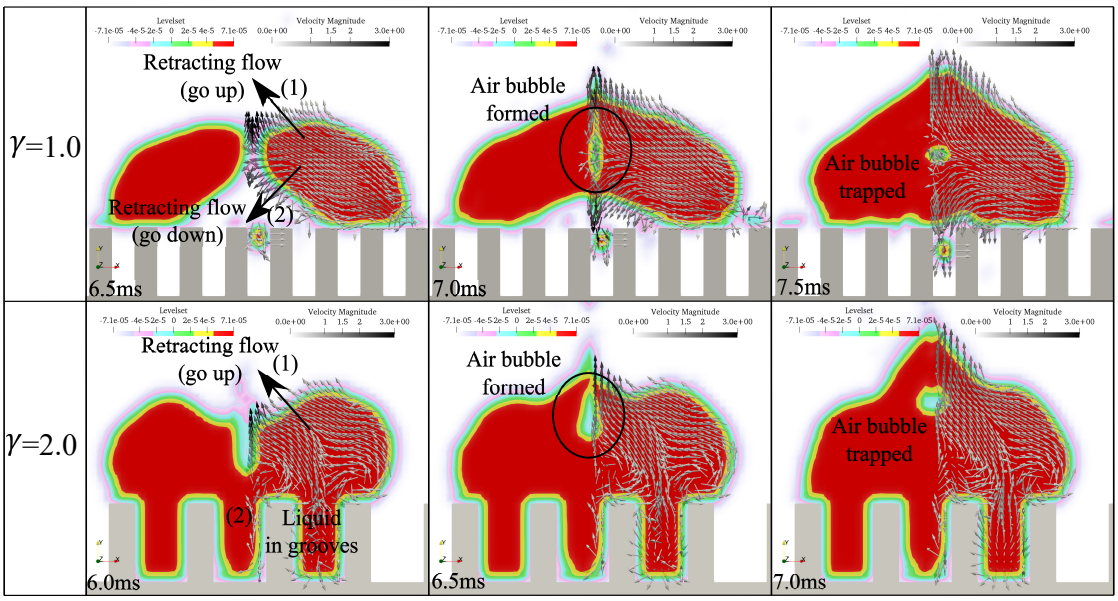

Figure 3.6: Different bubble trapping mechanisms on groove textured surfaces. (1) and (2) represent the upward and downward retracting flows, respectively.

an air bubble in the droplet center. In summary, two bubble entrapment mechanisms are found in this study, which is influenced by the droplet wetting state and the groove structure.

3.3.3 Spreading factor

3.3.3.1 Groove width effect

As mentioned above, asymmetric spreading on groove textured surfaces is demonstrated. To quantitatively show the droplet spreading behavior on textured surfaces, the spreading factor (β) in the parallel ($\beta_{\parallel}$) and perpendicular ($\beta_{\perp}$) groove directions are plotted as a function of time in Fig. 3.7. Both line charts are clearly divided into two parts, namely the impacting stage for the droplet quickly wetting the solid (a increase in β) and the bouncing stage for the liquid slowly leaving the substrate (a decrease in β). In detail, it takes approximately 4.5 ms for the droplet to reach its maximum spreading stage ($\beta_{\max}$ is obtained), and almost 10 ms is required to bounce and leave the surface.

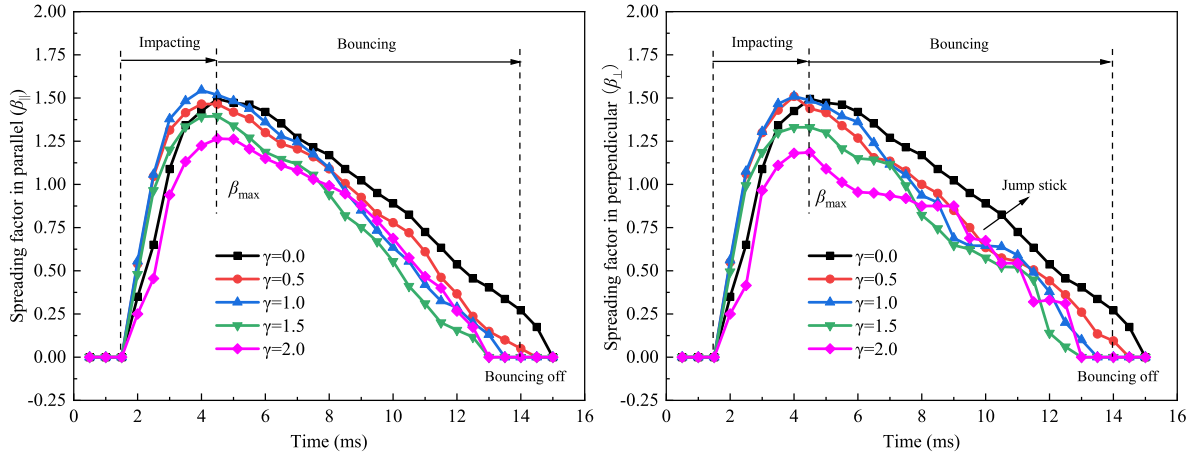

(a) β in groove parallel direction (b) β in groove perpendicular direction

Figure 3.7: Spreading factor (β) against time with different γ and constant u_0=0.6m/s: (a) β in groove parallel direction ($\beta_{\parallel}$); (b) β in groove perpendicular direction ($\beta_{\perp}$).

In both directions, in addition, the smallest $\beta_{\max}$ is obtained on a surface with $\gamma = 2.0$. Differences are also shown in parallel and perpendicular groove directions. First, $\beta_{\parallel} > \beta_{\perp}$ is demonstrated because of the asymmetric spreading. Second, the smooth increase and decrease of β are illustrated in the parallel groove direction, whereas lines in the bouncing stage exhibit a stepwise decrease behavior in the groove perpendicular direction. In particular, on the surface with a larger groove width ratio such as $\gamma = 2$, the clear stepwise decrease behavior corresponds to the "jump-stick" behavior shown in Fig. 3.4.

3.3.3.2 Impact velocity effect

Figure 3.8 shows the spreading factor (β) in the parallel ($\beta_{\parallel}$) and perpendicular ($\beta_{\perp}$) groove directions with the impact velocity varying from 0.0 to 0.8 m/s and a fixed $\gamma = 1.0$. The spreading factor is highly influenced by the impact velocity. A larger impact velocity leads to an early contact between the liquid and wall. In addition, the spreading factor increases with an increase in the impact velocity. Similar to the line shape in Fig. 3.3, the spreading factor in the parallel direction increases and decreases more smoothly than that in the perpendicular direction, thereby further confirming the "jump-stick"

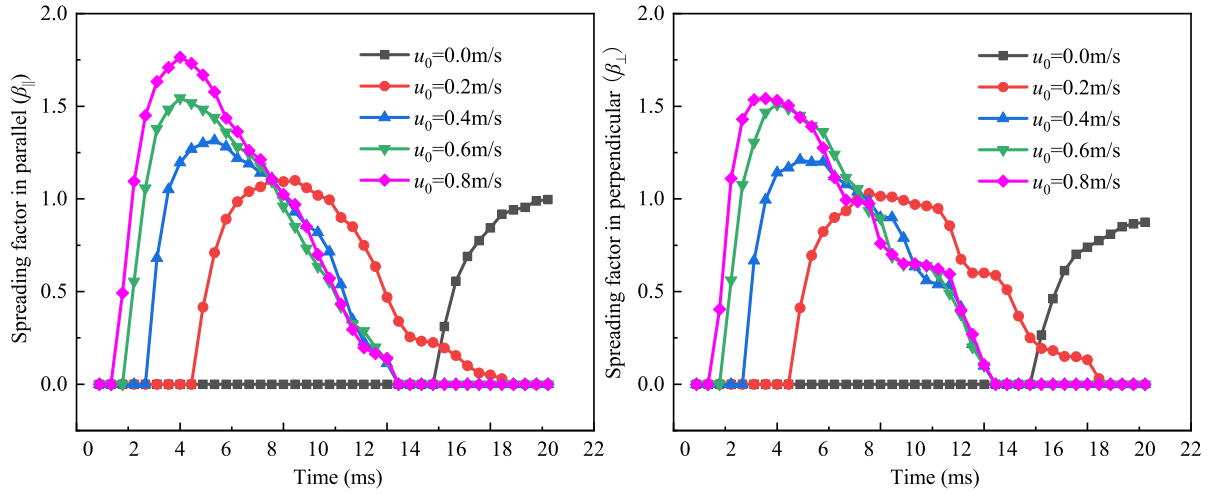

(a) β in groove parallel direction (b) β in groove perpendicular direction

Figure 3.8: Spreading factor (β) against time with different impinging velocity u_0 and constant $\gamma = 1.0$: (a) β in parallel groove direction ($\beta_{\parallel}$); (b) β in perpendicular groove direction ($\beta_{\perp}$).

behavior of droplets in the perpendicular direction.

3.3.4 Contact time

Figure 3.9 shows the contact time (t_c) between the liquid and wall, which is the time period from when the droplet first touches the surface to that when it bounces off the surface. Note that the cases of no liquid bouncing off the wall are not included. It is clear that the contact time decreases with an increase in the groove width ratio (γ) from 0.0 to 2.0. This result shows that the surface hydrophobicity is enhanced with the increase in γ. However, t_c increases with γ from 2.0 to 2.5. This occurs because, on a surface with large grooves, a liquid penetration takes place and forms a Wenzel state, thus weakening the surface hydrophobicity. In addition, no significant difference is found for droplets with different velocities. This behavior was also proposed by richard et al. [25], who revealed that, on a specific uniform surface, t_c is not dependent on the impact velocity u_0 but is a function of D_0, ρ, and σ [25]. Therefore, decorating the surface with grooves can improve the surface hydrophobicity, but it is weakened by a further increase in the

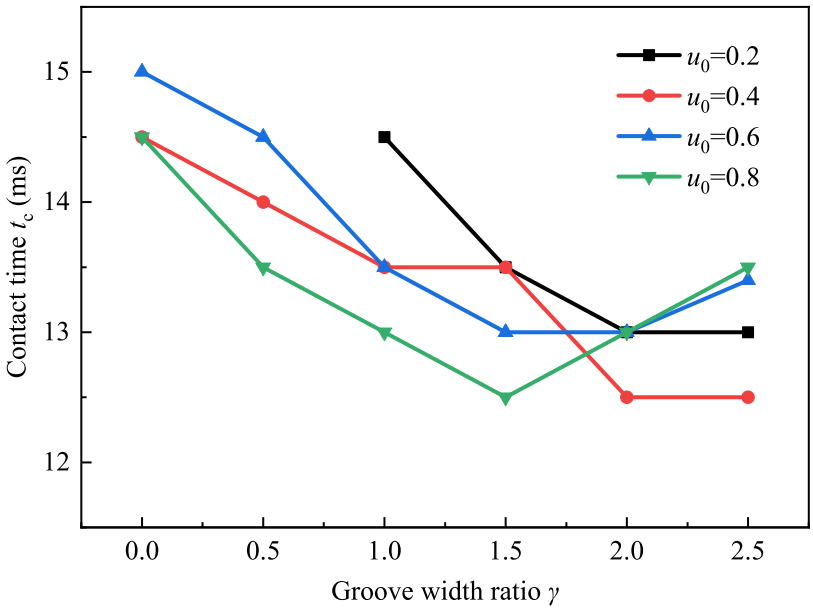

Figure 3.9: Contact time (t_c) between liquid and solid.

groove width.

We suggest that when developing hydrophobic surfaces by decorating them with grooved structures, both the solid fraction (f_s) and the wetting state should be considered. As the reason for this, although the contact time is smaller on surfaces with a larger groove width ratio such as $\gamma = 2.0$ and $\gamma = 2.5$, the liquid is entrapped in the grooves in a Wenzel state, leading to a loss of surface hydrophobicity. Hence, surfaces with $\gamma = 1.0$ and $\gamma = 1.5$ in the present work are good candidates when developing hydrophobic surfaces.

3.3.5 Phase diagram

Figure 3.10 summarizes the droplet bouncing states, where the bouncing (red circle) represents a droplet leaves on the surface, and no bouncing (black squares) describes the droplet pinned onto a substrate. The figure clearly shows the regions of bouncing and no bouncing cases. The diagram indicates that the bouncing behavior considerably depends on the initial velocity. No bouncing behavior is obtained for cases with $u_0 = 0.0$m/s,

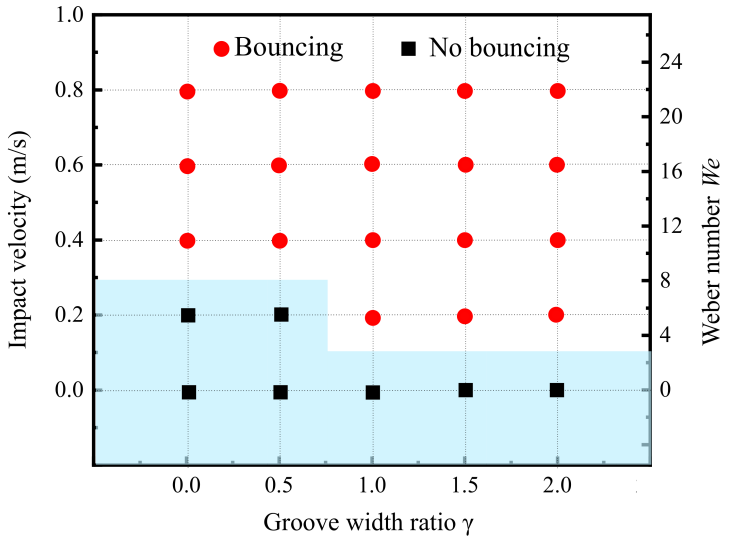

Figure 3.10: Bouncing states classified by bouncing (red circle) and no bouncing (black squares) behaviors.

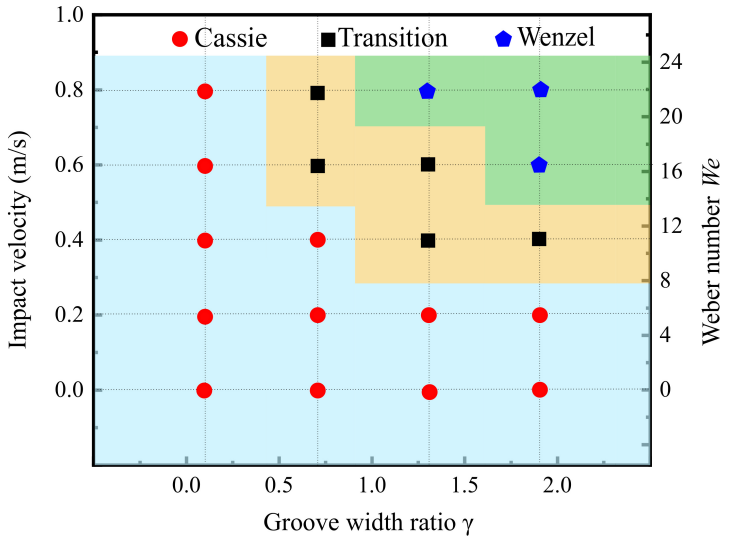

Figure 3.11: Wetting states classified by the Cassis state (red circle), transition state (black square), and Wenzel states.

whereas all droplets leave the surface when $u_0 \geq 0.4$ m/s. The bouncing behavior is also slightly affected by the groove width, i.e., bouncing occurs with an increase in γ when $u_0 = 0.2$ m/s.

In Fig. 3.11, the wetting states of droplets on a textured surface are classified by the Wenzel, transition, and Cassie states. The Cassis state (red circle) represents a droplet spreading on the ridges and not entering the groove. The Wenzel state (blue pentagon) indicates the liquid filling in the groove, and the transition state (black square) depicts air in the grooves partially replaced by the liquid. As shown in Fig. 3.11, a small groove width and small initial velocity lead to the Cassis state, whereas a large groove width and large impact velocity induce a droplet forming the Wenzel state. The present study provides an example, where hydrophobic surfaces are developed by masking with micro-scale grooves.

3.4 Conclusions

In this chapter, CLSVOF/DNS was applied to study the effect of micro-scale structures on the surface hydrophobicity and the wetting state. A total of 25 cases were setup and investigated by changing the groove width and the impinging velocity. The main results obtained in this chapter are summarized as follows.

1. Droplet spreads freely in the parallel groove direction, but it jumps from the attaching ridge to the next ridge in the perpendicular groove direction (called a "jump-stick"), leading to an elliptical droplet in the top-view.

2. Compared with the non-bouncing behavior of a droplet impinging on a flat surface, droplets completely bounce off when impinging on surfaces with a large groove width, revealing a enhanced surface hydrophobicity.

3. As the groove width increases, the droplet exhibits a shorter spreading factor and shorter contact time, meaning that the surface hydrophobicity is gradually enhanced. However, it is suppressed with a further increase in the groove width and the impact velocity, because the wetting transition from the Cassie state to the Wenzel state is obtained. This result demonstrates the surface hydrophobicity is weakened in the Wenzel state.

4. The wetting state of the droplet on a textured surface is determined based on the combined effect of the groove width and impact velocity. This finding provides information for following studies.

References

[1] Y.-Y. Quan, L.-Z. Zhang, R.-H. Qi, and R.-R. Cai. Self-cleaning of surfaces: the role of surface wettability and dust types. *Sci. Rep.*, 6:38239, 2016.

[2] S. Jung, M. K. Tiwari, N. V. Doan, and D. Poulikakos. Mechanism of supercooled droplet freezing on surfaces. *Nat. Commun.*, 3(1):1–8, 2012.

[3] S. Farhadi, M. Farzaneh, and S. Kulinich. Anti-icing performance of superhydrophobic surfaces. *Appl. Surf. Sci.*, 257(14):6264–6269, 2011.

[4] H. Park, G. Sun, and C.-J. Kim. Superhydrophobic turbulent drag reduction as a function of surface grating parameters. *J. Fluid Mech.*, 747:722–734, 2014.

[5] L. R. Scarratt, U. Steiner, and C. Neto. A review on the mechanical and thermodynamic robustness of superhydrophobic surfaces. *Adv. Colloid Interface Sci.*, 246:133–152, 2017.

[6] J. Jeevahan, M. Chandrasekaran, G. B. Joseph, R. Durairaj, and G. Mageshwaran. Superhydrophobic surfaces: A review on fundamentals, applications, and challenges. *J. Coat. Technol. Res.*, 15(2):231–250, 2018.

[7] K. Ellinas, A. Tserepi, and E. Gogolides. Durable superhydrophobic and superamphiphobic polymeric surfaces and their applications: A review. *Adv. Colloid Interface Sci.*, 250:132–157, 2017.

[8] D. Quéré. Wetting and roughness. *Annu. Rev. Mater. Res.*, 38:71–99, 2008.

[9] D. Quéré. Rough ideas on wetting. *Physica A*, 313(1-2):32–46, 2002.

[10] M. Kumar, R. Bhardwaj, and K. C. Sahu. Motion of a droplet on an anisotropic microgrooved surface. *Langmuir*, 35(8):2957–2965, 2019.

[11] V. Vaikuntanathan and D. Sivakumar. Maximum spreading of liquid drops impacting on groove-textured surfaces: Effect of surface texture. *Langmuir*, 32(10):2399–2409, 2016.

[12] N. D. Patil, R. Bhardwaj, and A. Sharma. Droplet impact dynamics on micropillared hydrophobic surfaces. *Exp. Therm. Fluid Sci.*, 74:195–206, 2016.

[13] Y. Liu, L. Moevius, X. Xu, T. Qian, J. M. Yeomans, and Z. Wang. Pancake bouncing on superhydrophobic surfaces. *Nat. Phys.*, 10(7):515–519, 2014.

[14] L. K. Malla, N. D. Patil, R. Bhardwaj, and A. Neild. Droplet bouncing and breakup during impact on a microgrooved surface. *Langmuir*, 33(38):9620–9631, 2017.

[15] C. Guo, D. Zhao, Y. Sun, M. Wang, and Y. Liu. Droplet impact on anisotropic superhydrophobic surfaces. *Langmuir*, 34(11):3533–3540, 2018.

[16] C. Liu, H. Zhan, J. Yu, R. Liu, Q. Zhang, Y. Liu, and X. Li. Design of superhydrophobic pillars with robustness. *Surf. Coat. Technol.*, 361:342–348, 2019.

[17] J. Song, L. Huang, C. Zhao, S. Wu, H. Liu, Y. Lu, X. Deng, C. J. Carmalt, I. P. Parkin, and Y. Sun. Robust superhydrophobic conical pillars from syringe needle shape to straight conical pillar shape for droplet pancake bouncing. *ACS Appl. Mater. Interfaces*, 11(48):45345–45353, 2019.

[18] R. N. Wenzel. Resistance of solid surfaces to wetting by water. *Ind. Eng. Chem.*, 28(8):988–994, 1936.

[19] I. Malgarinos, N. Nikolopoulos, M. Marengo, C. Antonini, and M. Gavaises. VOF simulations of the contact angle dynamics during the drop spreading: Standard models and a new wetting force model. *Adv. Colloid Interface Sci.*, 212:1–20, 2014.

[20] Y. Wang, G. Amberg, and A. Carlson. Local dissipation limits the dynamics of impacting droplets on smooth and rough substrates. *Phys. Rev. Fluids*, 2(3):033602, 2017.

[21] A. Cassie and S. Baxter. Wettability of porous surfaces. *Trans. Faraday Soc.*, 40:546–551, 1944.

[22] M. Gross, F. Varnik, and D. Raabe. Fall and rise of small droplets on rough hydrophobic substrates. *EPL (Europhys. Lett.)*, 88(2):26002, 2009.

[23] D. Hee Kwon and S. Joon Lee. Impact and wetting behaviors of impinging micro-droplets on superhydrophobic textured surfaces. *Appl. Phys. Lett.*, 100(17):171601, 2012.

[24] L. Chen, L. Li, Z. Li, and K. Zhang. Submillimeter-sized bubble entrapment and a high-speed jet emission during droplet impact on solid surfaces. *Langmuir*, 33(29):7225–7230, 2017.

[25] D. Richard, C. Clanet, and D. Quéré. Contact time of a bouncing drop. *Nature*, 417(6891):811–811, 2002.

Nomenclature

D	: Instantaneous spreading diameter [m]	β	: Spreading factor [-]
D_0	: Initial droplet diameter [m]	γ	: Groove width ratio [-]
D_{G}	: Groove depth [m]	Δ	: Mesh size [-]
f_{s}	: Solid fraction [-]	θ_{app}	: Apparent contact angle [$^\circ$]
$\boldsymbol{g}$	: Gravitational acceleration [m/s^2]	θ_{Y}	: Young's contact angle [$^\circ$]
t	: Time [s]	μ	: Viscosity [mPa $\cdot$ s]
t_c	: Contact time [s]	ρ	: Density [kg/m^3]
u_0	: Initial velocity [m/s]	σ	: Surface tension coefficient [N/m]
We	: Weber number [-]	**Subscripts**	
W_{G}	: Groove width [m]	a	Air
W_{R}	: Ridge width [m]	l	Liquid
		max	Maximum value
		$\parallel$	Parallel direction of groove
		$\perp$	Perpendicular direction of groove

Chapter 4

Manipulating the rebound direction of a droplet by surfaces with roughness gradient

4.1 Introduction

In chapter 3, it was found that the surface hydrophobicity is enhanced by masking with uniform micro-scale grooves, and a larger groove width leads to a greater surface hydrophobicity. However, it is suppressed with further increasing the groove width because of the liquid penetration and the obtaining of the Wenzel state. If the surface is decorated with nonuniform grooves, how will the droplet behave? In this chapter, we focus on a surface with nonuniform grooves, and the effects of the Weber number, groove depth, and groove width on the droplet dynamics are investigated using direct numerical simulation (DNS).

In contrast to their symmetrical response on homogeneous surfaces (with uniform decorations), droplets on heterogeneous surfaces (with nonuniform decorations) may exhibit asymmetric spreading and directional migration behaviors [1]. This technology is useful in areas including the fabrication of microfluidic devices [2, 3], water harvesting [4], anti-icing [5], and self-cleaning [6]. Heterogeneous surfaces are usually fabricated by

masking with nonuniform micro-scale structures [7, 8] and the chemical coatings [9]. Because the chemical layer is easily damaged by abrasion or erosion during long-term operation, masking with micro-scale structures is a better approach to the design of heterogeneous surfaces. [7, 10–12].

Some researchers have found that a gently released droplet (not impinging droplets) spontaneously transports to an area with dense structures. For instance, Fang et al. [13] showed that, on a surface with nonuniform pillars, the motion of the droplet is controlled in the desired direction. Shastry et al. [14] demonstrated that droplets are propelled down gradients fabricated by micropillars. Yang et al. [15] constructed textured surfaces with nonuniform grooves, upon which the spontaneous transport of a single droplet along the groove direction was found. Liu et al. [7] also designed several nonuniform groove textured surfaces, which afforded the directional and long-range transport of droplets following the roughness gradient. By controlling the groove density and orientation, Wu et al. [16] found that the rapid transport of droplets are realized without the use of an external power sources. These studies demonstrate that the motion of a gently released droplet is controllable by nonuniform structures, and the direction of the self-motion is from the area with sparse structures toward an area with dense structures (following the roughness gradient).

For an impinging droplet, however, does it always move following the roughness gradient? This question was experimentally explored by Wu et al. [17], who masked the surface with micropillars, upon which two types of movement were found, namely, following and against the roughness gradient. The droplet moved in the direction of increasing pillar density in a perfect Wenzel [18] or Cassie [19] states, whereas an opposite self-migration behavior was observed for droplets in a partial Wenzel state. Reyssat et al. [20] also found that droplets rebounded obliquely when impinged on a substrate with a roughness gradient. Malouin et al. [21] proposed a surface with nonuniform pillars, which was able to control the placement and trajectory of the impinging droplets. To the best of our knowledge, however, the droplet rebound behavior on a substrate with a roughness gradient has yet to be fully studied, particularly on surfaces with micro-scale

grooves, which can easily be fabricated over large areas [22].

Because the droplet deformation on a surface with a roughness gradient is a highly transient process, and its mechanism is difficult to probe through experimental observations alone, several numerical investigations have been reported. Using a particle-based numerical method, Zhao et al. [24] showed two possible types of droplet motion on a pillar-decorated surface: movement along the roughness gradient in a Cassie state, and movement against a roughness gradient in a partial Wenzel state. Wang et al. [25] numerically found that the main reason for the different motions is the asymmetric penetration of the liquid into the grooves. Using a lattice Boltzmann simulation, Zhang et al. [26] demonstrated that the rebound trajectory of droplets is determined by the competition of the lateral recoil of the liquid, as well as the asymmetric penetration into and the asymmetric capillary emptying from grooves. However, the above studies only consider a fictitious liquid droplet.

In this study, therefore, a droplet at a real scale is employed, and its dynamics are tracked using a coupled level-set and volume of fluid (CLSVOF) method based a three dimensional DNS. The effect of the impingement velocity (u_0), groove width (W_G), and groove depth (D_G) on its rebounding directions is studied when impinging on a surface with a roughness gradient. The roughness gradient is developed by gradually varying the groove width (W_G). We first examine the effect of the impingement velocity or Weber number, $We = (\rho D_0 u_0^2)/\sigma$, where ρ represents the density, D_0 is the initial droplet diameter, and σ is the surface tension coefficient at the liquid$-$air interface (σ=72.8$\times 10^{-3}$ Nm^{-1}). Further simulations are conducted to study the effect of the groove width (W_G). Finally, the influence of the groove depth (D_G) is examined.

4.2 Problem statement

A schematic of the computational domain, constructed using a uniform staggered 320 × 300 × 320 grid with grid size of $\Delta = 32$ μm in all three directions, is shown in Fig. 4.1(a). A spherical water droplet with $D_0 = 63\Delta$ (approximately 2 mm) is located above the center of the substrate. The distance (d) between the top of the ridges and the droplet in Fig. 4.1(b) is set to 10Δ (0.32mm), and thus the droplet evolves physically before touching the solid.

A surface with nonuniform grooves is placed on the bottom, where the ridge width (W_{R}) is fixed at 160 μm, and the roughness gradient is characterized by the varying groove width (W_{G}) as $n{\cdot}\Delta$, where n is a natural number. The cross-sectional view in Fig. 4.1(b) shows the groove widths W_{G1} and W_{G2} on the left and right sides of the impingement center. According to the results described in Chapter 3, three droplet wetting states were obtained for We ranging from 0.0 to 30.0 and a groove width ratio of between 1.0 and 2.0. Here, the groove width ratio (γ) is redefined as $\gamma = W_{\mathrm{G2}}/W_{\mathrm{R}}$, varying from 1.4 to 2.2 to investigate the effect of the groove width on the droplet

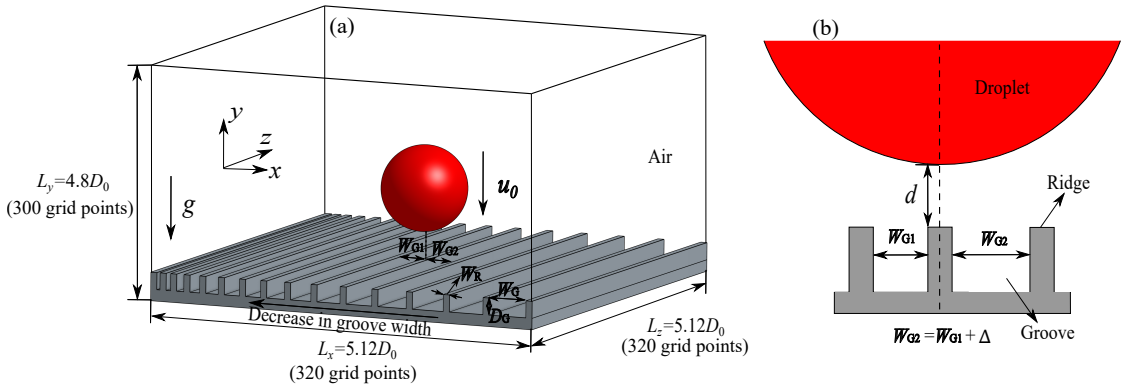

Figure 4.1: Schematic of the computational domain: (a) computational domain, where W_{R}, W_G, and D_{G} are the ridge width, the groove width (varying), and the groove depth, respectively; (b) cross-sectional view of the impingement, where W_{G1} and W_{G2} are the groove width in the left and right sides of the impingement center ($W_{\mathrm{G2}} = W_{\mathrm{G1}} + \Delta$), respectively. The black dashed line in (b) represents the impingement center.

Table 4.1: Parameters used in the simulations.

Parameter	Symbol	Value
Intrinsic contact angle (°)	θ_{Y}	100
Ridge width (μm)	W_{R}	160
Groove width (μm)	W_{G}	$n{\cdot}\Delta$
Groove width ratio	γ	1.4/1.8/2.2
Groove depth ratio	α	2.4/3.6/5.0
Weber number	We	1-30
Impact velocity (m/s)	u_0	0.19-1.04

movement direction. To investigate the influence of groove depth, the groove depth ratio $\alpha = D_{\mathrm{G}}/W_{\mathrm{R}}$ is varied from 2.4 to 5.0. The detailed simulation parameters are shown in Table 4.1, where the intrinsic contact angle is adopted as 100°, which is close to the value (101°) of the static contact angle for water on a uniform fluorocarbon substrate [17]. In addition, a gravitational acceleration $|\boldsymbol{g}|$ of 9.8 m/s^2 is imposed.

4.3 Results and discussion

Simulations are first conducted to examine the effect of the Weber number, in which the detailed physical insights into directional rebounding are presented. Groove depth influences are then discussed, and further simulations are conducted to understand how the groove width affects the droplet transportation directions.

4.3.1 Effect of Weber number

On textured surfaces, the wetting state has a significant effect on the transport direction of droplets [17, 21, 22]. For an impinging droplet, its wetting state depends on the combined effects of the dynamic pressure (wetting pressure), $P_{\mathrm{D}}=\rho_l u_0^2/2$; the capillary effect (antiwetting pressure), $P_{\mathrm{C}}=-2\sigma\cos\theta_a/W_{\mathrm{G}}$; and the effective water hammer pressure, $P_{\mathrm{WH}}=k\rho_l C_s u_0$ (see Fig. 4.2). Here, θ_a is the advancing contact angle that can be estimated every time step by the apparent contact angle model described in Chapter 2, k represents the water hammer pressure coefficient, which is fixed at 5×10^{-4} according to [27] owing to the small u_0, and C_{s} is the speed of sound in water, i.e., C_{s}=1480 m/s.

Figure 4.3 shows the effects of We and the groove width (W_{G})on the dynamic pressure

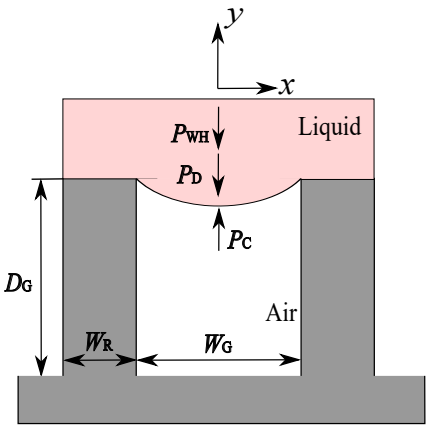

Figure 4.2: Schematic of the air−liquid meniscus on a groove. The shape of the meniscus is determined by the combined effects of the wetting pressure (P_{D}), capillary pressure (P_{C}), and water hammer pressure (P_{WH}).

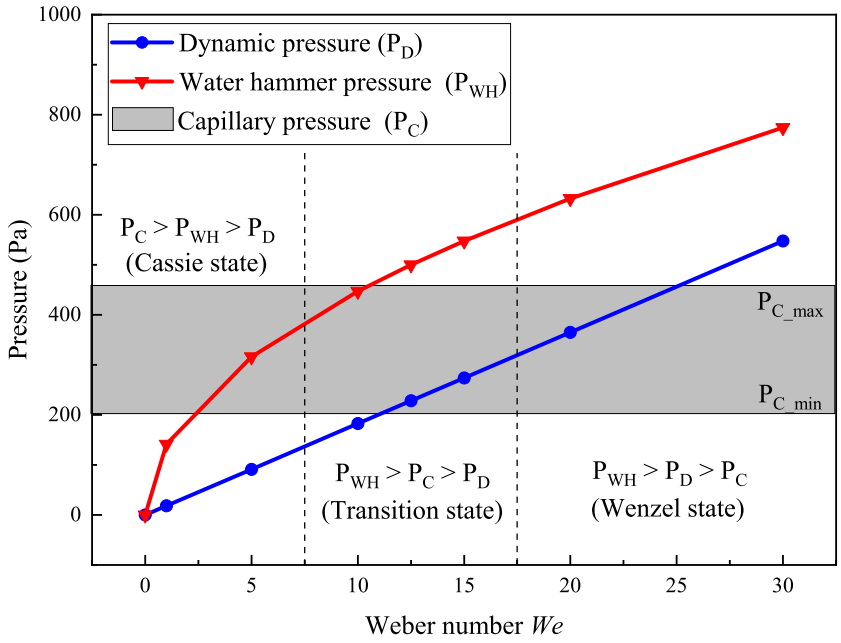

Figure 4.3: Comparison of dynamic pressure (P_{D}), capillary pressure (P_{C}), and effective water hammer pressure (P_{WH}) against the Weber number (We). The grey region represents the P_{C} owing to the roughness gradient. In addition, $P_{\mathrm{C\_max}}$ and $P_{\mathrm{C\_min}}$ are the maximum and maximum values of P_{C}.

(P_{D}), the capillary pressure (P_{C}), and the effective water hammer pressure (P_{WH}). On the surface with a roughness gradient, the capillary pressure is not uniform but decreases with an increase in groove width. In Fig. 4.3, the maximum ($P_{\mathrm{C\_max}}$) and minimum ($P_{\mathrm{C\_min}}$) capillary pressures are estimated based on the wetted groove width, which corresponds to a minimum W_{G} of 160 μm and a maximum W_{G} of 352 μm. Based on a comparison of P_{D}, P_{C}, and P_{WH}, the condition is roughly divided into three regions against We, and we expect to observe the corresponding wetting state and the motion direction for each region.

According to the snapshots shown in Fig. 4.4, three types of droplet rebounding behavior (vertical rebound and rebound following or against the roughness gradient) are observed with $1 \leq We \leq 15$, $\alpha = 3.6$, and $\gamma = 1.6$. First, we present the unbalanced Young's force [17, 28], $dF_{\mathrm{Y}} = \sigma(\cos\theta_{\mathrm{L}} - \cos\theta_{\mathrm{R}})dz$, where dz is the length of the TPCL,

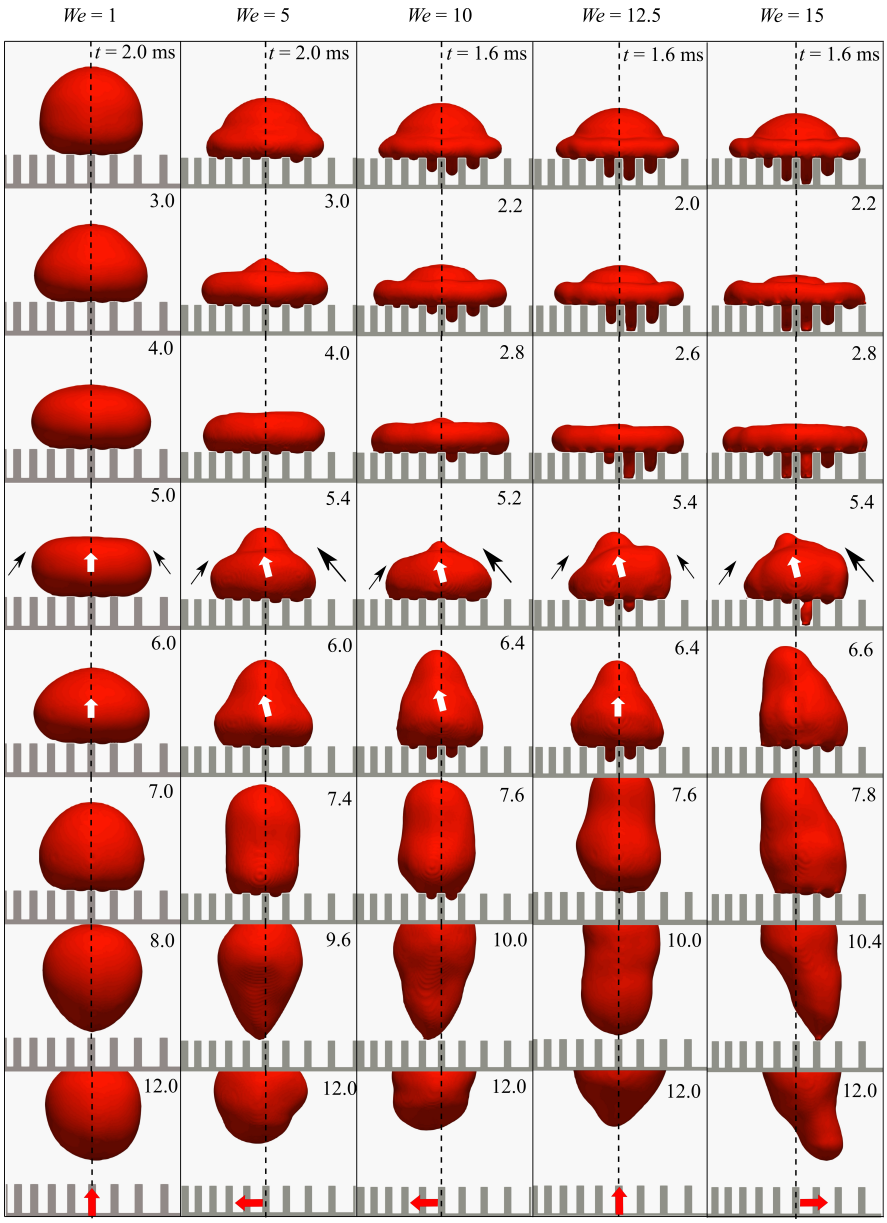

Figure 4.4: Time evolution of impinging water droplet with We ranging from 1 to 15, $\alpha = 3.6$, and $\gamma = 1.8$. The black arrows, white arrows, and red arrows indicate the local motion direction, the head motion direction, and the final rebound direction of the droplets, respectively. The black dashed lines represent the droplet impact center.

θ_L and θ_R are the receding contact angles on the left and right side of the impingement center, respectively. From this equation, an unbalanced Young's force is obtained on the

surface with roughness gradient (leading to $\theta_L \neq \theta_R$), which drives the droplet to move spontaneously. At a smaller We of 1, the droplet tends to rebound vertically owing to the small difference in the contact angle ($\theta_L - \theta_R$). For $We = 5$ and 10, the droplet rebounds leftward following the roughness gradient because of $\theta_L < \theta_R$. Therefore, in a perfect Cassie state ($P_C > P_{WH} > P_D$) and a transition state (partially impaled state [29, 30]) ($P_{WH} > P_C > P_D$), a larger groove width on the right side leads to a larger contact angle difference ($\theta_R > \theta_L$); thus, the net force toward the left drives the droplet to rebound following the roughness gradient. However, the droplet rebounds in the opposite direction, against the roughness gradient, when $We \geq 15$. For a larger We, the right side of the droplet penetrates the groove space, showing a partial Wenzel state ($P_{WH} > P_D > P_C$), whereas the left side remains in a Cassie state as a result of the small W_G. The different wetting states result in different contact angles on the left and right, and thus an unbalanced Young's force. In addition, the liquid in a Cassie state easily detaches from the substrate, whereas much of the liquid on the right side remains in the grooves. The mobility of the liquid on the right side is slower than that on the left, indicating that the droplet is arrested by the grooves (capillary emptying force) and cannot move further [23]. Hence, the unbalanced Young's force and the coexistence of the Cassie and Wenzel states induce the droplet to rebound against the roughness gradient (to the right side) at 10.4 ms. Interestingly, the droplet shows no clear rebounding direction at the critical We value of 12.5. This manner is caused by the balanced forces between the Young's force and the capillary emptying force. In addition, the rebound height of droplets at 12 ms increases with an increase in We from 1 to 12.5. In summary, on surfaces with a roughness gradient, the direction of the droplet movement depends on the combined effects of the unbalanced Young's force and the wetting state, which differs from those of a gently released droplet or a droplet impinging on a chemically heterogeneous surface, where only the unbalanced Young's force is relevant.

The Cassie state is obtained when a droplet impinges on textured surfaces with a small We, meaning a small P_{WH}, whereas a partial Wenzel state appears on the right side of the droplet for a larger We. To thoroughly investigate the relationship between

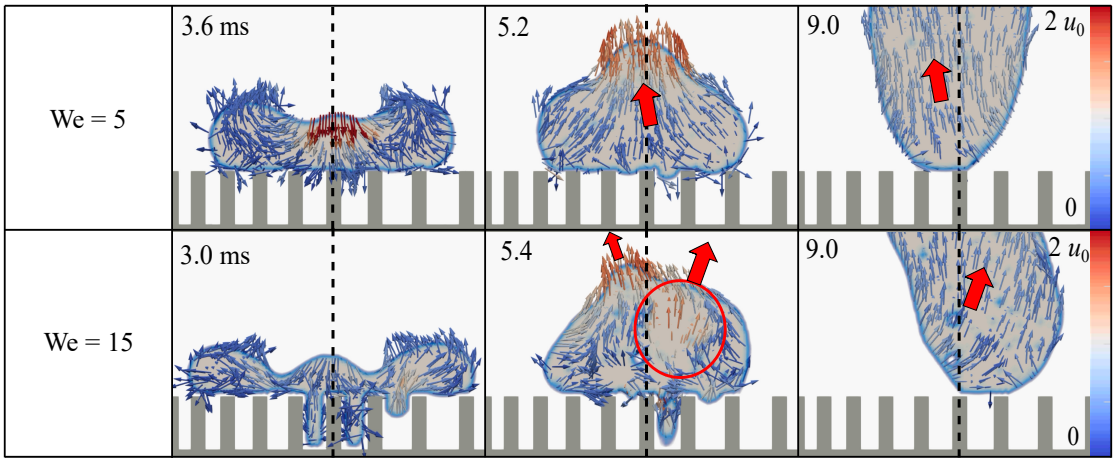

Figure 4.5: Cross-sectional view of the velocity field inside rebounding droplets following ($We = 5$) and against ($We = 15$) the roughness gradient. The color of the arrows in the droplets indicate the velocity magnitude ranging from 0 m/s to 2 u_0.

We and the droplet rebound behaviors, the velocity fields at the maximum spreading stage, recoil stage, and rebound stage are shown in Fig. 4.5. Although the maximum velocity inside the droplet can be several times the initial impinging velocity owing to the jet ejection [31], here we limit the range between 0 m/s and 2 u_0 in Fig. 4.5. For a small We, the recoiling flow is directed to the left owing to the unbalanced Young's force in the lateral direction, which drives the rebounding liquid to migrate along the roughness gradient. For a larger We, the partial Wenzel state is obtained. Although the top of the retracting liquid tends to rebound following the roughness gradient, much of the liquid in the red circle is transported rightward against the roughness gradient at 5.4 ms owing to the capillary emptying force of the liquid in the grooves; thus, the droplet finally rebounds against the roughness gradient.

Figure 4.6 shows the lateral displacement of the impinging droplet for various values of We. The displacement is evaluated using the contact line position on the top of the ridges in the cross-sectional view, which is positive toward the right (R.) and negative toward the left (L.) of the impinging center. The lines in Fig. 4.6 are roughly divided against time based on the three phases of spreading, retracting, and rebounding [32]. In

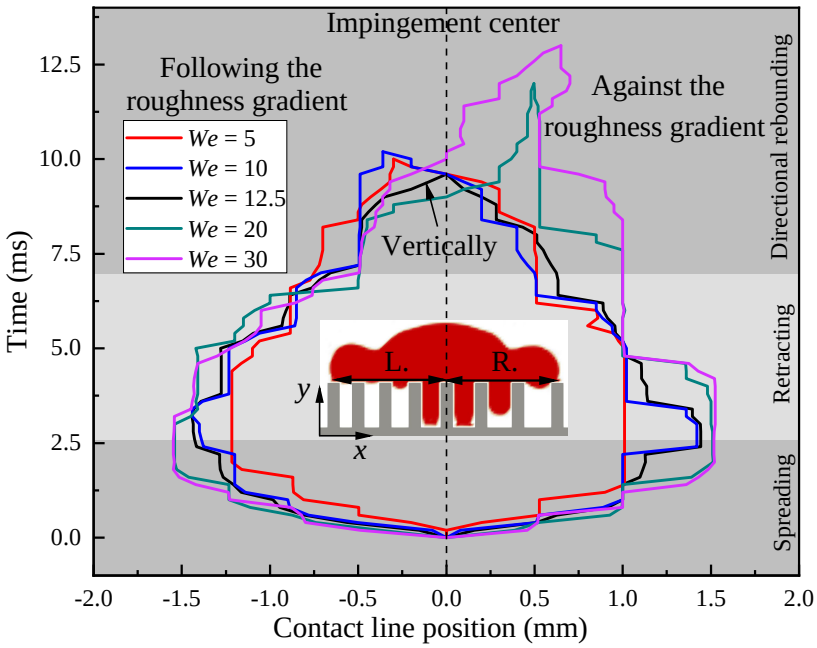

Figure 4.6: Contact line position ($x-$ axis) of the impinging droplet on the ridges. The black dashed line represents the impingement center in Fig. 4.1(b).

addition, three types of rebounding behaviors are observed according to the impingement center. For We values of 5 and 10, the droplet rebounds leftward following the roughness gradient owing to the unbalanced Young's force in the lateral direction. For the critical We of 12.5, no obvious displacement is observed because the Young's force and the capillary emptying process are balanced, and thus the droplet leaves the surface vertically. For a larger We, a rebounding against the roughness gradient occurs because of the combined effects of the unbalanced Young's force and the coexistence of the Cassie and Wenzel states. In addition, a larger We results in a much larger displacement of a droplet from its initial impact position.

To rationalize these observations, in Fig. 4.7 we estimate the translational momentum (P_x) of the departing droplet (at the moment it leaves the surface) along the $x-$ axis, $P_x = \sum_{i,j,k}^{320\times240\times320} m_{i,j,k}u_{x,i,j,k}$, where $m_{i,j,k}$ is the mass value in each cell computed based on the VOF function (C), and $u_{x,i,j,k}$ is the velocity in the $x-$ direction at the cell (i, j, k). The negative P_x within a small range of We suggests that the droplet tends

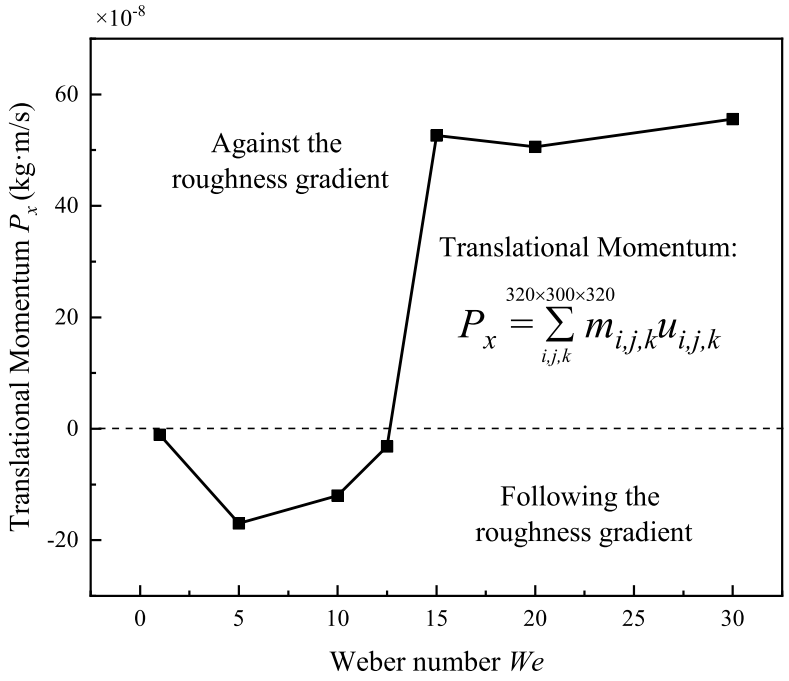

Figure 4.7: Translational momentum (P_x) of the departing droplet under a different We.

to move leftward following the roughness gradient. By contrast, the positive P_x illustrates an opposite rebound tendency against the roughness gradient, but no significant difference of P_x can be observed for We ranging from 15 to 30, which is caused by the wetting transition from a Cassie state to a Wenzel state even for areas with a small groove spacing. For $We = 1$ and 12.5, $|P_x|$ is extremely small and the droplet shows no clear rebounding directions shown in Fig. 4.4.

In addition, apart from the lateral transportation of droplets induced by the combined effects of an unbalanced Young's force and a dynamic wetting state, a rotating motion is also observed by computing the angular momentum ($\boldsymbol{L}_z$) with respect to the z-axis rotation shown in Fig. 4.8. Here, $\boldsymbol{L}_z$ is estimated by the cross product of the cell position (such as the cell (i, j, k)) vector $\boldsymbol{r}_{i,j,k}$ (with respect to the z-axis passing through the droplet center of mass O) and its linear momentum vector $\boldsymbol{P}_{i,j,k} = m_{i,j,k}\boldsymbol{u}_{i,j,k}$; thus, $\boldsymbol{L}_z = \sum_{i,j,k}^{320\times300\times320} \boldsymbol{r}_{i,j,k}\boldsymbol{P}_{x,i,j,k}$ for the 3-D droplet. Based on the right-hand rule, the negative L_z in Fig.8 indicates counterclockwise rotating behavior of the droplets. For a

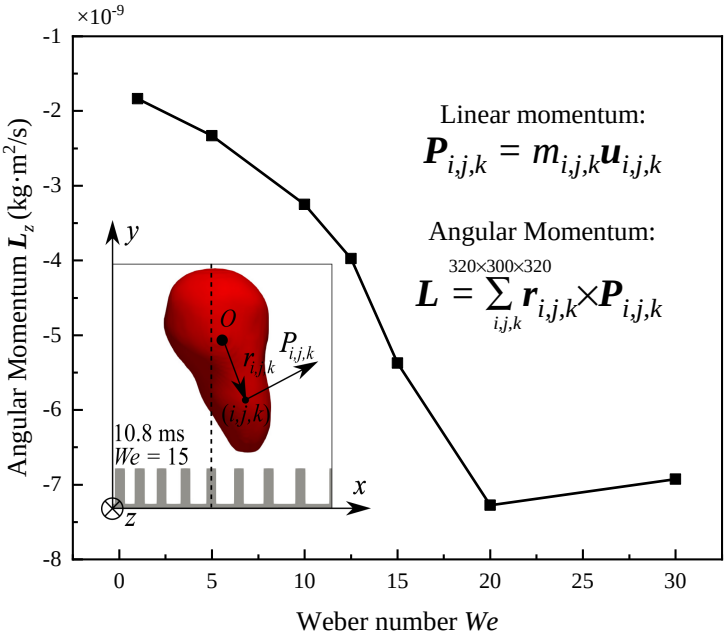

Figure 4.8: Z component ($\boldsymbol{L}_z$) of angular momentum of the leaving droplet under a different We.

We of 1 to 20, a significant amount of liquid floating on the patterns spreads around and wets an increasing number of ridges. Because the surface tension tends to minimize the free surface of the droplet, the asymmetric retracting flow triggers an increase in $|\boldsymbol{L}_z|$. For a We ranging between 20 and 30, however, much of the liquid infiltrates into the grooves, and the liquid is arrested by the ridges. Hence, $|\boldsymbol{L}_z|$ shows a decreasing tendency owing to the Cassie-to-Wenzel wetting transition, illustrating a weakened rotating motion.

4.3.2 Effect of groove depth

As mentioned above, the coexistence of the Cassie and Wenzel states plays a critical role in the rebound direction of an impinging droplet. On a surface with micro-scale structures, therefore, the groove depth (D_{G}) is a non-negligible factor in the droplet wetting state. The effect of D_{G} can be described using a touch-down scenario [33]. A droplet undergoes an impalement transition such as the transition from a Cassie to a Wenzel state if the pressure in the droplet exceeds the critical impalement pressure,

$\min(P^{\mathrm{T}}_{\mathrm{imp}}, P^{\mathrm{S}}_{\mathrm{imp}})$, where $P^{\mathrm{T}}_{\mathrm{imp}}$ is the touch-down pressure, $P^{\mathrm{T}}_{\mathrm{imp}} \sim \frac{\sigma D_{\mathrm{G}}}{(W_{\mathrm{G}}+W_{\mathrm{R}})^2}$, and $P^{\mathrm{S}}_{\mathrm{imp}}$ is the sliding pressure, $P^{\mathrm{S}}_{\mathrm{imp}} = \frac{2f_{\mathrm{s}}}{1-f_{\mathrm{s}}}|\cos(\theta_a)|\frac{2\sigma}{W_{\mathrm{R}}}$, where $f_{\mathrm{s}} = \frac{W_{\mathrm{R}}}{W_{\mathrm{G}}+W_{\mathrm{R}}}$ is the solid fraction. The relationship between the critical impalement pressure and the micro-scale structures was plotted by Bartolo et al. [33]. For surfaces with a roughness gradient, both the touch-down pressure ($P^{\mathrm{T}}_{\mathrm{imp}}$) and sliding pressure ($P^{\mathrm{S}}_{\mathrm{imp}}$) are not constant because of the nonuniform groove width W_{G}. For instance, P^{S}_{imp} varies between 912.5 and 414.8 Pa, which correspond to minimum and maximum groove spacings of 160 and 352 μm, and $P^{\mathrm{T}}_{\mathrm{imp}}$ ranges from approximately 273.9 to 106.9 Pa, respectively, with a groove depth ratio α of 3.6. The above equations also show that a larger D_{G} results in a higher critical impalement pressure and somewhat enhances the robustness against a liquid impalement for the surviving Cassie state [24].

Figure 4.9 shows the effect of the groove depth (D_{G}) on the droplet rebound direction (shown by the contact line position along the x-axis). As shown in Fig. 4.9(a), for small We, the droplet wets the surface in the transition state at 2.2 ms and rebounds following the roughness gradient for a larger α of 3.6, whereas the partial Wenzel state and rebounding in the opposite direction occur for a small α of 2.4. The smaller α

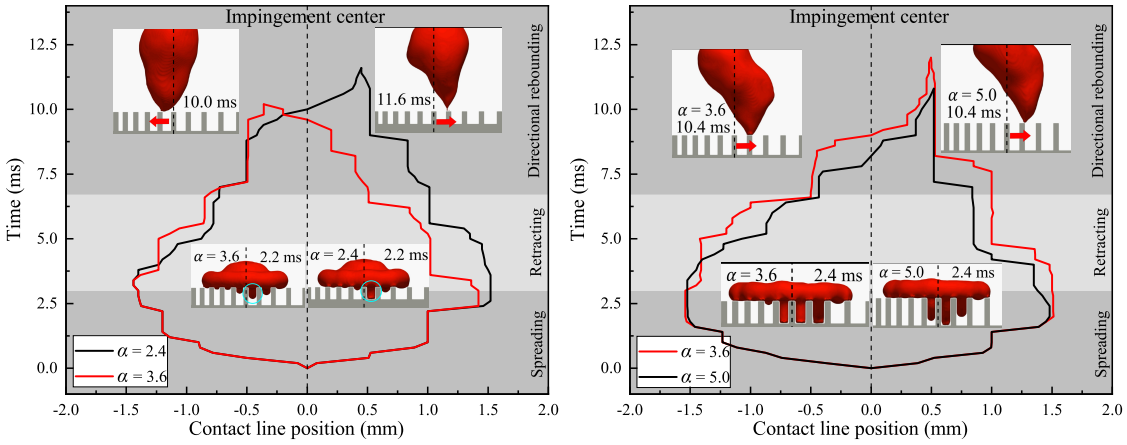

(a) We =10 (b) We =20

Figure 4.9: Groove depth effect on the droplet wetting state and the rebound direction for γ= 1.8 and different groove depth ratios (α), shown by the contact line position along the x-axis: (a) droplet impinging with We=10; (b) droplet impinging with We=20.

lowers the critical impalement pressure, min ($P^{\mathrm{T}}_{\mathrm{imp}}$, $P^{\mathrm{S}}_{\mathrm{imp}}$); thus, the droplet wets the grooves completely, thus leading to a different rebound direction. However, for a larger We, as shown in Fig. 4.9(b), although increasing α from 3.6 to 5.0 increases the critical impalement pressure, both droplets rebound against the roughness gradient owing to the presence of the partial Wenzel state at 2.4 ms. In addition, the contact time for α = 3.6, where more parts of the droplet are in a Wenzel state at 2.4 ms, is larger than that for a larger α. Therefore, for a high We, the liquid penetrates the groove owing to a larger P_{WH} even with a larger α, and forms a partial Wenzel state on the right side of the impingement center, causing the droplet to rebound against the roughness gradient.

4.3.3 Effect of groove width

The capillary pressure (P_C), which is related to the groove width, plays a vital role in the antiwetting and emptying of the liquid within the grooves. The comparison in Fig. 4.10 illustrates the effect of the groove width on the droplet rebound direction. For a

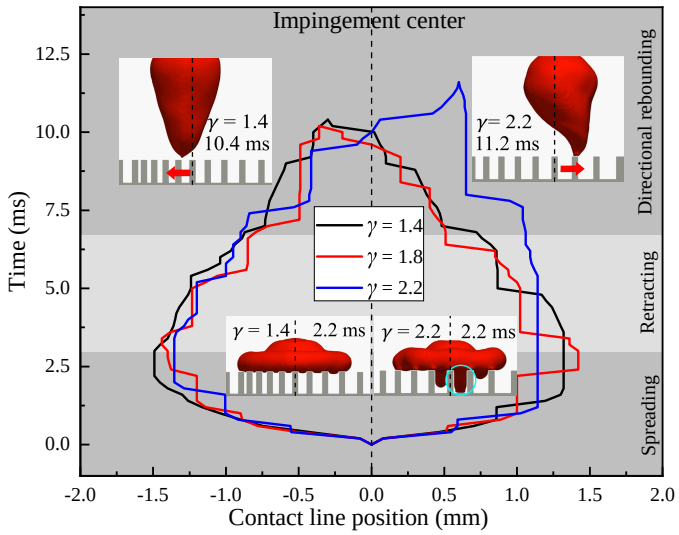

Figure 4.10: Groove width effect on the droplet wetting state and the rebound direction for γ ranging between 1.4 and 2.2, We = 10, and α = 3.6, as shown by the contact line position along the x-axis.

small groove width ratio γ of 1.4, the perfect Cassie state appears at 2.2 ms, whereas the transition state (see Fig. 4.4) and the partial Wenzel state are observed for γ = 1.8 and γ = 2.2, respectively. According to the equation of P_{C}, a larger W_{G} results in a smaller capillary pressure, and the partial Wenzel state is more easily obtained. Therefore, droplets rebound following the roughness gradient for γ = 1.4 and γ = 1.8, whereas the opposite behavior is observed for a larger γ. In addition, the contact time at γ = 2.2 is larger than that for a small groove width owing to the combined effects of the Wenzel state and the smaller capillary pressure.

Because the surface roughness influences the apparent contact angle of droplets on

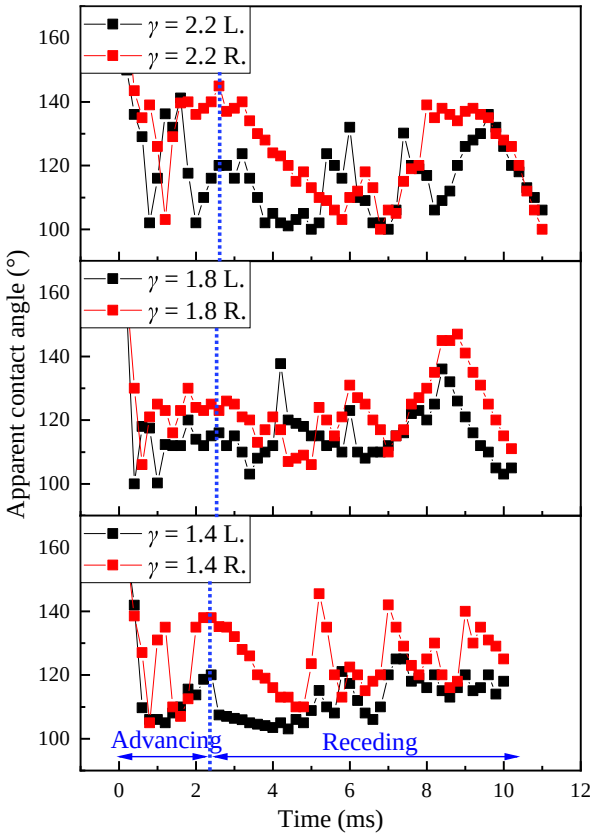

Figure 4.11: Time evolution of apparent contact angle in the left (L.) and right (R.) sides for a droplet impinging on surfaces with γ varying between 1.4 and 2.2, We = 10, and α = 3.6. The dotted lines roughly divide the advancing and receding stages of the droplets.

solid surfaces [18, 19], the roughness gradient in this work leads to an unbalanced Young's force in the lateral direction. The time evolution of the apparent contact angle under different values of γ is shown in Fig. 4.11, which is measured using the geometric method from the drop-images generated from the simulations results, applying image processing software (ImageJ software [34]). From 0 to approximately 2.5 ms, the droplet heads to the wall and spreads. The advancing contact angle increases slightly. A clear decreasing behavior of the receding contact angle can then be observed from 2.5 to approximately 6.0 ms, which happens at the so-called retracting stage [32]. Finally, the receding contact angle decreases again at the rebound stage after approximately 9 ms. Although the apparent contact angle quickly jumps up and down owing to the varying fraction of the droplet−wall and droplet−air interfaces, the value on the right-hand side (R.) is often larger than that on the left-hand side (L.). Hence, the unbalanced Young's force points toward the left-hand side, driving the droplet to move following the roughness gradient for cases with a small γ at 1.4 and 1.8. In contrast, a larger value of $\gamma = 2.2$ results in rebounding in the opposite direction.

4.3.4 Phase diagram

The above results demonstrate that the Weber number (We), the groove width (W_{G}), and the groove depth (D_{G}) play vital roles in determining the rebound direction of droplets dominated by the unbalanced Young's force and the wetting state. The wetting state is based on the relationship among the dynamic pressure (P_{D}), the capillary pressure (P_{C}), and the effective water hammer pressure (P_{WH}) in Fig. 4.3. Here, the combined effects of We and a groove width ratio of γ on the droplet rebound directions are summarized in Fig. 4.12 with a constant of α= 3.6. The figure shows that a droplet with a small impingement velocity (corresponding to $P_{\mathrm{C}} > P_{\mathrm{WH}} > P_{\mathrm{D}}$ in Fig. 4.3) reaching a rough surface with dense ridge arrays (blue region with blue triangles) tends to rebound following the roughness gradient, the reason for which is the unbalanced Young's force in a Cassie state or a transition state owing to the small P_{WH} and larger P_{C}. By contrast, for larger We (corresponding to $P_{\mathrm{WH}} > P_{\mathrm{D}} > P_{\mathrm{C}}$) and sparse

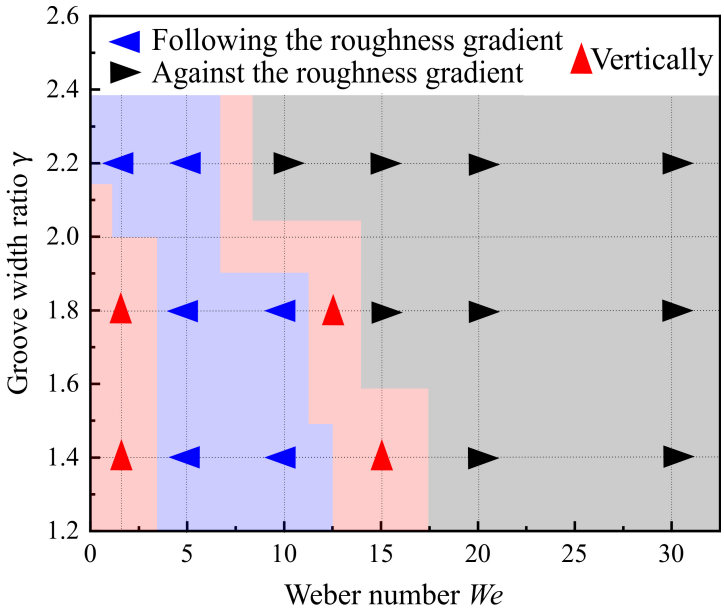

Figure 4.12: Phase diagram of the rebound directions as a function of groove width ratio (γ) and Weber number (We), where α is fixed at 3.6.

surface roughness (gray region with black triangles), the rebound directions are opposed because of the combined effects of the unbalanced Young's force and the wetting state. The third behavior, a vertical bouncing of the droplet (pink region with red triangles), can be obtained at an extremely small We or a critical We. Therefore, We and γ are two important factors that determine P_{WH}, P_{C}, P_{D}, the wetting state, and the rebound direction when droplets impinge on surfaces with a roughness gradient.

From the above results, droplets in a Wenzel state are arrested by the roughness structure and fail to move further. Hence, the hydrophobicity of textured surfaces is weakened. In addition, it is generally agreed that droplets in a Cassie state are characterized as rapid rebounding or rolling off the surface. Therefore, approaches to prevent the wetting transition from a Cassie state to a Wenzel state should be proposed, which are subjects for following studies.

4.4 Conclusions

On surfaces with a roughness gradient, the effects of the Weber number (We), the groove depth (D_{G}), and the groove width (W_{G}) on the droplet transport directions were explored using CLSVOF/DNS. The main results of this exploration are summarized as follows.

1. Three types of rebound behaviors (vertical rebound, following, or against the roughness gradient) are observed when droplets impinge on a surface with a roughness gradient. The rebound behavior depends strongly on We, D_{G}, and W_{G}.

2. For an extremely small We, the small difference in contact angles on the left and right sides of the impingement center results in a vertical rebounding of the droplet. When We increases, the water hammer pressure increases, and the droplet rebounds following the roughness gradient owing to the unbalanced Young's force in a Cassie state. However, rebounding in the opposite direction is observed for a larger We due to the coexistence of the Cassie and Wenzel states.

3. The groove depth determines the critical impalement pressure and robustness against a liquid penetration. A larger groove depth and small We result in rebounding following the roughness gradient, whereas the droplet tends to rebound against the roughness gradient for a small groove depth and larger We due to an achievement of the partial Wenzel state.

4. A droplet impingement at a large groove width, that is, a small antiwetting pressure, tends to generate both Cassie and Wenzel states, resulting in rebounding against the roughness gradient.

References

[1] Y. Liu, G. Whyman, E. Bormashenko, C. Hao, and Z. Wang. Controlling drop bouncing using surfaces with gradient features. *Appl. Phys. Lett.*, 107(5):051604, 2015.

[2] I. U. Chowdhury, P. Sinha Mahapatra, and A. K. Sen. Self-driven droplet transport: Effect of wettability gradient and confinement. *Phys. Fluids*, 31(4):042111, 2019.

[3] V. Narayanamurthy, Z. Jeroish, K. Bhuvaneshwari, P. Bayat, R. Premkumar, F. Samsuri, and M. M. Yusoff. Advances in passively driven microfluidics and lab-on-chip devices: A comprehensive literature review and patent analysis. *RSC Advances*, 10(20):11652–11680, 2020.

[4] X. Dai, N. Sun, S. O. Nielsen, B. B. Stogin, J. Wang, S. Yang, and T.-S. Wong. Hydrophilic directional slippery rough surfaces for water harvesting. *Sci. Adv.*, 4(3):eaaq0919, 2018.

[5] C. Qi, H. Chen, L. Shen, X. Li, Q. Fu, Y. Zhang, Y. Sun, and Y. Liu. Superhydrophobic Surface Based on Assembly of Nanoparticles for Application in Anti-Icing under Ultralow Temperature. *ACS Appl. Nano Mater.*, 3(2):2047–2057, 2020.

[6] F. Geyer, M. D'Acunzi, A. Sharifi-Aghili, A. Saal, N. Gao, A. Kaltbeitzel, T.-F. Sloot, R. Berger, H.-J. Butt, and D. Vollmer. When and how self-cleaning of superhydrophobic surfaces works. *Sci. Adv.*, 6(3):eaaw9727, 2020.

[7] C. Liu, J. Sun, J. Li, C. Xiang, L. Che, Z. Wang, and X. Zhou. Long-range spontaneous droplet self-propulsion on wettability gradient surfaces. *Sci. Rep.*, 7(1):1–8, 2017.

[8] J. Seo, S.-K. Lee, J. Lee, J. S. Lee, H. Kwon, S.-W. Cho, J.-H. Ahn, and T. Lee. Path-programmable water droplet manipulations on an adhesion controlled superhydrophobic surface. *Sci. Rep.*, 5(1):1–10, 2015.

[9] S. Deng, W. Shang, S. Feng, S. Zhu, Y. Xing, D. Li, Y. Hou, and Y. Zheng. Controlled droplet transport to target on a high adhesion surface with multi-gradients. *Sci. Rep.*, 7(1):1–8, 2017.

[10] J. Jeevahan, M. Chandrasekaran, G. B. Joseph, R. Durairaj, and G. Mageshwaran. Superhydrophobic surfaces: A review on fundamentals, applications, and challenges. *J. Coat. Technol. Res.*, 15(2):231–250, 2018.

[11] K. Ellinas, A. Tserepi, and E. Gogolides. Durable superhydrophobic and superamphiphobic polymeric surfaces and their applications: A review. *Adv. Colloid Interface Sci.*, 250:132–157, 2017.

[12] L. R. Scarratt, U. Steiner, and C. Neto. A review on the mechanical and thermodynamic robustness of superhydrophobic surfaces. *Adv. Colloid Interface Sci.*, 246:133–152, 2017.

[13] G. Fang, W. Li, X. Wang, and G. Qiao. Droplet motion on designed microtextured superhydrophobic surfaces with tunable wettability. *Langmuir*, 24(20):11651–11660, 2008.

[14] A. Shastry, M. J. Case, and K. F. Böhringer. Directing droplets using microstructured surfaces. *Langmuir*, 22(14):6161–6167, 2006.

[15] J.-T. Yang, J. C. Chen, K.-J. Huang, and J. A. Yeh. Droplet manipulation on a hydrophobic textured surface with roughened patterns. *J. Microelectromech. Syst.*, 15(3):697–707, 2006.

[16] H. Wu, K. Zhu, B. Cao, Z. Zhang, B. Wu, L. Liang, G. Chai, and A. Liu. Smart design of wettability-patterned gradients on substrate-independent coated surfaces to control unidirectional spreading of droplets. *Soft Matter*, 13(16):2995–3002, 2017.

[17] J. Wu, R. Ma, Z. Wang, and S. Yao. Do droplets always move following the wettability gradient? *Appl. Phys. Lett.*, 98(20):204104, 2011.

[18] R. N. Wenzel. Resistance of solid surfaces to wetting by water. *Ind. Eng. Chem.*, 28(8):988–994, 1936.

[19] A. Cassie and S. Baxter. Wettability of porous surfaces. *Trans. Faraday Soc.*, 40:546–551, 1944.

[20] M. Reyssat, F. Pardo, and D. Quéré. Drops onto gradients of texture. *Europhys. Lett.*, 87(3):36003, 2009.

[21] B. A. Malouin Jr, N. A. Koratkar, A. H. Hirsa, and Z. Wang. Directed rebounding of droplets by microscale surface roughness gradients. *Appl. Phys. Lett.*, 96(23):234103, 2010.

[22] J. Song, M. Gao, C. Zhao, Y. Lu, L. Huang, X. Liu, C. J. Carmalt, X. Deng, and I. P. Parkin. Large-area fabrication of droplet pancake bouncing surface and control of bouncing state. *ACS Nano*, 11(9):9259–9267, 2017.

[23] C. Liu, H. Zhan, J. Yu, R. Liu, Q. Zhang, Y. Liu, and X. Li. Design of superhydrophobic pillars with robustness. *Surf. Coat. Technol.*, 361:342–348, 2019.

[24] J. Zhao and S. Chen. Following or against topographic wettability gradient: Movements of droplets on a micropatterned surface. *Langmuir*, 33(21):5328–5335, 2017.

[25] Y. Wang, M. Jian, and X. Zhang. Lateral motion of a droplet after impacting on groove-patterned superhydrophobic surfaces. *Colloid Surf. A-Physicochem. Eng. Asp.*, 570:48–54, 2019.

[26] B. Zhang, Q. Lei, Z. Wang, and X. Zhang. Droplets can rebound toward both directions on textured surfaces with a wettability gradient. *Langmuir*, 32(1):346–351, 2016.

[27] T. Bobinski, G. Sobieraj, M. Psarski, G. Celichowski, and J. Rokicki. Droplet bouncing on the surface with micro-structure. *Arch. Mech*, 69:177–193, 2017.

[28] F. Brochard. Motions of droplets on solid surfaces induced by chemical or thermal gradients. *langmuir*, 5(2):432–438, 1989.

[29] M. Gross, F. Varnik, and D. Raabe. Fall and rise of small droplets on rough hydrophobic substrates. *EPL (Europhys. Lett.)*, 88(2):26002, 2009.

[30] D. Hee Kwon and S. Joon Lee. Impact and wetting behaviors of impinging micro-droplets on superhydrophobic textured surfaces. *Appl. Phys. Lett.*, 100(17):171601, 2012.

[31] A. U. Siddique, M. Trimble, F. Zhao, M. M. Weislogel, and H. Tan. Jet ejection following drop impact on micropillared hydrophilic substrates. *Phys. Rev. Fluids*, 5(6):063606, 2020.

[32] D. Vadillo, A. Soucemarianadin, C. Delattre, and D. Roux. Dynamic contact angle effects onto the maximum drop impact spreading on solid surfaces. *Phys. Fluids*, 21(12):122002, 2009.

[33] D. Bartolo, F. Bouamrirene, E. Verneuil, A. Buguin, P. Silberzan, and S. Moulinet. Bouncing or sticky droplets: Impalement transitions on superhydrophobic micropatterned surfaces. *Europhys. Lett.*, 74(2):299, 2006.

[34] W. S. Rasband et al. ImageJ, 1997.

Nomenclature

C	: VOF function [-]	α	: Groove depth ratio [-]
C_{s}	: Speed of sound in water [-]	γ	: Groove width ratio [-]
D_0	: Initial droplet diameter [m]	Δ	: Mesh size [-]
D_{G}	: Groove depth [m]	θ_{a}	: Advancing contact angle [$^\circ$]
f_{s}	: Solid fraction [-]	θ_{Y}	: Intrinsic contact angle [$^\circ$]
F_{Y}	: Young's force [N]	ρ	: Density [kg/m^3]
$\boldsymbol{g}$	: Gravitational acceleration [m/s^2]	μ	: Viscosity [mPa $\cdot$ s]
k	: Water hammer pressure coefficient [-]	σ	: Surface tension coefficient [N/m]
$\boldsymbol{L}_z$	: Angular momentum [kg$\cdot m^3$/s]	**Subscripts**	
m	: Mass [kg]	a	: Air
n	: Natural number [-]	l	: Liquid
$\boldsymbol{P}$	: Translational momentum [kg$\cdot$m/s]	R	: Right side
P_{C}	: Capillary pressure [Pa]	L	: Left side
P_{D}	: Dynamic pressure [Pa]	max	: Maximum
$P_{\mathrm{imp}}^{\mathrm{S}}$	: Sliding pressure [Pa]	min	: Minimum
$P_{\mathrm{imp}}^{\mathrm{T}}$	: Touch-down pressure [Pa]		
P_{WH}	: Water hammer pressure [Pa]		
$\boldsymbol{r}$	: Position vector [m]		
u_0	: Initial velocity [m/s]		
We	: Weber number [-]		
W_{G}	: Groove width [m]		
W_{R}	: Ridge width [m]		

Chapter 5

Suppressing the Cassie-to-Wenzel transition using surfaces with hierarchical structures

5.1 Introduction

As described in Chapters 3 and 4, a larger groove width leads to a greater surface hydrophobicity, which is suppressed with a further increase in the groove width because a Wenzel state is obtained. It is generally agreed upon that the wetting in a Wenzel state weakens the hydrophobicity of a textured surface, and a stable Cassie state is preferred in practical applications. To both enhance the surface hydrophobicity and suppress the Cassie-to-Wenzel state transition, in this chapter, a novel hydrophobic surface with primary structures (taller) to improve the hydrophobicity and secondary structures (shorter) to stabilize the Cassie state, is proposed.

Hydrophobic surfaces are designed to prevent the sticking, icing, and corrosion of water droplets on the surface of industrial equipment. One widely used strategy is to texture the surface by pillars or grooves [1, 2]. On low-energy surfaces, the Cassie model [3] demonstrates that the contact angle (θ_C) is amplified by minimizing the solid fraction (f_s), $\cos\theta_C = f_s(1+\cos\theta_Y)-1$, where θ_Y is the Young's angle (the intrinsic contact angle)

of a droplet on the ideal surface. However, if f_s decreases to zero, it will result in a fragile surface structure or a fully wet Wenzel state [4]. In general, droplets in a Cassie state are characterized as a large apparent contact angle (θ_{app}) and small roll-off angle, revealing behaviors such as a rapid rebounding off and rolling off of textured surfaces. Wetting transition from a Cassie state to a Wenzel state induced by impingement or vibration [5], however, causes the liquid to be arrested by the rough structures and fail to move further, thereby weakening the water-repellency of a hydrophobic surface [6].

The wetting transition typically results from two scenarios: a depinning mechanism and a sag mechanism [7, 8]. Because the sag mechanism is irrelevant if the designed structures prevent the sagging liquid−air interface from touching the bottom of the substrate, a number of studies have concerned the effect of roughness structures on the energy barrier of the depinning mechanism. Inspired by the lotus leaf (see Chapter 1), artificial surfaces with a hierarchical roughness exhibit a metastable Cassie state of droplets owing to the multi-level energy barrier for the Cassie-to-Wenzel transition [6, 9–12]. Nosonovsky [6] theoretically demonstrated that multiscale roughness can help resist the destabilization, thus preventing the liquid penetration even in the case with hydrophilic materials. Pan et al. [12] experimentally demonstrated that the critical Laplace pressure needed for losing the Cassie state increases due to the increase in hierarchical level and structural complexity. Nosonovsky further [13] discussed the effect of the re-entrant surface topography on the wetting state, which was beyond the standard Wenzel and Cassie models. Whyman and Bormashenko [14, 15] analyzed various surfaces with re-entrant topographies from the viewpoint of the stability of a Cassie state by considering the tension of the three-phase contact line (TPCL). They found that the potential barrier, separating the Cassie and Wenzel states, sufficiently increased as the liquid penetrated into the structures. Inspired by the body skin of Springtails or Collembola (wingless arthropods), Hensel et al. [16] analytically and numerically indicated that a robust wetting resistance even for low-surface-tension liquids (such as hexane) can be obtained on surfaces with T-shaped profiles, paving the way for fabricating omniphobic surfaces with a high repellency irrespective of a solid surface chemistry. Furthermore, they [17]

proposed a theoretical model to predict the barrier of the wetting transition. Other approaches, such as masking surfaces with non-communicating holes [18, 19] and mushroom pillars [20], have also proven to be effective; however, the need to explore alternate methods becomes imperative when considering the fabrication processes, fabrication over large areas [21], and the robustness and durability of such tiny structures [22]. To both maximize the surface hydrophobicity and stabilize the Cassie state, we propose a novel surface with sparse and taller primary structures (small f_s) to repel water, and shorter secondary structures to suppress the Cassie-to-Wenzel wetting transition, which can be a one-step fabrication surface through laser processing [23, 24] based on a simple and regular structures.

In this chapter, we therefore conduct a computational study on the effect of secondary structures on the droplet deformation, penetration, and wetting state on the novel surface. We first describe a study on the wetting behavior of droplets on surfaces with various secondary structures. We further extend our analysis to different impingement centers. Furthermore, we focus on the influence of the Weber number (We); i.e., $We = \rho_l D_0 u_0^2/\sigma$, where D_0 is the droplet diameter, u_0 is the initial impinging velocity, and σ is the surface tension coefficient of the water$-$air interface ($\sigma = 72.8 \times 10^{-3}\mathrm{Nm}^{-1}$). The two-step wetting transition of droplets on the novel surface is theoretically discussed based on the Laplace's law, the Young's equation, and the Gibbs extension. Finally, some concluding remarks are provided.

5.2 Problem statement

A schematic of the computational domain is shown in Fig. 6.1(a). All 3D simulations are conducted on a staggered Cartesian grid consisting of 320×300×320 grid points (a total of 30.72 million grid points) in the x-, y- and z- directions, respectively, and the grid size Δ is equal to 32 μm in all three directions. A spherical water droplet with diameter D_0=62Δ is placed above the center of the substrate. The distance between the wall and droplet center is set as $0.55D_0$ to make the droplet evolve in a physical manner before touching the solid. A textured surface with primary and secondary ridges is located at the bottom, and the ridge width, the groove width, and the ridge height of the primary and secondary structures are W_{R1} and W_{R2} , W_{G1} and W_{G2}, and H_{R1} and H_{R2} as shown in the cross-sectional view in Fig. 6.1(b), respectively. According to the results in Chapter 3, the perfect Wenzel state was obtained at a groove width ratio of $\gamma \geq 2.0$. Hence, the redefined γ=$W_{\mathrm{G1}}/W_{\mathrm{R1}}$ is fixed at 15Δ/7Δ, whereas the secondary ridges are placed in the middle of the primary grooves and thus the secondary

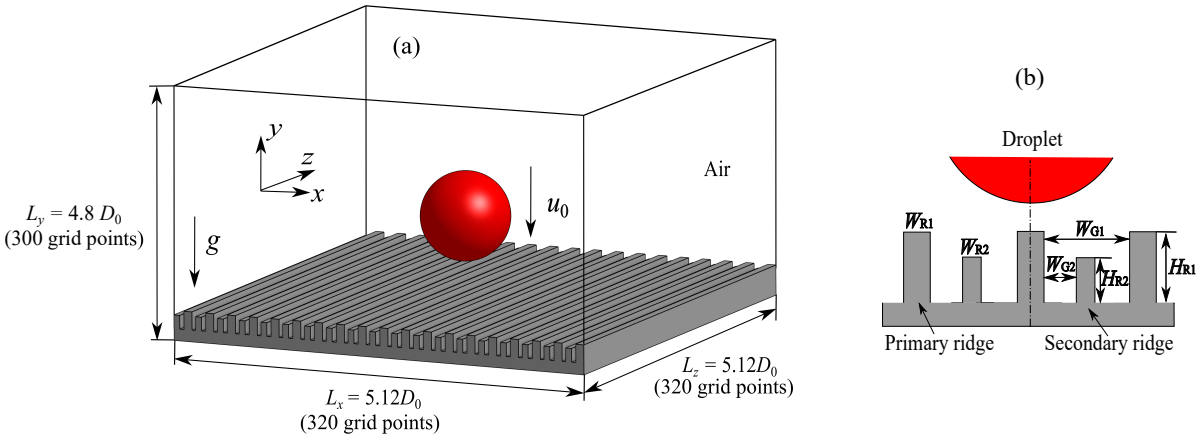

Figure 5.1: Schematic of the computational domain and conditions: (a) computational domain; (b) cross-sectional view of the structure, where the black dashed-dotted line in (b) represents the impingement center.

Table 5.1: Parameters used in numerical simulations.

Parameter	Symbol	Value
Mesh size	Δ	32μm
Droplet diameter	D_0	62Δ
Intrinsic contact angle	θ_{Y}	100°
Primary ridge width	W_{R1}	7Δ
Primary groove width	W_{G1}	15Δ
Primary groove width ratio	γ	15/7
Secondary ridge width	W_{R2}	5Δ
Primary ridge height	H_{R1}	18Δ
Secondary ridge height ratio	H^*	0.0, 2/9, 0.5, 7/9, 1.0
Weber number	We	1–30
Impinging velocity	u_0	0.19–1.04 m/s

groove width is $W_{\mathrm{G2}} = (W_{\mathrm{G1}} - W_{\mathrm{R2}})/2$. In addition, the ratio of the secondary ridge height $H^* = H_{\mathrm{R2}}/H_{\mathrm{R1}}$ ranges from 0.0 to 1.0 to investigate the influence of the relevant height on the droplet wetting state. The detailed simulation parameters are shown in Table 6.2. The liquid and air phase properties are the same as those in Chapters 3 and 4. The boundary condition of the substrate is set as a wall, whereas the surroundings are considered as shear free surfaces. In addition, a gravitational acceleration $|\boldsymbol{g}|$ of 9.8 m/s^2 is imposed.

5.3 Results and discussion

5.3.1 Effect of secondary structure

The images compared in Fig. 5.2 illustrate the effect of the secondary ridge on the droplet wetting states. We note here that the slight asymmetric behavior of the droplets is caused by a mismatch between the droplet center and the impingement ridge center, whose effect on the wetting, penetrating, and rebounding behavior of droplets is negligible in this study. Roughly, the droplet undergoes the spreading and retracting stages on three types of substrates. At the end of the spreading phase at approximately 3.2ms, the inertia, viscosity, and surface tension compete toward the stop of the contact line [25] and droplets reach their so-called maximum spreading phase. Then, the liquid starts retracting and goes back to the impingement center. For the surface with $H^* = 0.0$, liquid penetration occurs when the liquid breaks through the primary ridge. A part of the liquid quickly penetrates into the grooves, forming a Wenzel state at 2.0 ms because of the downward momentum of the droplet. In contrast, although the first penetration occurs, the secondary penetration, defined as the liquid breaking through the secondary groove, is hindered by secondary ridges in which a stable Cassie state is obtained on the

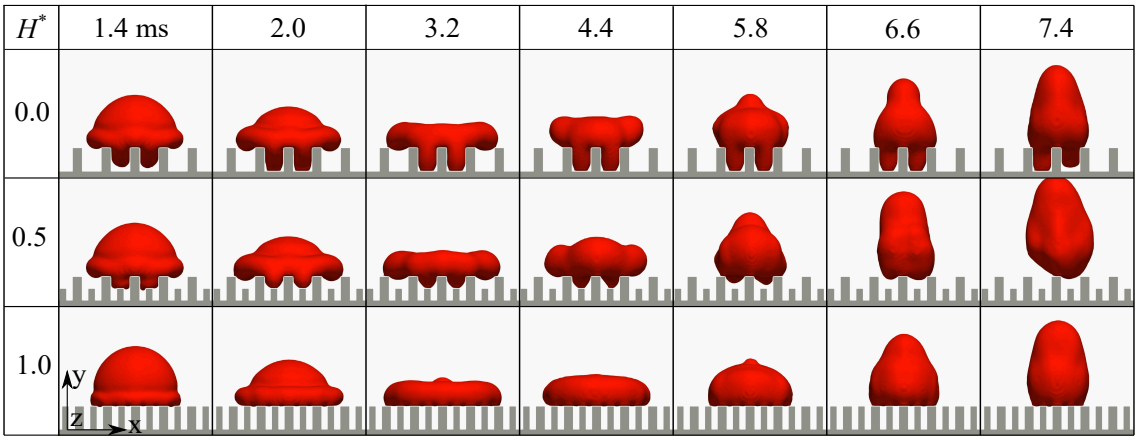

Figure 5.2: Time evolution of impinging water droplet on surfaces with different secondary ridges (H^*=0.0, 0.5, and 1.0, respectively). Here, We and γ are fixed at 10 ($u_0 = 0.6$m/s) and 15/7, respectively.

surfaces with $H^* = 0.5$. The droplet undergoes viscous dissipation and retracts toward the impingement center due to the surface tension. At 5.8 ms, although the impregnated liquid is sustained in the groove for the case of $H^* = 0.0$, the droplet is already detached from the secondary ridge and tends to leave the surface with $H^* = 0.5$. For the droplet impinging on surface with $H^* = 1.0$, although the Wenzel state is not observed, the water repellency of the surface is not greatly improved based on the Cassie model. Therefore, to improve both the hydrophobicity of textured surfaces and the stability of the Cassie state, decorating the surface with secondary structures ($H^* = 0.5$) can be a promising approach for impinging droplets.

To analyze the effect of a secondary ridge on the droplet wetting behavior, we define the spreading factor ($\beta = D/D_0$) and the penetration factor ($\eta = H/H_{\mathrm{R1}}$), where D is the instantaneous diameter of a wetted area along the x-axis, and the maximum spreading factor ($\beta_{\max}$) is obtained when $D = D_{\max}$ at the maximum spreading stage

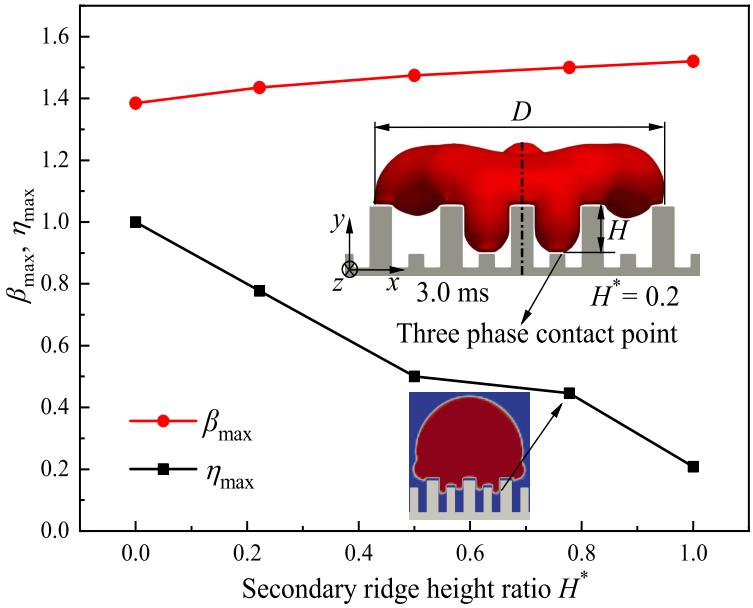

Figure 5.3: Variations of maximum spreading factor ($\beta_{\max}$) and penetration factor ($\eta_{\max}$) of droplets impinging on surfaces with different secondary structures. Here, We and γ are fixed at 10 ($u_0 = 0.6$m/s) and 15/7, respectively. The dashed-dotted line in the snapshots indicates the centerline.

(see the images at 3.2ms in Fig. 5.2). Similarly, H is the instantaneous penetration depth of a liquid estimated by the distance between three-phase contact point (on the cross-sectional view) and the top of primary ridges, and the maximum penetration factor ($\eta_{\max}$) is achieved with $H = H_{\max}$ at the maximum penetration stage (see the images at 2.0ms in Fig. 5.2). The maximum spreading factor ($\beta_{\max}$) and the maximum penetration factor ($\eta_{\max}$) are plotted against the secondary ridge height ratio (H^*) in Fig. 5.3. Here, $H^* = 0.0$ means the surface with only primary ridges, whereas $H^* = 1.0$ represents the heights are same at 576 μm between the primary and secondary ridges. From Fig. 5.3, both $\eta_{\max}$ and $\beta_{\max}$ change nearly linearly with an increase in the secondary ridge height. $\eta_{\max}$ decreases from approximately 1.0 to 0.2 as H^* increases from 0.0 to 1.0. This occurs because the increase in secondary ridge height prevents the liquid from penetrating into small grooves with a spacing of W_{G2}. As for the inflection with $H^* \geq 7/9$, this is because the larger kinetic energy at the early impacting stage triggers the secondary penetration as shown in Fig. 5.3. Here, $\beta_{\max}$ slightly increases from approximately 1.4 to 1.5 as H^* increases from 0.0 to 1.0, suggesting that liquid tends to spread and float on the patterns rather than fall into grooves.

Subsequently, the time scales, as analyzed in Fig. 5.4 are the spreading time (t_s), emptying time (t_e), and contact time (t_c), where t_s is the time at which the droplet spreads and reaches its maximum spreading stage, t_e is the time interval between the moments when the droplet first infiltrates into the primary groove and when the groove is completely emptied, during which the droplet undergoes downward penetrating and upward capillary emptying processes, and t_c is the so-called contact time during which the time period from when the drop first touches the surface to that when it bounces off the surface [27]. As shown in Fig. 5.4, H^* exerts a significant effect on t_e but only a small influence on t_s and t_c.

Specifically, t_s experiences a slight increase with H^* ranging from 0.0 to 1.0. This is because, at a larger H^* (taller secondary ridge), liquid can easily reach and touch the secondary ridge, meaning a decrease in the fraction of liquid$-$air interface, leading to a decrease in the contact angle based on the Cassie model [3]. Shen et al. [28]

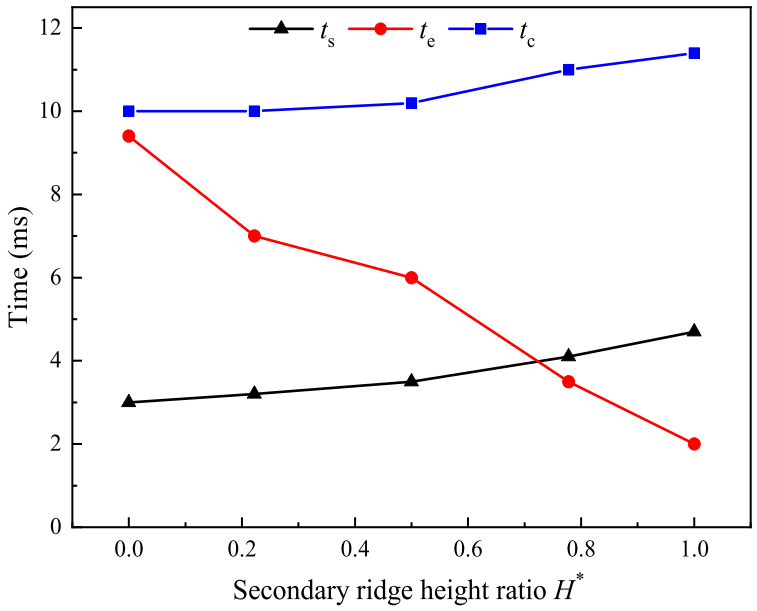

Figure 5.4: Variations of t_s, t_e, and t_c with H^* ranging from 0.0 to 1.0. Here, We and γ are fixed at 10 and 15/7, respectively.

proposed an equation to estimate t_s based on the energy conservation law, but there is something wrong in this equation, because it is not homogeneous to a time according to the dimensionality check. We re-derived this equation, and t_s can be estimated by

$$t_s \sim \frac{2}{3}\sqrt{\frac{D_0}{\rho_l \mu u_0}}\left(\frac{\rho_l D_0^3 u_0^2 + 12\sigma D_0^2 - 3\sigma {D^2}_{\max}(1-\cos(\theta_{app}))}{{D^2}_{\max} u_0^2}\right) \tag{5.1}$$

Here, θ_{app} is the apparent contact angle, which is a function of the Capillary number ($Ca = \mu_l u_0/\sigma$) and the intrinsic contact angle (θ_Y) of surfaces, $\theta_{app} = f(Ca, \theta_Y)$, Re the Reynolds number, $Re = \rho u_0 D_0/\mu_l$. When we combine Eqs. (5.2) [29] and (6.5), a decrease in θ_{app} leads to an increase in t_s.

$$\beta_{\max} = \frac{D_{\max}}{D_0} = \sqrt{\frac{We + 12}{3(1-\cos(\theta_{app})) + 4We/\sqrt{Re}}} \tag{5.2}$$

Figure 5.4 shows that t_e decreases with an increase in H^*, because the increase in this value prevents the liquid penetration into the grooves, as shown in Fig. 5.3. Theoretically, because t_e involves the processes of liquid penetration and capillary emptying [27], when the liquid does not touch the bottom of the surface, the timescale can be expressed

as

$$t_{\mathrm{e}} \sim -\frac{u_0 \rho D_0 (W_{\mathrm{G}} + W_{\mathrm{R}})}{2\sigma \cos\theta_{\mathrm{Y}}} \tag{5.3}$$

where W_{G} and W_{R} are the width of the wetted groove and the ridge, respectively. The interval of the roughness structure W_{G}+W_{R} = W_{G1} + W_{R1} when only the first penetration occurs, whereas it equals W_{G2}+W_{R2} under the secondary penetration. Based on Eq.(5.2), the increase in H^*, meaning a decrease in W_{G} and W_{R}, leading to a decline of t_{e}.

$$t_{\mathrm{r}} \propto \sqrt{\frac{\rho_l D_0^3}{2\sigma\pi \left[1 - \cos\left(\theta_{\mathrm{app}}\right)\right]}} \tag{5.4}$$

For the contact time ($t_{\mathrm{c}} \approx t_{\mathrm{s}} + t_{\mathrm{r}}$), on a specific uniform surface, t_{c} is not dependent on the impact velocity u_0 but is a function of D_0, ρ, and σ [30]. However, the increase in H^* in this study brings about an increase in the solid fraction (f_{s}) and thus lowers the apparent contact angle. During the retracting stage, liquid in the grooves returns to the mother droplet, and liquid floating on the ridges recoils back to the center. According to Eq. (6.4) for $We \gg 1$ [30], the retracting time t_{r} is related to θ_{app} and D_0 . It can be seen that a decrease in θ_{Y} brings about an increase in t_{r}. Based on Eqs.(6.5)−(6.6), a slight increase in t_{c} is found with H^* ranging from 0.0 to 1.0.

5.3.2 Effect of impingement center

To analyze the influence of the impact position, two cases with different impinging centers are studied. The spreading factor of droplets with an impingement centered at the primary ridge (β_{ridge}) and the primary groove (β_{groove}) are compared in Fig. 5.5. It can be seen that both values increase rapidly up to the peak (β_{max}) and then slowly decreases to zero, which correspond to the spreading (before 2.0 ms) and the recoiling stage (after 4.0 ms) of a droplet−wall interaction, respectively [25]. As the images shown in Fig. 5.5 indicate, the first penetration occurs in three grooves for the droplet with the impinging center at the primary groove, whereas only two primary grooves are filled with liquid for impingement centered at the primary ridge. When the droplet touches the ridge first, it spreads out and the kinetic energy rapidly converts into the surface energy.

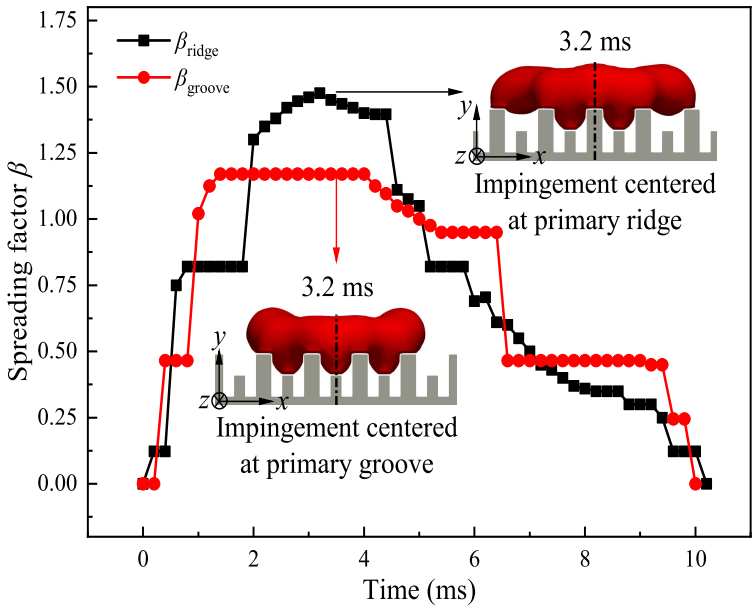

Figure 5.5: Variation of the spreading factor (β) against time. We, H^*, and γ are fixed at 10, 0.5, and 2.1, respectively. The dashed-dotted line in the snapshots indicates the centerline.

When the droplet contacts the groove first, it tends to infiltrate into grooves that limit the spreading behavior. Hence, the maximum β_{groove} is smaller than the maximum β_{ridge}. Then, the surface energy transfers into kinetic energy at the retracting stage, leading to a rebound of the droplet. The contact time of the droplets with the substrate, from first touch to finally leave off, shows no significant difference due to the same surface roughness. The lines in Fig. 5.5 exhibit a staged increase and decrease in behavior, which is induced by the "jump-stick" of three-phase contact line on the rough surfaces, revealing a jump from the current to the following contact pillar [31, 32].

Figure 5.6 shows the penetration depth factor of a droplet with the impingement centered at the primary ridge (η_{ridge}) and primary groove (η_{groove}). It is clear that the maximum η_{ridge} is approximately 0.5, which illustrates that the first penetration occurs but the secondary penetration is prevented well by the secondary ridge. For a droplet heading to the groove, the maximum η_{groove} is approximately 0.6 owing to the occurrence of a secondary penetration. This occurs because of the different conversion

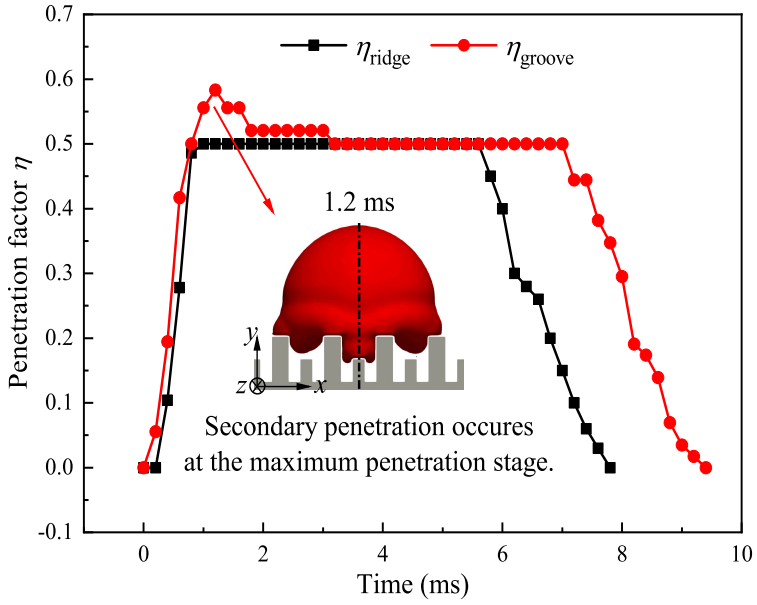

Figure 5.6: Variation of the penetration factor (η) against time. We, H^*, and γ are fixed at 10, 0.5, and 2.1, respectively. The dashed-dotted line in the snapshots indicates the centerline.

of the kinetic energy when the droplets touch the ridge and groove. Furthermore, η_{ridge} starts to decrease at approximately 5.8 ms, whereas the decreasing behavior occurs at 7.2 ms for η_{groove}. In addition, the groove is early emptied with the impingement centered at the primary ridge, which is reduced by approximately 1.5 ms compared to that of the droplet impinging on the primary groove first.

5.3.3 Effect of Weber number

The Weber number (We) characterizes the relative magnitude of the kinetic energy to the surface tension energy. Figure 5.7 plots the maximum droplet penetrating factor η_{max} against We on a surface with ($H^* = 0.5$) and without ($H^* = 0.0$) secondary ridges. On the surface with only primary ridges, η_{max} increases rapidly to its maximum value of 1.0 with We ranging from 1 to 10, because a greater impinging inertia induces a larger deformation of the droplet. Then, $\eta_{\text{max}}+$ remains constant with a further increase in We owing to the Wenzel state. In contrast, η_{max} shows a slow growth behavior on a

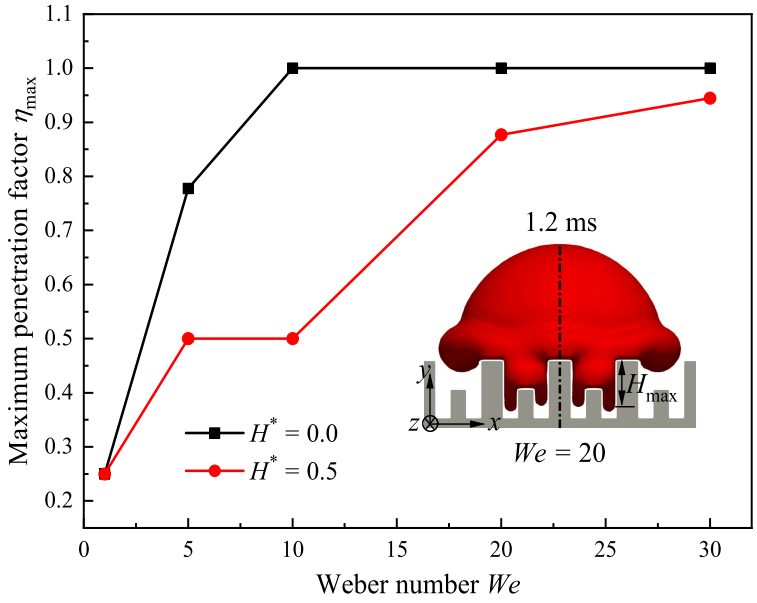

Figure 5.7: Comparison of maximum droplet penetration factor ($\eta_{\max}$) between surfaces without ($H^* = 0.0$) and with ($H^* = 0.5$) secondary ridges.

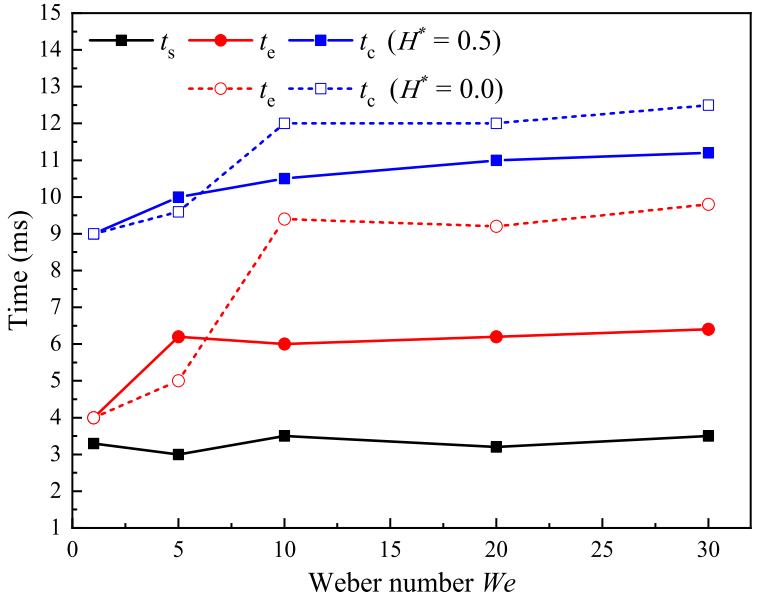

Figure 5.8: We dependence at time scales of t_s, t_e, and t_c. The variations of t_s, t_e, and t_c with $H^* = 0.5$ are plotted by solid lines, whereas the red dash line shows the effect of We on t_e for surfaces without secondary ridges ($H^* = 0.0$).

surface with primary and secondary ridges, and the value is always smaller than 1.0 with We between 1 and 30. In detail, $\eta_{\max}$ increases to 0.5 with We from of 1 to 5, when the droplet touches the secondary ridges. Then $\eta_{\max}$ increases slowly because secondary ridges weaken the penetration of liquid into the secondary grooves. From the image in Fig. 5.7, no liquid touches the bottom of the substrate even under large We conditions with $H^* = 0.5$. We again emphasize here that the secondary ridges prevent the wetting transition.

Next, the effect of We on the time scales of t_{s}, t_{e}, and t_{c} are plotted in Fig. 5.8. First, we compare the emptying time (t_{e}) of droplets impinging on surfaces with (H^* = 0.5) and without (H^* = 0.0) secondary ridges. For $H^* = 0.0$, t_{e} increases rapidly for We smaller than 10, and no significant change can be observed with a continuously increasing We. This is because, at a small We, the maximum penetration factor ($\eta_{\max}$) of the liquid increases rapidly with an increase in We, thus leading to a sharp increase in t_{e}. This tendency is also explained based on Eq. (6.4), from which the increase in We or u_0 brings about an increase in t_{e} on a specific surface. However, a Wenzel state is obtained in which t_{e} almost remains constant with We between 10 and 30. On the surface with $H^* = 0.5$, t_{e} quickly increases to approximately 6.2 ms with We ranging from 1 to 5 owing to the abrupt change in the surface roughness. Then, t_{e} undergoes no significant change with We between 5 and 30, during which secondary ridges prevent the droplet from completely wetting the pattern structure. Interestingly, with We=5, t_{e} for a case in which $H^* = 0.5$ is larger than that with $H^* = 0.0$. This is because, at a small We, the liquid dose not touches the bottom of the grooves on the surface with $H^* = 0.0$, whereas the liquid touches the secondary ridges on the surface with H^* = 0.5. For the contact time on the surface with $H^* = 0.0$, t_{c} increases rapidly with We ranging from 1 to 10, and it undergoes small change with further increasing We due to the achievement of a Wenzel state. When $H^* = 0.5$, t_{c} experiences small increase with We from 1 to 5 owing to the abrupt change in the surface roughness, and no significant variation can be found with We from 10 to 30. Furthermore, on a specific surface with $H^* = 0.5$, t_{s} is almost constant with the increase in We.

5.3.4 Theoretical analysis

The above penetration of an expanding droplet into the groove can be analytically investigated based on the pressure. For a sagging liquid surface, the theoretical model of the transition barrier is derived based on the correlation of Laplace's law, Young's equation, and Gibbs extension [16, 17, 33, 34]. Laplace's law describes the relationship among the pressure difference (ΔP), the surface tension coefficient (σ), and the interface radius:

$$\Delta P = \sigma \left(\frac{1}{R_{\parallel}} + \frac{1}{R_{\perp}} \right) \tag{5.5}$$

where $R_{\parallel}$ and $R_{\perp}$ are the radii of the semi-cylinder interface in the groove parallel and perpendicular directions. For the primary and secondary ridge textured surfaces shown in Fig. 5.9, we suppose that $R_{\parallel}$=∞ and $R_{\perp}$=$R_{\min}$, where $R_{\min}$ is estimated as

$$R_{\min} = \frac{d}{\sin\left(\theta_{\mathrm{app}} - \pi\right)} \tag{5.6}$$

Here d represents the distance between the three-phase contact point at the edge and the symmetry center of the sagging interface on the cross-section. In addition, d_1 and d_2 in Fig. 5.9 are for liquid wetting of the primary and secondary ridges, when $d_1 = W_{\mathrm{G1}}$ and $d_2 = W_{\mathrm{G2}}$, respectively.

For an ideally flat surface with intrinsic contact angle θ_{Y}, Young's equation describes the force balance acting on the TPCL:

$$\sigma_{\mathrm{sa}} = \sigma_{\mathrm{sl}} + \sigma \cos\theta_{\mathrm{Y}} \tag{5.7}$$

where σ_{sa} and σ_{sl} are the surface tension coefficient of solid−air and solid−liquid, respectively. The inhibition of liquid penetration by a sharp edge was described well by the Gibbs inequality condition [16, 17]:

$$\theta_{\mathrm{Y}} \leq \theta_{\mathrm{app}} \leq \theta_{\mathrm{Y}} + (\pi + \Psi) \tag{5.8}$$

where θ_{app} is the apparent contact angle at a given position, and Ψ is the geometrical edge angle ($\Psi = \pi/2$ in our system), i.e., Ψ_1 and Ψ_2 in Fig. 5.9 are the geometrical edge angles for the primary and secondary ridges, respectively.

Differing from the stationary droplet in previous articles [16, 17, 34, 35], an impinging droplet is studied in this study. Both the hydrodynamic and hydrostatic pressures should be considered when calculating the pressure difference. Given that the ΔP between the total pressure (P_t) inside the liquid phase and the atmospheric pressure (P_0) can be calculated by

$$\Delta P = P_\mathrm{t} - P_0 = \frac{\sigma \sin\left(\theta_\mathrm{app} - \pi\right)}{d} \tag{5.9}$$

For the pressure triggering the penetration of the liquid, if $\theta_\mathrm{Y} \leq \Psi + \pi/2$, the canthotaxis effect dominates the penetration [36]. Hence, based on Eqs.(5.5)−(5.9), the critical pressure (breakthrough pressure) can be estimated by

$$P_\mathrm{b} = \frac{\sigma \sin\left(\theta_\mathrm{Y} - \Psi\right)}{d} \tag{5.10}$$

If $\theta_\mathrm{Y} > \Psi + \pi/2$, a Laplace breakup occurs [36]. The breakthrough pressure is determined by the Laplace law with $R = d$:

$$P_\mathrm{b} = \frac{\sigma}{d} \tag{5.11}$$

Penetration occurs when the pressure difference exceeds the breakthrough pressure ($\Delta P > P_\mathrm{b}$). According to the topographic structure and intrinsic contact angle in this study, the canthotaxis effect takes place first due to $\theta_\mathrm{Y} \leq \Psi + \pi/2$. Both Eqs. (5.10) and (5.11) illustrate that P_b increases with a decrease in$d$. Therefore, on surfaces with primary and secondary structures, a two-step wetting transition is induced by the canthotaxis effect, as shown in Fig. 5.9. In addition, $P_{\mathrm{b},1}$ and $P_{\mathrm{b},2}$ in Fig. 5.9 are the breakthrough pressures for the first and second penetration, respectively. In the initial situation shown in Fig. 5.9(a), liquid is considered to float on the ridges, and the total pressure P_t inside the liquid phase equals the atmospheric pressure P_0 ($P_{\mathrm{t},0}$ = P_0) when a perfect Cassie state is obtained. The liquid−air interface will sag into the groove (without penetration) if P_t increases. A further increase in P_t results in the first penetration scenario in Fig. 5.9(b), when the pressure difference exceeds the first breakthrough pressure ($\Delta P > P_{\mathrm{b},1}$), resulting in a downward sliding of the TPCL along the groove sidewall (red arrows). The secondary penetration, however, is hindered by

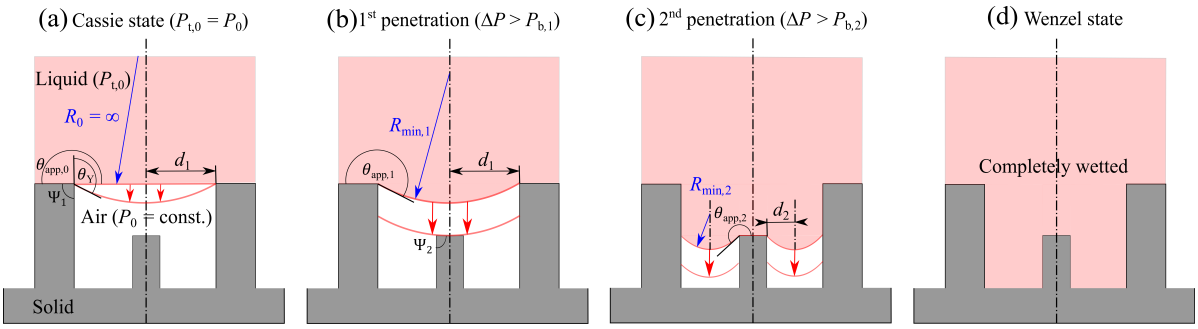

Figure 5.9: Schematic (sectional view) of the liquid penetration mechanisms of an impinging droplet: (a) Perfect Cassie state with $P_{t,0} = P_0$, curvature radius R_0, apparent contact angle $\theta_{app,0}$ and the edge angle of primary ridge Ψ_1; (b) First penetration takes place when $\Delta P > P_{b,1}$ with curvature radius $R_{min,1}$, apparent contact angle $\theta_{app,1}$ and the edge angle of secondary ridge Ψ_2; (c) Second penetration happens when $\Delta P > P_{b,2}$ with apparent contact angle $\theta_{app,2}$, curvature radius $R_{min,2}$; (d) Wenzel state: liquid completely wets the grooves. The dash-dotted line in the snapshots indicates the centerline.

secondary ridges owing to a smaller d_2, which leads to a higher breakthrough pressure $P_{b,2}$ in Fig. 5.9(c). For this reason, the secondary ridge in this work can prevent the wetting transition from the Cassie to the Wenzel state. The secondary penetration takes places when $\Delta P > P_{b,2}$. Finally, the Wenzel state is obtained when the grooves are completely wetted, as shown in Fig. 5.9(d).

Figure 5.10 plots the relation between the breakthrough pressures (P_b) and the groove width ratio (γ), considering the significant effect of the groove width on the wetting transition of droplets impinging on a textured surface. It can be seen that P_b decreases sharply with the increase in γ, because a large value of γ corresponds to a larger d, leading to a small P_b according to Eq. (5.10). A penetration, may not occur even if ΔP slightly exceeds P_b, and the penetration can be triggered with P_b within a certain range [17].

To quantitatively judge the effect of the initial impacting conditions on the occurrence of a wetting transition, we define P_t as the total pressure in the liquid, which is the sum of the hydrodynamic pressure (P_{hd}), hydrostatic pressure (P_{hs}), and atmospheric pressure

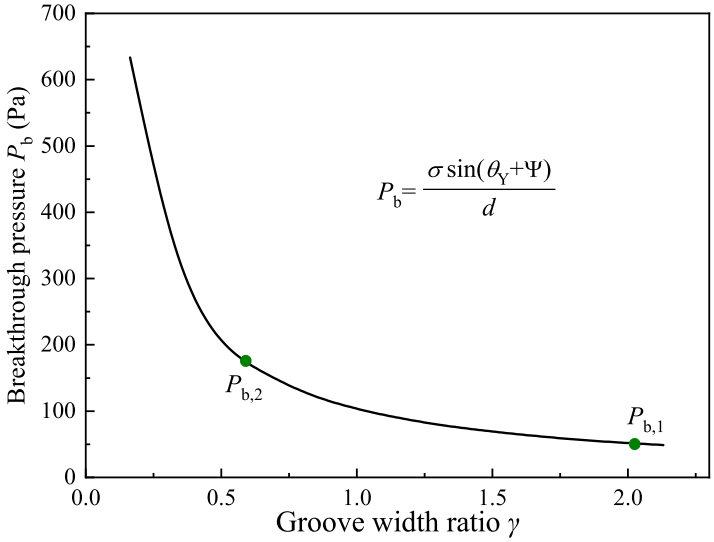

Figure 5.10: Variation in the breakthrough pressure (P_b) against the groove width ratio (γ). P_b is estimated using Eq. (5.10). The green points represent the breakthrough pressures at the primary ($P_{\mathrm{b},1}$) and secondary ($P_{\mathrm{b},2}$) roughness , when d equals $W_{\mathrm{G}1}$ and $W_{\mathrm{G}2}$, respectively.

(P_0) based on Bernoulli's equation. Thus, according to Eq. (5.9), ΔP can be rewritten as

$$\Delta P = P_\mathrm{hd} + P_\mathrm{hs} = \frac{1}{2}\rho {u_0}^2 + \rho g h \tag{5.12}$$

Here, h is the thickness of the fluid, which we assume equals D_0 initially. Although $\Delta P > P_{\mathrm{b},2}$ is satisfied when We=10, the secondary penetration is not observed according to the images in Fig. 5.2. Two reasons induce this behavior. One is the conversion from kinetic energy to surface tension energy during the droplet spreading stage. As the other reason, the critical We value has a certain range, only within which the wetting transition can be triggered as mentioned above [17].

The phase diagram of the wetting transition based on the simulation results is shown in Fig. 5.11. To compare the simulation results with a theoretical estimation, ΔP estimated using Eq. (5.12) and P_b estimated using Eq. (5.10) are presented. It can be seen that the region of no penetration, the first penetration, and the secondary penetration is obtained with an increase in We, which is roughly divided by the theoretically esti-

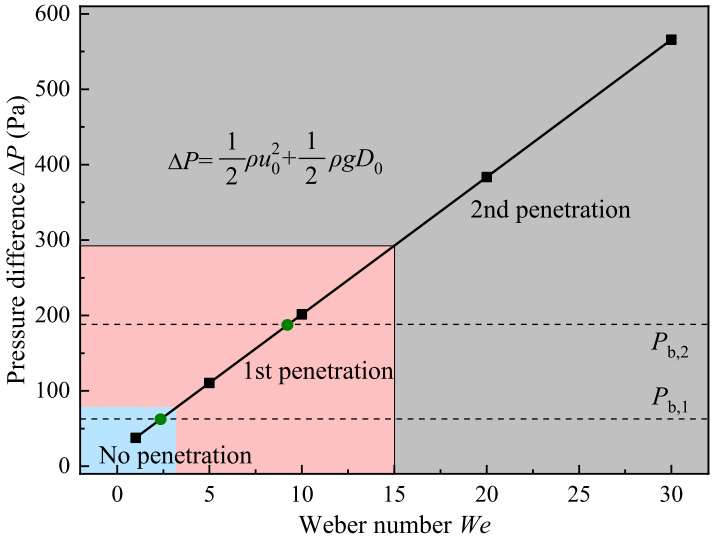

Figure 5.11: Phase diagram of the liquid penetration based on the simulation results, and the variation of in pressure difference (ΔP) against We of between 1 and 30, and H^*=0.5. The black dashed lines represent the value of the breakthrough pressure at the primary ($P_{b,1}$) and secondary ($P_{b,2}$) structures when d equals d_1=W_{G1}=15Δ and d_2=W_{G2}=5Δ, respectively. The blue, red, and gray regions represent the area, in which no penetration, the first penetration, and the secondary penetration take place based on our numerical results.

mated $P_{b,1}$ and $P_{b,1}$. We here again suggest that a secondary penetration is not triggered even though the initial ΔP exceeds $P_{b,2}$ with We=10. At a large We, the secondary penetration in Fig. 5.7 occurs when We = 20.

Inspired by the above penetration theory of droplets impinging on surfaces with primary and secondary ridges, a fractal-structured surface is conceived in Fig.5.12. It is predicted that the surface with multi-level structures can ensure a more stable Cassie wetting than that in Fig. 5.9, because the fractal surface is demonstrated to be super-water-repellent with a contact angle of as large as 174° [37]. Fractal models were developed by Onda et al. [37] and more recently by Jain et al. [38] to predict the apparent contact angle on surfaces with multi-level structures. Therefore, this study provides a new fabrication strategy of robust hydrophobic or superhydrophobic surfaces with a

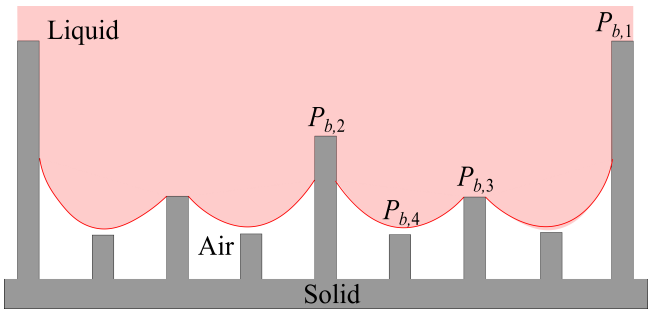

Figure 5.12: A fractal surface characterized by four-level ridges. The liquid penetration can be prevented well by a multi-level structure, corresponding to a breaking through pressures of $P_{\mathrm{b},1}$, $P_{\mathrm{b},2}$, $P_{\mathrm{b},3}$, and $P_{\mathrm{b},4}$.

stable Cassie state, which can be extended to a large-scale generation of superhydrophobic surfaces with simple, regular, and micro-scale structures. Future studies should pay closer attention to the fractal surface and Cassie-to-Wenzel transition of impinging droplets on textured surfaces.

5.4 Conclusions

To amplify the surface hydrophobicity as much as possible and simultaneously enhance the stability of the Cassie state on the textured surfaces, a novel surface decorated with primary and secondary structures was proposed and examined numerically. The results obtained in this chapter are summarized as follows.

1. When compared with the droplet behavior on surfaces masked with only primary structures, the secondary penetration is suppressed such that a stable Cassie state is obtained on surfaces with both primary and secondary ridges.

2. The liquid penetration factor and the emptying time decrease with an increase in the secondary ridge height. The impingement position, at the primary groove or the primary ridge, also plays a vital role in the wetting transition.

3. The increase in the Weber number (We), meaning a larger kinetic energy, leads to the occurrence of a secondary penetration. The value of We also influences the time scales owing to the abrupt change in the solid fraction when a liquid slides down the sidewall of the primary groove and then touches the secondary ridge.

4. The two-step wetting transition found in the numerical results is explained well by theoretical models based on the correlation of Laplace's law, Young's equation, and Gibbs extension.

5. This study provides developing guidelines of superhydrophobic surfaces when considering the stability of a Cassie state, one-step fabrication processes, and fabrication over large areas.

References

[1] D. Quéré. Rough ideas on wetting. *Physica A*, 313(1-2):32–46, 2002.

[2] D. Quéré. Wetting and roughness. *Annu. Rev. Mater. Res.*, 38:71–99, 2008.

[3] A. Cassie and S. Baxter. Wettability of porous surfaces. *Trans. Faraday Soc.*, 40:546–551, 1944.

[4] R. N. Wenzel. Resistance of solid surfaces to wetting by water. *Ind. Eng. Chem.*, 28(8):988–994, 1936.

[5] E. Bormashenko, R. Pogreb, G. Whyman, Y. Bormashenko, and M. Erlich. Vibration-induced Cassie-Wenzel wetting transition on rough surfaces. *Appl. Phys. Lett.*, 90(20):201917, 2007.

[6] M. Nosonovsky. Multiscale roughness and stability of superhydrophobic biomimetic interfaces. *Langmuir*, 23(6):3157–3161, 2007.

[7] D. Bartolo, F. Bouamrirene, E. Verneuil, A. Buguin, P. Silberzan, and S. Moulinet. Bouncing or sticky droplets: Impalement transitions on superhydrophobic micropatterned surfaces. *Europhys. Lett.*, 74(2):299, 2006.

[8] M. Reyssat, F. Pardo, and D. Quéré. Drops onto gradients of texture. *Europhys. Lett.*, 87(3):36003, 2009.

[9] K. Koch, B. Bhushan, Y. C. Jung, and W. Barthlott. Fabrication of artificial Lotus leaves and significance of hierarchical structure for superhydrophobicity and low adhesion. *Soft Matter*, 5(7):1386–1393, 2009.

[10] M. S. Bell, A. Shahraz, K. A. Fichthorn, and A. Borhan. Effects of hierarchical surface roughness on droplet contact angle. *Langmuir*, 31(24):6752–6762, 2015.

[11] Z. Lian, J. Xu, W. Ren, Z. Wang, and H. Yu. Bouncing dynamics of impact droplets on the biomimetic plane and convex superhydrophobic surfaces with dual-level and three-level structures. *Nanomaterials*, 9(11):1524, 2019.

[12] R. Pan, M. Cai, W. Liu, X. Luo, C. Chen, H. Zhang, and M. Zhong. Extremely high Cassie–Baxter state stability of superhydrophobic surfaces via precisely tunable dual-scale and triple-scale micro–nano structures. *J. Mater. Chem. A*, 7(30):18050–18062, 2019.

[13] M. Nosonovsky and B. Bhushan. Why re-entrant surface topography is needed for robust oleophobicity. *Phil. Trans. R. Soc. A*, 374(2073):20160185, 2016.

[14] G. Whyman and E. Bormashenko. How to make the Cassie wetting state stable? *Langmuir*, 27(13):8171–8176, 2011.

[15] E. Bormashenko and G. Whyman. On the role of the line tension in the stability of Cassie wetting. *Langmuir*, 29(18):5515–5519, 2013.

[16] R. Hensel, R. Helbig, S. Aland, H.-G. Braun, A. Voigt, C. Neinhuis, and C. Werner. Wetting resistance at its topographical limit: The benefit of mushroom and serif T structures. *Langmuir*, 29(4):1100–1112, 2013.

[17] R. Hensel, A. Finn, R. Helbig, S. Killge, H.-G. Braun, and C. Werner. In situ experiments to reveal the role of surface feature sidewalls in the Cassie–Wenzel transition. *Langmuir*, 30(50):15162–15170, 2014.

[18] V. Bahadur and S. V. Garimella. Preventing the Cassie-Wenzel transition using surfaces with noncommunicating roughness elements. *Langmuir*, 25(8):4815–4820, 2009.

[19] H. Mayama, T. Nishino, A. Sekiguchi, R. Nishimura, K. Uchida, S. Yokojima, S. Nakamura, and Y. Nonomura. Theoretical consideration of wetting in Cassie-Baxter state on multi-pillar and multi-hole surfaces: Thermodynamics and Laplace pressure. *J. Photopolym. Sci. Technol.*, 32(2):279–285, 2019.

[20] R. Roy, J. A. Weibel, and S. V. Garimella. Re-entrant cavities enhance resilience to the Cassie-to-Wenzel state transition on superhydrophobic surfaces during electrowetting. *Langmuir*, 34(43):12787–12793, 2018.

[21] J. Song, M. Gao, C. Zhao, Y. Lu, L. Huang, X. Liu, C. J. Carmalt, X. Deng, and I. P. Parkin. Large-area fabrication of droplet pancake bouncing surface and control of bouncing state. *ACS Nano*, 11(9):9259–9267, 2017.

[22] D. Wang, Q. Sun, M. J. Hokkanen, C. Zhang, F.-Y. Lin, Q. Liu, S.-P. Zhu, T. Zhou, Q. Chang, B. He, et al. Design of robust superhydrophobic surfaces. *Nature*, 582(7810):55–59, 2020.

[23] J. Li, S. Zhao, F. Du, Y. Zhou, and H. Yu. One-step fabrication of superhydrophobic surfaces with different adhesion via laser processing. *J. Alloys Compd.*, 739:489–498, 2018.

[24] H. Wang, M. He, H. Liu, and Y. Guan. One-step fabrication of robust superhydrophobic steel surfaces with mechanical durability, thermal stability, and anti-icing function. *ACS Appl. Mater. Interfaces*, 11(28):25586–25594, 2019.

[25] D. Vadillo, A. Soucemarianadin, C. Delattre, and D. Roux. Dynamic contact angle effects onto the maximum drop impact spreading on solid surfaces. *Phys. Fluids*, 21(12):122002, 2009.

[26] J. Wu, R. Ma, Z. Wang, and S. Yao. Do droplets always move following the wettability gradient? *Appl. Phys. Lett.*, 98(20):204104, 2011.

[27] C. Guo, D. Zhao, Y. Sun, M. Wang, and Y. Liu. Droplet impact on anisotropic superhydrophobic surfaces. *Langmuir*, 34(11):3533–3540, 2018.

[28] Y. Shen, J. Tao, H. Tao, S. Chen, L. Pan, and T. Wang. Approaching the theoretical contact time of a bouncing droplet on the rational macrostructured superhydrophobic surfaces. *Appl. Phys. Lett.*, 107(11):111604, 2015.

[29] M. Pasandideh-Fard, Y. Qiao, S. Chandra, and J. Mostaghimi. Capillary effects during droplet impact on a solid surface. *Phys. Fluids*, 8(3):650–659, 1996.

[30] D. Richard, C. Clanet, and D. Quéré. Contact time of a bouncing drop. *Nature*, 417(6891):811–811, 2002.

[31] L. Xu, Z. Li, and S. Yao. Directional motion of evaporating droplets on gradient surfaces. *Appl. Phys. Lett.*, 101(6):064101, 2012.

[32] R. Zheng, H. Liu, J. Sun, and Y. Ba. Droplet hysteresis investigation on non-wetting striped textured surfaces: A lattice Boltzmann study. *Physica A*, 411:53–62, 2014.

[33] T. M. Schutzius, G. Graeber, M. Elsharkawy, J. Oreluk, and C. M. Megaridis. Morphing and vectoring impacting droplets by means of wettability-engineered surfaces. *Sci. Rep.*, 4:7029, 2014.

[34] J. Oliver, C. Huh, and S. Mason. Resistance to spreading of liquids by sharp edges. *J. Colloid Interface Sci.*, 59(3):568–581, 1977.

[35] C. Extrand and S. I. Moon. Influence of geometry, edges and roughness on liquid penetration and removal during wet cleaning. *ECS J. Solid State Sci. Technol.*, 3(6):P198, 2014.

[36] J. Berthier, F. Loe-Mie, V.-M. Tran, S. Schoumacker, F. Mittler, G. Marchand, and N. Sarrut. On the pinning of interfaces on micropillar edges. *J. Colloid Interface Sci.*, 338(1):296–303, 2009.

[37] T. Onda, S. Shibuichi, N. Satoh, and K. Tsujii. Super-water-repellent fractal surfaces. *Langmuir*, 12(9):2125–2127, 1996.

[38] R. Jain and R. Pitchumani. Fractal model for wettability of rough surfaces. *Langmuir*, 33(28):7181–7190, 2017.

Nomenclature

D	: Instantaneous droplet diameter [m]	β	: Spreading factor [-]
d	: Distance of contact points [m]	γ	: Primary groove width ratio [-]
D_0	: Initial droplet diameter [m]	Δ	: Mesh size [-]
f_s	: Solid fraction [-]	η	: Penetration factor [-]
$\boldsymbol{g}$	: Gravitational acceleration [m/s^2]	θ_app	: Apparent contact angle [°]
H	: Instantaneous penetration depth [m]	θ_Y	: Intrinsic contact angle [°]
H_R	: Ridge height [m]	μ	: Viscosity [mPa · s]
H^*	: Secondary right height ratio [-]	ρ	: Density [kg/m^3]
h	: Thickness of the liquid [m]	σ	: Apparent contact angle [°]
P_0	: Ambient pressure [Pa]	Ψ	: Intrinsic contact angle [°]
P_b	: Breakthrough pressure [Pa]	**Subscripts**	
P_hd	: Hydrodynamic pressure [Pa]	1	: Primary
P_hs	: Hydrostatic pressure [Pa]	2	: Secondary
P_t	: Total pressure [Pa]	a	: Air
ΔP	: Pressure difference [Pa]	l	: Liquid
R	: Interface radius [m]	s	: Solid
Re	: Reynolds number [-]	max	: Maximum
t	: Time [s]	min	: Minimum
t_c	: Contact time [s]	$\parallel$	: Parallel direction of groove
t_e	: Emptying time [s]	$\perp$	: Perpendicular direction of groove
t_r	: Receding time [s]		
t_s	: Spreading time [s]		
u_0	: Initial velocity [m/s]		
We	: Weber number [-]		
W_G	: Groove width [m]		
W_R	: Ridge width [m]		

Chapter 6

Stabilizing the Cassie state using surfaces with multiple holes

6.1 Introduction

In Chapter 5, a novel surface is proposed to suppress the Cassie-to-Wenzel transition. However, liquid penetration occurs inevitably at large Weber number (We) conditions. In this chapter, we study the wetting stability of a droplet impinging on surfaces with multiple holes, where a robust air pocket is formed during the droplet-wall interaction.

Hydrophobic surfaces can be fabricated by introducing micro-scale structures [1, 2]. Common structures are pillars [3–5], grooves [6, 7], and holes [8, 9]. For instance, Liu et al. [5] reported a robust superhydrophobic surface manufactured by masking with a regular array of square pillars on a substrate of 304 stainless steel (intrinsic contact angle θ_{Y}=88°). On this textured surface, the equilibrium contact angle and the roll-off angle of a water droplet are ∼162.5° and ∼2.3°, respectively. Guo et al. [6] proposed a groove textured surface, upon which the contact time between an impingement droplet and the surface was reduced by ∼70%. These above textured surfaces, however, are subject to the wetting transition from a Cassie state to a Wenzel state (the surface is fully wetted) [10] induced by impingement or vibration [11]. It is generally agreed that the wetting in the Wenzel state weakens the hydrophobicity of a textured surface, and

a stable Cassie state is preferred in practical applications. Hence, how to enhance the stability of the Cassie state on textured surfaces has aroused extensive research interest.

Inspired by natural superhydrophobic surfaces (such as the lotus leaf and insect wing in Chapter 1), artificial surfaces with a hierarchical multiscale roughness exhibit a metastable Cassie state because of the multi-level energy barrier for the Cassie-to-Wenzel transition [12–16]. Nosonovsky [12] theoretically suggested the stability of the liquid−air interface on surfaces with hierarchical roughness. Pan et al. [16] experimentally demonstrated that the critical pressure needed for eliminating the Cassie state increased due to the increase in the hierarchical level and structural complexity. However, these tiny dual- and triple-scale structures are vulnerable to mechanical damage, leading to a loss of superhydrophobicity. Other approaches, such as re-entrant structures and T-shaped structures, have also been proved effective in enhancing the stability of the Cassie state [17–23]. This is because, on these surfaces, the energy barrier separating the Cassie and Wenzel states increases due to the increase in liquid-air interface when liquid penetrates into the re-entrant structures [19]. For example, Nosonovsky and Bhushan [18] proposed that the re-entrant surface topography is crucial for the resistance to wetting by liquids, because it is capable of pinning the liquid−air interface. Using T-shaped structures, Wang et al. [22] obtained superhydrophobic ($\theta_Y > 150°$) behaviors of droplets after they masked a hydrophilic substrate with T-shaped micropillars coated with diamond-like carbon. Hensel et al. [23] also found that a robust wetting resistance even for low-surface-tension liquids (such as hexane) was achieved on surfaces with mushroom and T-shaped structures. However, these re-entrant and T-shaped structures are facing challenges in manufacturing owing to the complex profiles. In addition, the Wenzel state is obtained at larger impingement velocities due to the air escaping from the structural space.

Multi-hole [8] or noncommunicating structures [9], by contrast, have paved a way to fabricate surfaces with a super stable Cassie state because of the robust air pockets in holes or pores. Bahadur et al. [9] used electrowetting to control the droplet morphology and wetting states on rough surfaces, and they found that surfaces with noncommuni-

cating roughness structures (holes) required significantly higher voltages to trigger the Cassie-to-Wenzel transition than corresponding surfaces with communicating roughness elements (pillars). Mayama et al. [8] theoretically predicted that a multi-hole surface easily generates a higher Laplace pressure than a multi-pillar surface making it easy to prevent liquid penetration. Various researchers [24–26] also proved the stability of the Cassie state by comparing the dynamics of the liquid−air interface when surfaces with holes and pillars are submerged in water. For an impinging droplet, however, it remains elusive how and to what extent the surface with multiple holes can modulate the wetting stability, which is the scope of this chapter.

To capture the physics behind the wetting on multi-hole surfaces, a three-dimensional direct numerical simulation (DNS) is employed, which is based on the coupled level-set and volume of fluid (CLSVOF) method [27–29]. The wetting behavior of droplets on surfaces with multi-hole and multi-pillar structures are first compared. A pressure analysis conducted to show the fundamental reason of the wetting behavior is subsequently shown. To test the stability of the wetting state, we further extend our analysis to larger impingement velocities. A theoretical model to predict the maximum spreading factor of an impinging droplet is presented. Finally, some concluding remarks are given.

6.2 Problem statement

Two textured substrates are modelled: a multi-pillar surface (MPS) shown in Fig. 6.1(a) and another multi-hole surface (MHS) shown in Fig. 6.1(b). The front views of the MPS and the MHS are shown in Figs. 6.1(c) and 6.1(d), respectively. We use the same symbols in the MPS and MHS for the surface structure parameters, i.e., h, the pillar height or hole depth; a, the side length of square pillars or hole space; and b, the pillar or hole intervals, respectively.

For the Cassie wetting state on a textured surface [30], the contact angle θ_{C} of a droplet is defined by

$$\cos\theta_{\mathrm{C}} = f_{\mathrm{s}}\cos\theta_{\mathrm{s}} + f_a\cos\theta_a \tag{6.1}$$

where f_{s} and f_a are the area fraction the solid and air occupy in the apparent wetting

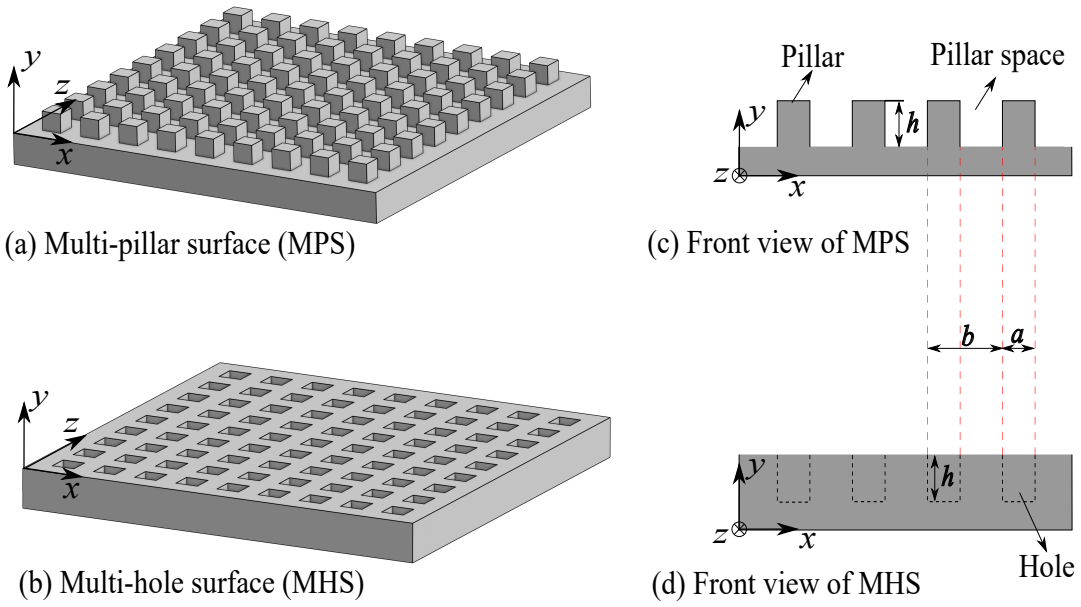

Figure 6.1: Schematic of surfaces characterized by multiple pillars and the multiple holes: (a) 3-D model of multi-pillar surface (MPS) masked by square pillars; (b) 3-D model of multi-hole surface (MHS) masked by square holes; (c) front view of the MPS with pillar height h, the side length of square pillars a, and the pillar interval b; (d) front view of the MHS with hole depth h, the side length of square holes a, and the hole interval b.

area, θ_s and θ_a are the equilibrium contact angle of a droplet sitting on a solid and in air, respectively, $\theta_s = \theta_Y$, $\theta_a = \pi$, and $f_s + f_a = 1$. In this chapter, f_s and f_a for the MPS and MHS can be described by

$$f_s^{MPS} = f_a^{MHS} = \frac{a^2}{b^2} \tag{6.2}$$

$$f_a^{MPS} = f_s^{MHS} = 1 - \frac{a^2}{b^2} \tag{6.3}$$

Theoretical study on the Laplace pressure of surfaces with cylindrical pillars or holes was proposed by Mayama et al. [8]. Prior to the numerical simulation, we first compare the difference between the MPS and MHS on f_s, f_a, and pressures against a/b. Figure 6.2(a) plots the dependences of f_s and f_a on a/b based on Eq. (6.2) and Eq. (6.3). It is clear that $f_s = f_a$ is obtained when a/b is equal to the critical value of $\sqrt{2}/2$.

Table 6.1: Structures studied in this chapter

Structure	a	b	a/b	f_s^{MPS}	f_a^{MPS}	f_s^{MHS}	f_a^{MHS}
S-MPS/MHS	5Δ	20Δ	0.25	0.0625	0.9375	0.9375	0.0625
M-MPS/MHS	10Δ	20Δ	0.50	0.25	0.75	0.75	0.25
C-MPS/MHS	14Δ	20Δ	0.70	0.49	0.51	0.51	0.49
L-MPS/MHS	16Δ	20Δ	0.80	0.64	0.46	0.46	0.64

Table 6.2: Parameters for numerical simulations.

Parameter	Symbol	Value
Initial droplet diameter	D_0	62Δ
Intrinsic contact angle	θ_Y (°)	100
Initial pressure	P_0 (kPa)	100
Hole depth or pillar height	h	18Δ
Weber number	We	10
Initial velocity	u_0	0.603

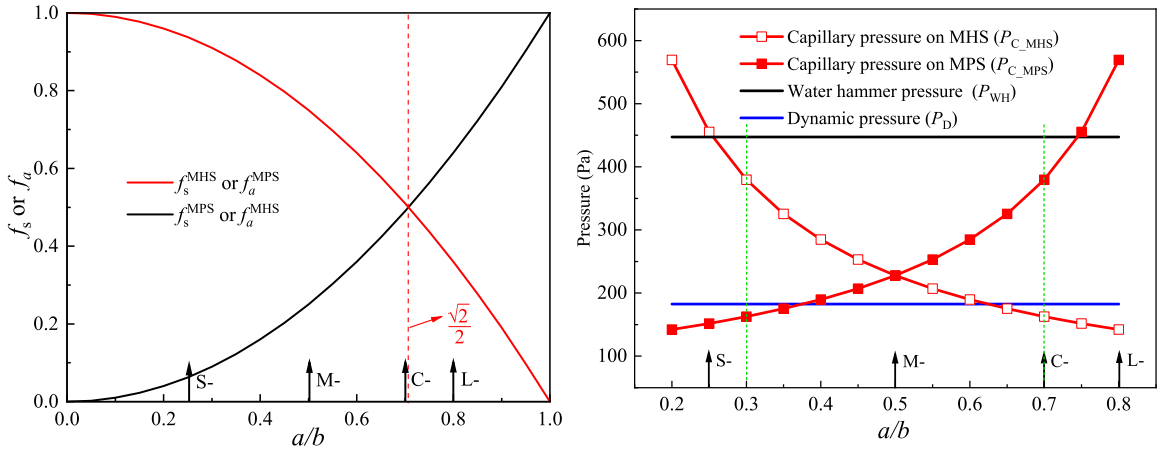

(a) Dependences of f_s and f_a on a/b based on Eqs. (6.2) and (6.3).

(b) P_D, P_C, and P_{WH} against a/b with We=10 (u_0 = 0.603m/s).

Figure 6.2: Effect of a/b on f_s, f_a, and pressures: (a) dependences of f_s and f_a on a/b, and $f_s = f_a$ is obtained at the critical $a/b = \sqrt{2}/2$; (b) variation of P_D, P_C, and P_{WH} against a/b, and three regions are roughly divided by green dashed lines. Black arrows point out the cases studied in this chapter.

In addition, the wetting state of an impinging droplet on a textured surface [31, 32] depends on the combined effects of the dynamic pressure (wetting pressure), $P_D = \rho_l u_0^2/2$, the capillary effect (antiwetting pressure), $P_C = -2\sigma\cos\theta_a/W_s$, and the effective water hammer pressure, $P_{WH} = k\rho_l C_s u_0$, where ρ_l is the water density, u_0 is the initial velocity, θ_a is the advancing contact angle predicted every time step by apparent contact angle model (see Chapter 2), which is as large as 120° in this chapter, W_s the width of the pillar space or the hole, and thus $W_s = b - a$ on the MPS and $W_s = a$ on the MHS, k represents the water hammer pressure coefficient, which is fixed at 5×10^{-4} owing to the large structural interval and the small u_0 [33], and C_s is the speed of sound in water, i.e., C_s = 1480 m/s. Figure 6.2(b) shows the effects of a/b on the three pressures of P_D, P_C, and P_{WH}, where We is the Weber number, i.e., $We = \rho_l D_0 u_0^2/\sigma$, in which D_0 is the initial droplet diameter, and σ is the surface tension coefficient of the water−air interface ($\sigma = 72.8 \times 10^{-3}\mathrm{Nm}^{-1}$). With the increase in a/b, P_D and P_{WH} are constant, but P_{C_MHS} decreases and P_{C_MPS} increases because of the change of W_s. In general,

the Cassie state, the transition state (partially impaled state [31, 32]), and the Wenzel state are obtained with $P_{\mathrm{C}} > P_{\mathrm{WH}} > P_{\mathrm{D}}$, $P_{\mathrm{WH}} > P_{\mathrm{C}} > P_{\mathrm{D}}$, and $P_{\mathrm{WH}} > P_{\mathrm{D}} > P_{\mathrm{C}}$, respectively. Based on the comparison of P_{D}, P_{C}, and P_{WH} in Fig. 6.2(b), we expect to observe the corresponding wetting state of an impinging droplet in these three regions (roughly classified by the green dashed lines in Fig. 6.2(b)). Eight cases with different structures (a/b = 0.25, 0.50, 0.70, and 0.80 for both the MPS and MHS) are studied. The details of these cases are shown in Table 6.1. Other parameters utilized in the simulation are shown in Table 6.2.

All cases are conducted on a uniform staggered grid consisting of 320×300×320 grid points (a total of 30.72 million grid points with grid size Δ=32 μm) in the x-, y- and z-directions, respectively. In the computational domain with initial pressure P_0, a spherical water droplet with diameter D_0 heads to the center of the substrate with initial impingement velocity u_0. Other parameters such as the water viscosity (μ_l), air density (ρ_a) and viscosity (μ_a) are the same as those in Chapter 2. In this chapter, liquid is assumed incompressible, but air is a compressible fluid, obeying the ideal gas law: PV = constant. In addition, an isothermal simulation is conducted. The boundary condition of the substrate is set as a wall, whereas the surroundings are considered as shear free surfaces. A gravitational acceleration $|\boldsymbol{g}|$ of 9.8 m/s^2 is imposed

6.3 Results and discussion

First, the wetting state of an impinging droplet on the MPS and the MHS is investigated by comparing snapshots, the maximum penetration depth, and the contact time. Subsequently, the reason for the penetration and sagging of the liquid into structures is explored from the viewpoint of pressure. In addition, the stable non-wetting feature of the MHS is demonstrated under an extremely larger Weber number (We). Finally, a new prediction model for the maximum spreading factor is constructed based on the law of energy conservation.

6.3.1 Wetting state

Rioboo et al. [34] classified the evolution into four phases: a kinematic phase, spreading phase, relaxation phase (or recoiling phase), and wetting or equilibrium phase when a droplet impinges on a flat substrate. On a textured surface, liquid penetration occurs simultaneously during the spreading phase, and emptying of the liquid from the structural space is also seen during the recoiling phase. To better illustrate the wetting state of a droplet, both the front view and bird's-eye view of a droplet at 1.8ms on the MPS and MHS are presented in Fig. 6.3. Because $P_{\mathrm{C\_MPS}}$ increases rapidly with an increase in a/b, the Wenzel state, transition state, and Cassie state are obtained on the S-MPS, M-MPS, and L-MPS, respectively. Liquid replaces the air in the pillar space and wets the S-MPS completely, forming a Wenzel state, whereas liquid penetration is inhibited on the L-MPS due to the larger pillar size and smaller pillar space, forming the Cassie state. To design a superhydrophobic surface, a small f_{s} is needed according to Eq.(6.2). Hence, decorating surfaces with multiple pillars faces a contradiction between improving the surface hydrophobicity and the wetting stability. On all MHSs, liquid contacts only the outermost tops of the structures, forming a stable Cassie state, because, in the hole, the air is not replaced by the liquid, but is entrapped underneath forming an air pocket. The existence of air pockets can withstand the deformation of droplets on the structure,

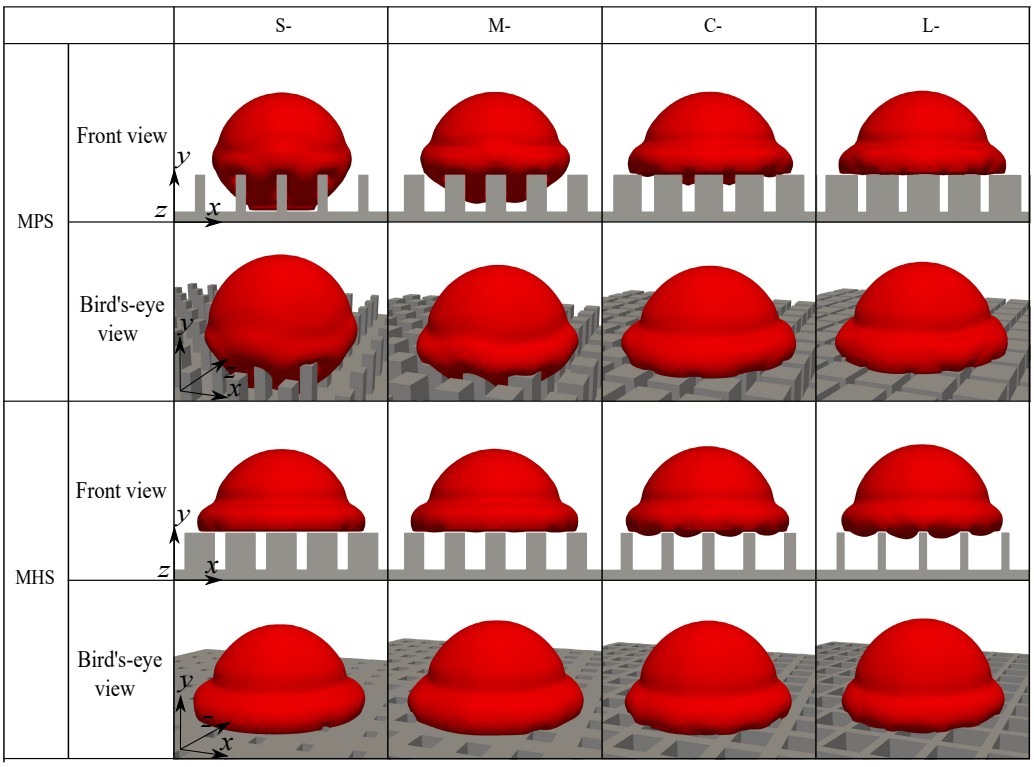

Figure 6.3: Wetting states at 1.8ms of a droplet impinging on the MPS and MHS.

thus leading to a stable Cassie state even under an impinging condition.

To understand how the surface structure affects the liquid penetration, the schematics shown in Fig. 6.4 indicating the deformation of droplets on the MPS and the MHS. During the spreading and penetration process, on the MPS, the deformation of the liquid induces a depinning of the TPCL at the edge of the pillars. With the sliding of the TPCL on the sidewall of the pillars, the Cassie-to-Wenzel transition takes place when the surface is completely wetted. On the MHS, however, the TPCL is always pinned on the top edge of the holes. The deformation of the liquid only leads to a sagging of the interface. Thus, the MHS prevents a rough structure from completely wetting during the spreading phase. In the recoiling phase, the liquid in the Wenzel state in Fig. 6.4(a) may not leave the surface because of the arresting state by the pillars, whereas the interface in Fig. 6.4(b) can withdraw from the holes and bounce off the surface.

To characterize the wetting behavior of a droplet, we measure the maximum pen-

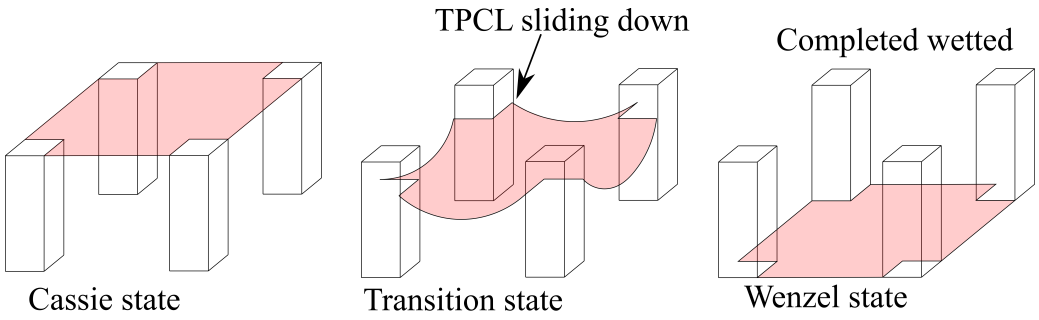

(a) Cassie-to-Wenzel transition on the MPS

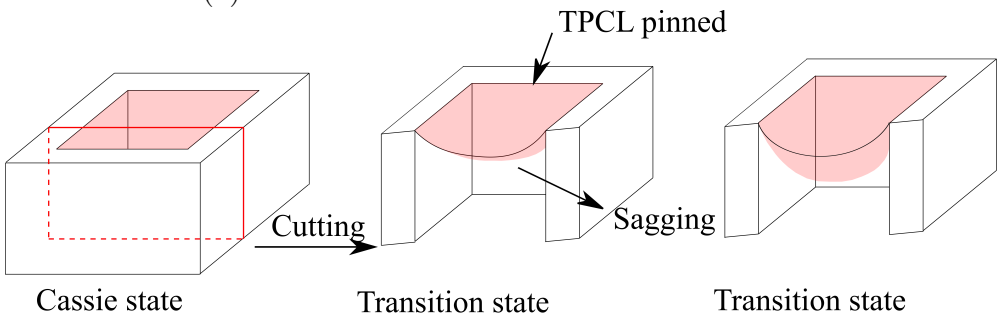

(b) Superstable Cassie state on the MHS

Figure 6.4: Schematics describing the evolution of a curved interface (in pink) when a droplet impinges on a structural substrate: (a) Cassie-to-Wenzel transition of a droplet impinging on the S-MPS; (b) Superstable Cassie state of a droplet impinging on the L-MHS, with the red lines indicating the cutting position to show the shape of the interface.

etration factor ($\eta_{\max}$) and the contact time (t_c). The maximum penetration factor is defined as $\eta_{\max} = H_{\max}/h$, where $H_{\max}$ is the maximum penetration depth, referring to the distance between the bottom of the liquid−air interface and the outermost top of the structures. The contact time (t_c) is the the time period from when the drop first touches the surface to when it bounces off. Figure 6.5 plots $\eta_{\max}$ and t_c against a/b. The starting time is noted when the droplet starts contacting the solid. On the MPS, $\eta_{\max}$ decreases with an increase in a/b, which is caused by an increase in the Capillary pressure (P_C). On the MHS, however, $\eta_{\max}$ is a constant of close to zero over a range of a/b of 0.25 to 0.7, when the perfect Cassie state is obtained. A sharp increase is observed with a/b ranging from 0.7 to 0.8 because of the sagging of the interface as shown in Fig.6.4(b).

As for the contact time, t_c on a flat surface is yielded by balancing the inertia (on the

order of $\rho_l D_0/2t_c^2$) with capillarity ($4\sigma/{D_0}^2$), and scaled as $t_c \approx (\rho_l {D_0}^3/8\sigma)^{1/2}$ [35]. The value of t_c in this study, however, is also influenced by the wetting state of the droplet. During the droplet−wall interaction, the spreading, emptying, and retracting behaviors of a droplet are observed on textured surfaces. The emptying time (t_e) indicates the time interval between the moments when the droplet first touches the solid structure and when the liquid in the pattern space is completely emptied, during which the droplet undergoes downward penetration and upward capillary emptying processes [3]. The penetration of the liquid, particularly in a visible Wenzel state on the S-MPS and the M-MPS, happens with a/b ranging from 0.25 to 0.7. Under this situation, the dominant

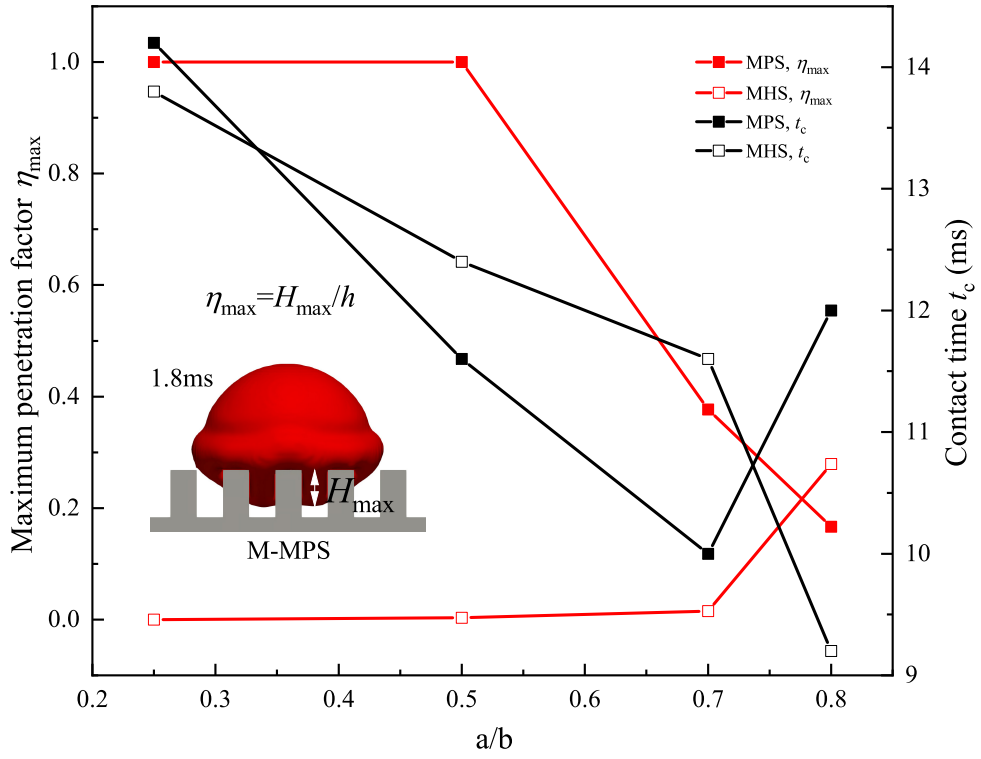

Figure 6.5: Variations of the maximum penetration factor (η_{max}) and the contact time (t_c) with a/b between 0.25 and 0.8 on the MPS and MHS. H_{max} is the maximum penetration depth, and η_{max} is the maximum penetration factor.

part of the contact is the liquid penetration and surface emptying, and thus $t_c \sim t_e$,

$$t_e \sim -\frac{u_0 \rho_l D_0 b^2}{2a\sigma \cos\theta_Y} \tag{6.4}$$

From Eq. (6.4), the increase in a/b leads to the decline of t_e. Hence, a decreasing t_c is shown in Fig. 6.5. However, t_c increases with a/b between 0.7 and 0.8, demonstrating the decrease in surface hydrophobicity according to Eq. (6.1). On the L-MPS, a Cassie state is obtained, and the droplet undergoes spreading and recoiling phases on the outermost of pillars. In this case, t_c can be approximately scaled as $t_c \approx t_s + t_r$, where, t_s represents the spreading time, at which the droplet spreads and reaches its maximum spreading stage. Shen et al. [36] proposed an equation to estimate t_s based on the energy conservation law, but such an equation is incorrect, because it is not homogeneous to a time according to the dimensionality check. We re-derived this equation, and t_s can be estimated by Eq. (6.5). In addition, t_r is the recoiling time estimated by Eq. (6.6) for $We \gg 1$ [35], meaning the time interval from when the droplet starts to recoil to when it bounces off the surface.

$$t_s \sim \frac{2}{3}\sqrt{\frac{D_0}{\rho_l \mu u_0}}\left(\frac{\rho_l D_0^3 u_0^2 + 12\sigma D_0^2 - 3\sigma {D^2}_{\max}(1-\cos(\theta_{app}))}{{D^2}_{\max} u_0^2}\right) \tag{6.5}$$

$$t_r \propto \sqrt{\frac{\rho_l D_0^3}{2\sigma\pi\left[1-\cos\left(\theta_{app}\right)\right]}} \tag{6.6}$$

where D_{max} is the maximum spreading diameter [37] that can be estimated by,

$$\frac{D_{max}}{D_0} = \sqrt{\frac{We+12}{3\left(1-\cos\left(\theta_{app}\right)\right)+4We/\sqrt{Re}}} \tag{6.7}$$

The increase in a/b brings an increase in the solid fraction (f_s^{MPS}) and thus lowers the apparent contact angle θ_{app} according to Eq. (6.1). When we insert Eq.(6.7) into Eqs. (6.5) and (6.6), an increase in t_c is found with a/b increasing from 0.7 to 0.8 in a Cassie state.

For a droplet impinging on the MHS, t_c decreases almost linearly. This is because, with an increase in a/b, θ_{app} increases due to the decrease in f_s^{MHS}. Because a stable

Cassie state is achieved from the S-MHS to the L-MHS, the decrease in t_c is shown in Fig. 6.5 when we combine Eqs. (6.5) and (6.6).

6.3.2 Pressure analysis

To elucidate the origin of the penetration on the S-MPS and the sagging on the L-MHS, we show the variation of the local pressure and velocity in the cross-sectional plan in Fig. 6.6. The left panel of each image is colored based on the pressure ranging between 100kPa and 101kPa, and the arrows in the right panel are colored based on the velocity from 0 to $2u_0$. On the S-MPS, a large pressure can be seen at the liquid−solid contact

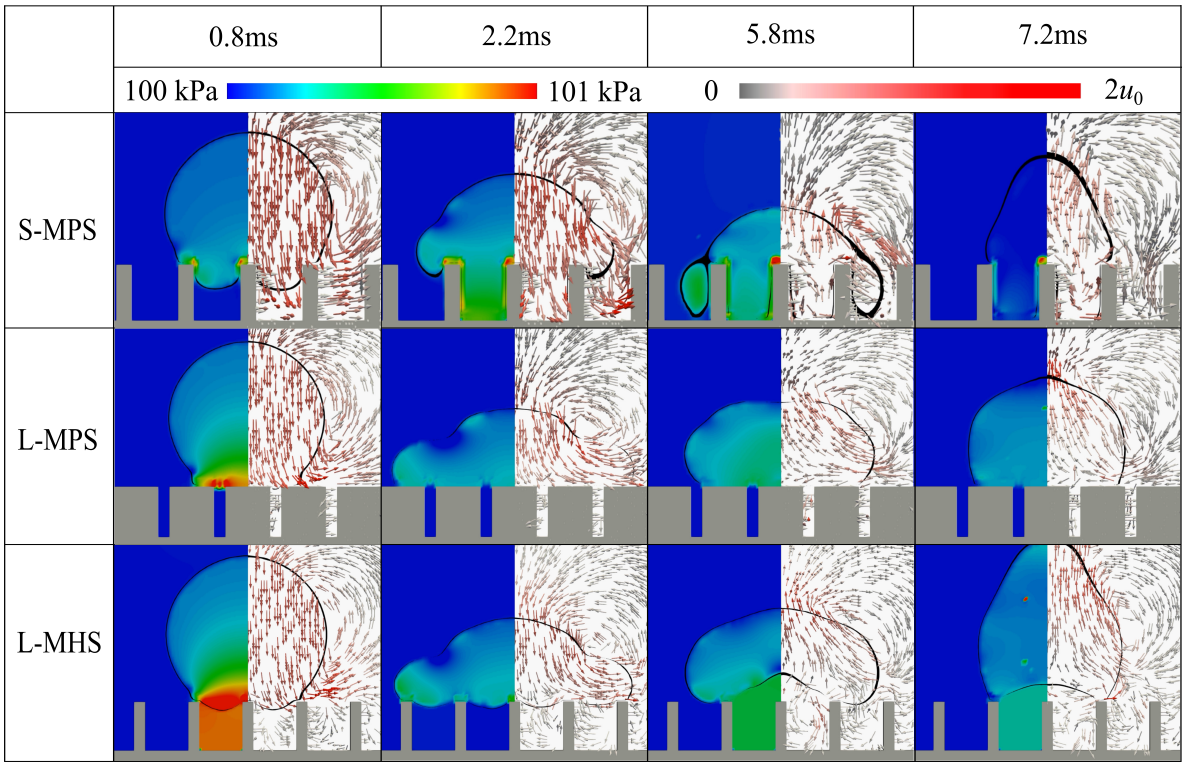

Figure 6.6: Pressure contour (left panel, colored based on pressure) and the velocity field (right panel, colored based on velocity) at the cross-sectional plane on the S-MPS, L-MPS, and L-MHS. The liquid−air interface (VOF function: C=0.5) is represented by the black lines.

area, and the liquid penetrates into the pillar space from 0.8 to 5.8ms, because the air in the pillar space flows freely, and is easily pushed out by the liquid. Thus, the surface is completely wetted, forming a Wenzel state. On the L-MPS, although the free-flowing air exists in the pillar space, a large a/b brings about a larger $P_{\mathrm{C\_MPS}}$, leading to a Cassie state when $P_{\mathrm{C}} > P_{\mathrm{WH}} > P_{\mathrm{D}}$ is satisfied. For the case with the L-MHS, air pockets are formed in the holes, and the air pressure in the holes varies with a deformation of the droplet. At 0.8ms in the impact stage, high-pressure areas appear in the hole, which is totally different from that on the S-MHS and L-MPS. At 5.8ms, subsequently, high-pressure areas appear again in the hole due to a compressing of the recoiling liquid. Therefore, the robust air pocket in the holes prevents the liquid from penetration.

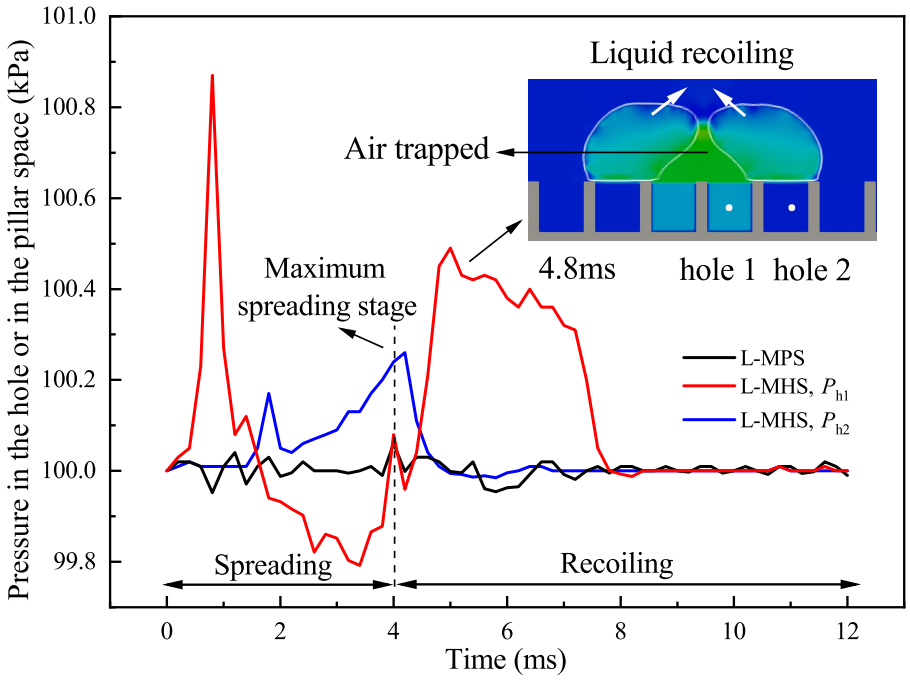

Figure 6.7: Pressure variation in the pillar space for the L-MPS and in the holes for the L-MHS. Here, P_{h1} and P_{h2} are the pressures measured in the hole 1 (close to the impingement center) and hole 2 (far from the impingement center) in the image (colored by the pressure as the left panel in Fig. 6.6), respectively. White arrows show the direction of the recoiling flows.

Figure 6.7 provides statistical information on the pressure in the pillar space for the L-MPS and in the holes for the L-MHS. On the L-MPS, it is clear that the pressure in the pillar space is nearly constant at approximately P_0=100kPa. On the L-MHS, however, the pressure varies rapidly in both the spreading and recoiling phases. In the spreading phase, P_{h1} increases sharply, and then decreases with a spreading of the center liquid. Here, P_{h1} returns to near P_0 at the maximum spreading stage. The liquid then starts recoiling, and the air in the center is trapped as shown in the image at 4.8ms. Owing to the compression of the recoiling liquid, a high P_{h1} appears again. The value of P_{h1} decreases to near P_0, when the droplet bounces off the substrate. In addition, P_{h2} shows a slight increase when the maximum spreading stage is reached. Then, P_{h2} decreases to near P_0 with a retracting of the liquid.

To better understand the effect of the pressure change on the stability of the liquid-air

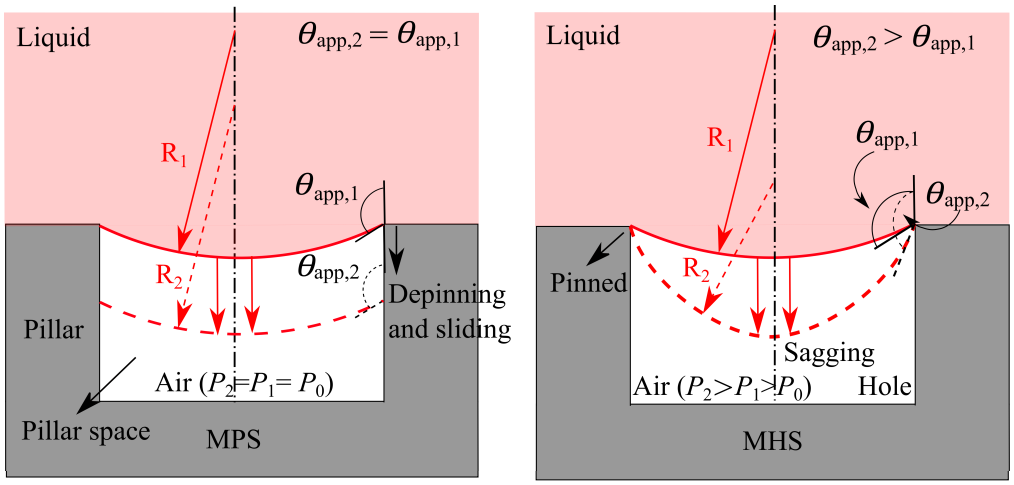

(a) Depinning penetration (b) Sagging penetration

Figure 6.8: Schematic diagram (sectional view) of the penetration mechanisms: (a) depinning penetration on the S-MPS; (b) sagging penetration on the L-MHS. Solid lines and arrows represent state 1, and the dash lines and arrows represent state 2. Here, R, θ_{app}, and P are the radius of the interface, the apparent contact angle, and the pressure in the air region, respectively. Subscripts 1 and 2 indicate the value of the parameter under states 1 and 2.

interface, we next turn to the theoretical analysis shown in Fig.6.8. The liquid penetration occurs when the energy of the droplet exceeds the potential barrier separating the Cassie and the Wenzel states. The energy barrier, represented by the breakthrough pressure (P_{b}) in this study, is derived based on the correlation of Laplace's law, Young's equation, and a Gibbs extension [23, 38–40],

$$P_{\mathrm{b}} = \frac{4\sigma \sin\left(\theta_{\mathrm{Y}} - \Psi\right)}{W_{\mathrm{s}}} \tag{6.8}$$

Here, Ψ the geometrical edge angle ($\Psi = \pi/2$ in our system). This equation illustrates that P_{b} increases with a decrease in W_{s}. In Fig. 6.3, therefore, the Wenzel, transition, and Cassie states are observed on the MPS with an increase in a.

Laplace's law describes the relationship among the pressure difference (ΔP, on both sides of the interface), the surface tension coefficient (σ), and the interface curvature (κ):

$$\Delta P = 2\sigma\kappa \tag{6.9}$$

We assume that the interface has the profile of a spherical cap with a curvature radius R, in which R can be estimated by

$$R = \frac{1}{\kappa} = \frac{W_{\mathrm{s}}}{2\sin\left(\theta_{\mathrm{app}} - \pi\right)} \tag{6.10}$$

When we combine Eqs. (6.9) and (6.10), the ΔP is expressed as

$$\Delta P = P_{\mathrm{t}} - P_a = \frac{4\sigma \sin\left(\theta_{\mathrm{app}} - \pi\right)}{W_{\mathrm{s}}} \tag{6.11}$$

where P_a is the air pressure in the pillar space or holes, which is represented by P_1 and P_2 under states 1 and 2, as shown in Fig. 6.8. In addition, P_{t} is the total pressure inside the liquid phase, and is estimated by

$$P_{\mathrm{t}} = P_0 + P_{\mathrm{hd}} + P_{\mathrm{hs}} = P_0 + \frac{1}{2}\rho_l {u_0}^2 + \rho_l g D_0 \tag{6.12}$$

where P_{hd} is the hydrodynamic pressure, and P_{hs} the hydrostatic pressure.

A stable Cassie state is obtained when $\Delta P < P_{\mathrm{b}}$. Conversely, the penetration occurs with $\Delta P > P_{\mathrm{b}}$. The schematics in Fig. 6.8 describe the penetration mechanism of the

liquid on the MPS and MHS. At state 1, droplets on the MPS and MHS have the same radius (R_1) and apparent contact angle ($\theta_{\mathrm{app},1}$) but different air pressure (P_1). On the MPS, because the air in the pillar space can flow freely, the interface slides down the side of the pillar with R_2=R_1, $\theta_{\mathrm{app},2}$=$\theta_{\mathrm{app},1}$, and P_2=P_1=P_0. On the MHS, however, the sagging of the interface brings $\theta_{\mathrm{app},2} > \theta_{\mathrm{app},1}$, $R_2 < R_1$, and $P_2 > P_1$ according to Eqs. (6.9)−(6.12). Hence, the greater the sagging is, the greater the value of P_{a} and the smaller the value of ΔP. When $\Delta P \leq P_{\mathrm{b}}$ is satisfied, the sagging penetration stops. We again emphasize that the robust air pocket in the MHS is the fundamental reason for inhibiting the depinning of the TPCL.

6.3.3 Larger We effect

A stable Cassie state is obtained on all MHSs above with $We = 10$. Eq. (6.12) illustrates the total pressure (P_{t}) increases with an increase in the initial impingement velocity (u_0). Can the Cassie state survive if the droplet heads to an MHS with large impinging velocities?

Figure 6.9 presents the maximum pressure in holes 1 and 2 ($P_{\mathrm{h1,m}}$ and $P_{\mathrm{h2,m}}$, respectively) as a function of We on an L-MHS. Both $P_{\mathrm{h1,m}}$ and $P_{\mathrm{h2,m}}$ increase nearly linearly with approximate slope of 50:1 for a different We. For a small We at 10, $P_{\mathrm{h2,m}}$ is slightly larger than P_0. As We increases, both $P_{\mathrm{h1,m}}$ and $P_{\mathrm{h2,m}}$ increase rapidly. Owing to the change in pressure in the air pocket, the pressure difference ΔP at the sagging interface is insufficiently high to trigger a liquid penetration. Hence, a Wenzel state is not observed even under an extremely large We at 100.

The maximum penetration factor (η_{max}) is plotted against We in Fig. 6.10. The sequence of cut droplets is indicated to clearly show the penetration in holes 1 and 2. Under a small We condition, the liquid penetration is inhibited due to the variation in $P_{\mathrm{h1,m}}$ and $P_{\mathrm{h2,m}}$. With an increase in We, liquid penetration is vividly observed at hole 2, and the line slope for We <60 is relatively smaller than that for 60≤ We ≤80. In addition, η_{max} is achieved in hole 1 when $We < 60$, whereas the liquid slides down and

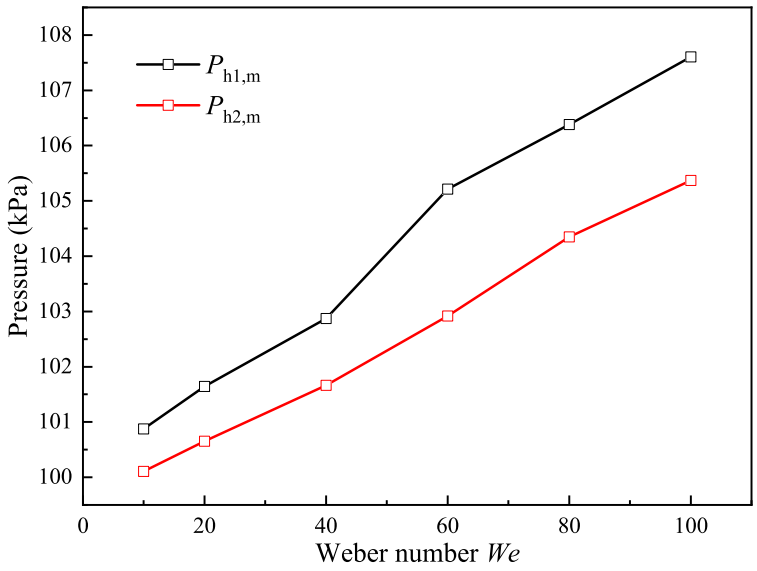

Figure 6.9: Maximum pressure ($P_{h1,m}$ and $P_{h2,m}$ in holes 1 and 2, respectively) in the air pocket on the L-MHS as a function of We from 10 to 100, or u_0 from 0.603 to 1.908 m/s.

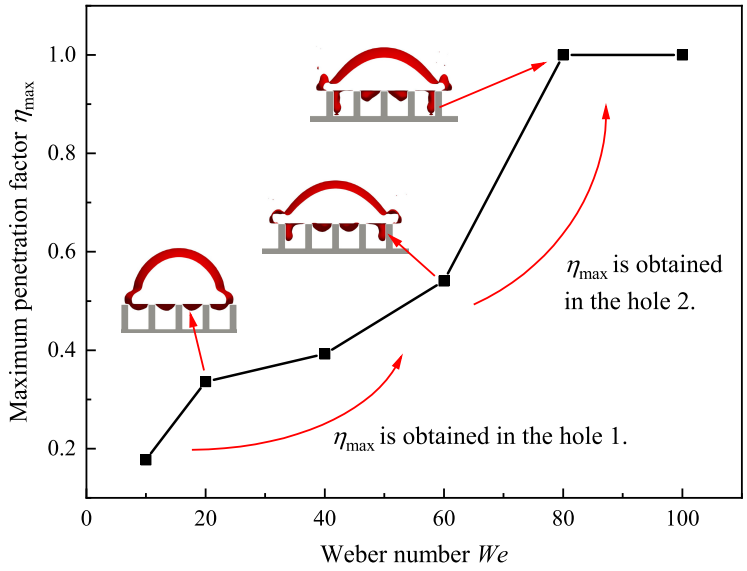

Figure 6.10: Variation of the maximum penetration factor (η_{max}) of a droplet under We from 10 to 100, or u_0 from 0.603 m/s to 1.908 m/s.

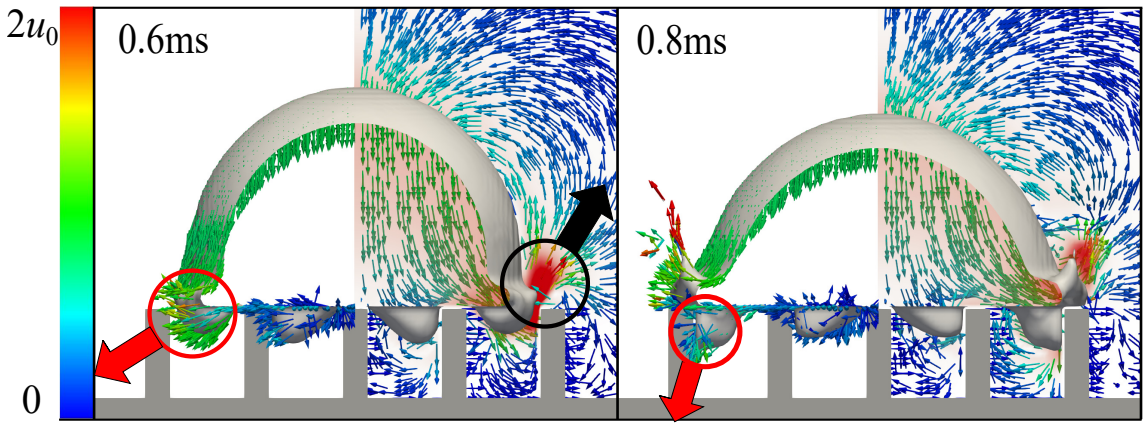

Figure 6.11: Velocity field describing the liquid penetration in hole 2 on the L-MHS with large We=60, or u_0=1.48m/s. The left panel shows the velocity field at the liquid−air interface, and the right panel presents the velocity field on the cross-sectional plane. The red and black arrows show the flow direction of the interface and air, respectively. The small arrows are colored based on a velocity of 0 to $2u_0$.

touches the hole bottom with We from 60 to 100, leading to $\eta_{\max}$=1.0.

The velocity field in Fig. 6.11 is employed to complement the statistical information in Fig. 6.10 and investigate the penetration mechanism under a large We. The droplet (represented by VOF function C=0.5) is colored in grey. The left panel shows the velocity field at the liquid-air interface, and the right panel presents the velocity field on the cross-sectional plane. At 0.6 ms, the liquid rim indicated by the red circle tends to infiltrate into the hole owing to the large impinging velocity, and simultaneously, the portion of air shown in the black circle is rapidly squeezed out of the hole. Owing to the weak air pocket in hole 2, at 0.8 ms, the liquid slides down the sidewall of hole 2. As a result, the liquid will wet the bottom of the hole, leading to $\eta_{\max}$=1.0 with a further increase in We.

6.3.4 Theoretical formulation of the maximum spreading factor

The maximum spreading factor ($\beta_{\max}$), defined as $\beta_{\max} = D_{\max}/D_0$, depends on the liquid properties such as the density (ρ_l), viscosity (μ_l), surface tension (σ), intrinsic

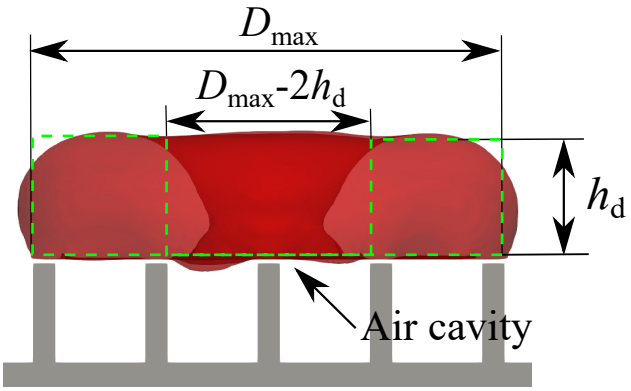

Figure 6.12: Donut-like droplet (50% transparent) at the maximum spreading stage. Here, D_{max} and h_d are the maximum spreading diameter and the thickness of the rim, respectively. The green dashed line outlines a donut-like droplet.

contact angle (θ_Y), and surface roughness, where D_{max} is the maximum spreading diameter shown in Fig. 6.12. Accurately predicting the maximum spreading factor is important for understanding the deformation of an impinging droplet. Most theoretical models based on the energy conservation principle have been proposed to predict β_{max} on smooth and rough substrates. However, these models take many assumptions. For instance, the drop shape at the maximum spreading stage is usually assumed as a cylinder [37, 41] or a central cylinder wrapped by another semi-cylinder [7]; however, experimental [42–44] and numerical [44, 45] evidence shows that the top surface of the droplet is not flat. With the deformation of the droplet, an air cavity is present at the center of the droplet, forming a donut- or ring-like profile. In addition, little consideration has been given to the influence of energy loss of the TPCL depinning when a droplet spreads on a textured surface.

Here, a donut-like droplet is selected to deduce the new theoretical model. Its profile can be roughly represented by the green dashed line in Fig. 6.12, and we assume that the width of the rim is equal to its height, leading to the diameter of the cavity at $(D_{max} - 2h_d)$, where h_d is the thickness of the rim, and its value (relevant to D_{max}) can be estimated based on the volume conservation law.

Beginning with the energy conservation principle, at the initial and the maximum

spreading states, if we neglect the possible contributions to the momentum given by internal motions of particles with respect to the total droplet momentum, we have

$$E_{s0} + E_{k0} = E_{sm} + W_{vis} + W_{pin} \tag{6.13}$$

where E_{s0} and E_{k0} are the surface energy and kinetic energy prior to impact, and E_{sm}, W_{vis}, and W_{pin} at the maximum spreading state are the surface energy, viscous dissipation, and energy loss due to the pinning of the TPCL during the spreading across the hole edges, respectively.

For the impact droplet with the initial impinging velocity u_0, the energy terms at the initial stage can be estimated by

$$E_{s0} = \pi D_0^2 \sigma \tag{6.14}$$

$$E_{k0} = \frac{\pi}{12} \rho_l u_0^2 D_0^3 \tag{6.15}$$

Considering the stable Cassie state on the MHS, the surface energy at the maximum spreading stage [7] is obtained by

$$E_{sm} \approx \sigma \left[\pi D_{max} h_d + \frac{\pi}{4} D_{max}^2 \left(\xi + f_a^{MHS} \right) \right] + \frac{\pi}{4} D_{max}^2 f_s^{MHS} \sigma \cos\theta_Y \tag{6.16}$$

where ξ is the factor introduced in this study and is estimated by

$$\xi = \frac{A_d}{A_c} = 1 + \frac{4(D_{max} - 2h_d)h_d}{D_{max}^2} \tag{6.17}$$

Here, A_d is the area of the top surface when the droplet is assumed to take a donut-like shape, and A_c is the area of the top surface for a cylinder-like droplet. In addition, $\xi = 1.0$ is satisfied if a cylinder-like shape is employed. Considering the real droplet shape, its value is often greater than 1.0 and ranges between 1.1 and 1.5 in the present cases.

The energy lost in deforming the droplet against the viscosity is expressed approximately as follows [37]:

$$W_{vis} = \frac{\pi}{3\sqrt{Re}} \rho_l u_0^2 D_{max}^2 D_0 \tag{6.18}$$

Table 6.3: Comparison of theoretical models with our new model in Eq. (6.20) for the maximum spreading factor.

Reference	Target surface	Equation
Fard et al. [37]	Flat	$\beta_{\max} = \sqrt{\frac{We+12}{3(1-\cos(\theta_{\text{app}}))+4We/\sqrt{Re}}}$
Lee et al. [41]	MHS	$(We+12)\beta_{\max} = 8 + \beta_{\max}^3 \left[4\frac{We}{\sqrt{Re}} - 3\psi\right]$
New model	MHS	Eq. (6.20)

* ψ is a roughness and wetting state related factor [41].

When liquid encounters the hole edge, energy loss takes places to overcome the contact line pinning force. Vaikuntanathan et al. [7] proposed a model to calculate the energy loss in the perpendicular groove direction on groove-textured surfaces. Here, we extend the model to predict the energy loss on surfaces with pillars or holes, which is written as

$$W_{\text{pin}} = N_{\text{h}}\left(\frac{F_{\text{Y}} D_{\max}}{2}\right) \approx \frac{\pi^2 D_{\max}^4}{4b^2}\sigma\left(\cos\theta_{\text{Y}} - \cos\theta_{\text{app}}\right) \tag{6.19}$$

Here, F_{Y} is Young's force, N_{h} is the number of hole edges encountered during spreading, and $N_{\text{h}} = \frac{\pi D_{\max}^2}{2b^2}$.

By substituting Eqs. (6.14) − (6.19) into Eq. (6.13), a final form for the maximum spreading factor ($\beta_{\max} = D_{\max}/D_0$) is derived as follows

$$\begin{aligned}\left[\frac{3\pi D_0^2}{b^2}\left(\cos\theta_{\text{Y}} - \cos\theta_{\text{app}}\right)\right]\beta_{\max}^5 \\ + \left[3\left[\left(\xi + f_a^{\text{MHS}}\right) + \left(f_{\text{s}}^{\text{MHS}}\cos\theta_{\text{Y}}\right)\right] + \frac{4We}{\sqrt{Re}}\right]\beta_{\max}^3 \\ - (We+12)\beta_{\max} + 8 = 0\end{aligned} \tag{6.20}$$

To validate the new model, we conduct comparisons between Eq. (6.20) and the models in articles as shown in Table 6.3. The widely used model proposed by Fard et al. [37] matches the experimental results well on a flat surface but cannot be employed

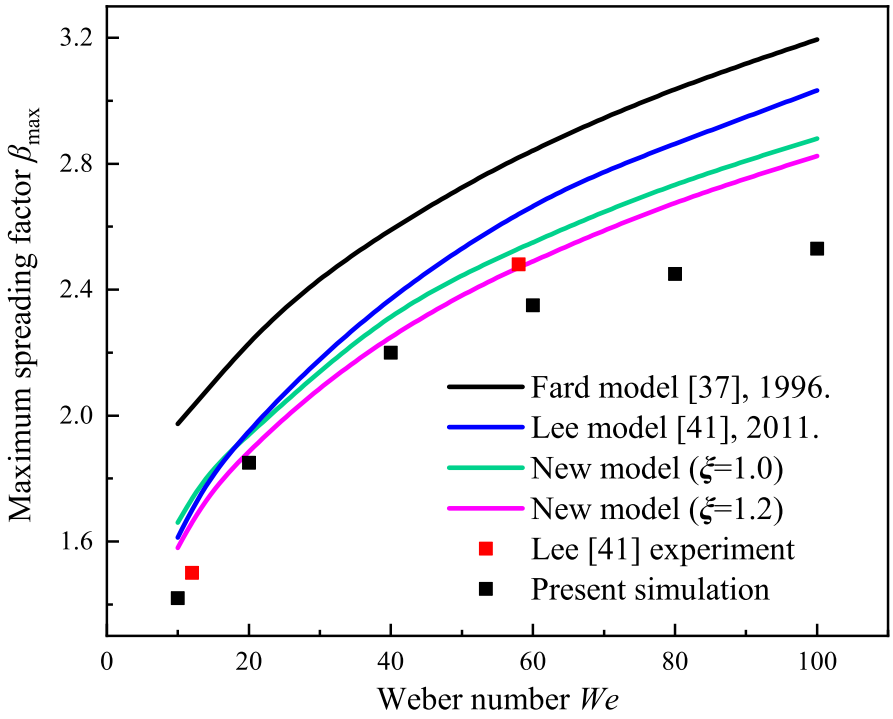

Figure 6.13: Comparison of the maximum spreading factor ($\beta_{\max}$) predicated by theoretical models and numerical results against We from 10 to 100, for u_0 from 0.603 to 1.908 m/s.

to predict $\beta_{\max}$ on a textured surface. Lee et al. [41] derived a model for predicting $\beta_{\max}$ on a MHS; however, compared with the experimental results, their model illustrates an over-predictive result because W_{pin} is not considered.

Figure 6.13 shows a comparison among the experiment [41], our simulation, and theoretical predications by Fard et al. [37], Lee et al. [41], and our new models with $\xi = 1.0$ and $\xi = 1.2$. First, compared with the experimental results, $\beta_{\max}$ is over−estimated using the model proposed by Fard et al. [37] and Lee et al. [41]. In contrast, $\beta_{\max}$ predicted by the new model shows an extremely good agreement with experimental results when $\xi = 1.2$. Second, at a small We, no significant difference in $\beta_{\max}$ is observed between the theoretical and simulation results. Under large We conditions, the simulation results are smaller than the experimental results and theoretical predications. This difference is caused by the liquid penetration, as shown in Figs. 6.10 and 6.11.

6.4 Conclusions

DNS was conducted to capture the rapid transient interaction between impinging droplets and surfaces with multiple pillars (MPS) and multiple holes (MHS). The pressure analysis clearly showed the fundamental reason for the liquid penetration and wetting transition. The robustness of the air pocket in the MHS was examined by releasing a droplet with an extremely large We. A new model for the maximum spreading factor ($\beta_{\max}$) was derived. The main results obtained in this chapter are summarized as follows.

1. Compared with the MPS, the MHS not only enhances the surface hydrophobicity but also greatly stabilizes the Cassie state of an impinging droplet.

2. The varying pressure in the air pocket inhibits the depinning of the TPCL. This is the fundamental reason for obtaining a superstable Cassie state on the MHS.

3. Although a large We triggers the depinning of the TPCL in some holes, a significant number of liquid−air interfaces hang between structures, and a Wenzel state is not obtained on the MHS.

4. The new model for the maximum spreading factor ($\beta_{\max}$), considering the air cavity at center of the droplet and the energy loss of the TPCL depinning, is derived based on the law of energy conservation. The new model is in better agreement with experimental and simulation results than previously proposed models.

References

[1] D. Quéré. Rough ideas on wetting. *Physica A*, 313(1-2):32–46, 2002.

[2] D. Quéré. Wetting and roughness. *Annu. Rev. Mater. Res.*, 38:71–99, 2008.

[3] Y. Liu, L. Moevius, X. Xu, T. Qian, J. M. Yeomans, and Z. Wang. Pancake bouncing on superhydrophobic surfaces. *Nat. Phys.*, 10(7):515–519, 2014.

[4] J. Song, M. Gao, C. Zhao, Y. Lu, L. Huang, X. Liu, C. J. Carmalt, X. Deng, and I. P. Parkin. Large-area fabrication of droplet pancake bouncing surface and control of bouncing state. *ACS Nano*, 11(9):9259–9267, 2017.

[5] C. Liu, H. Zhan, J. Yu, R. Liu, Q. Zhang, Y. Liu, and X. Li. Design of superhydrophobic pillars with robustness. *Surf. Coat. Technol.*, 361:342–348, 2019.

[6] C. Guo, D. Zhao, Y. Sun, M. Wang, and Y. Liu. Droplet impact on anisotropic superhydrophobic surfaces. *Langmuir*, 34(11):3533–3540, 2018.

[7] V. Vaikuntanathan and D. Sivakumar. Maximum spreading of liquid drops impacting on groove-textured surfaces: Effect of surface texture. *Langmuir*, 32(10):2399–2409, 2016.

[8] H. Mayama, T. Nishino, A. Sekiguchi, R. Nishimura, K. Uchida, S. Yokojima, S. Nakamura, and Y. Nonomura. Theoretical consideration of wetting in Cassie-Baxter state on multi-pillar and multi-hole surfaces: Thermodynamics and Laplace pressure. *J. Photopolym. Sci. Technol.*, 32(2):279–285, 2019.

[9] V. Bahadur and S. V. Garimella. Preventing the Cassie-Wenzel transition using surfaces with noncommunicating roughness elements. *Langmuir*, 25(8):4815–4820, 2009.

[10] R. N. Wenzel. Resistance of solid surfaces to wetting by water. *Ind. Eng. Chem.*, 28(8):988–994, 1936.

[11] E. Bormashenko, R. Pogreb, G. Whyman, Y. Bormashenko, and M. Erlich. Vibration-induced Cassie-Wenzel wetting transition on rough surfaces. *Appl. Phys. Lett.*, 90(20):201917, 2007.

[12] M. Nosonovsky. Multiscale roughness and stability of superhydrophobic biomimetic interfaces. *Langmuir*, 23(6):3157–3161, 2007.

[13] K. Koch, B. Bhushan, Y. C. Jung, and W. Barthlott. Fabrication of artificial Lotus leaves and significance of hierarchical structure for superhydrophobicity and low adhesion. *Soft Matter*, 5(7):1386–1393, 2009.

[14] M. S. Bell, A. Shahraz, K. A. Fichthorn, and A. Borhan. Effects of hierarchical surface roughness on droplet contact angle. *Langmuir*, 31(24):6752–6762, 2015.

[15] Z. Lian, J. Xu, W. Ren, Z. Wang, and H. Yu. Bouncing dynamics of impact droplets on the biomimetic plane and convex superhydrophobic surfaces with dual-level and three-level structures. *Nanomaterials*, 9(11):1524, 2019.

[16] R. Pan, M. Cai, W. Liu, X. Luo, C. Chen, H. Zhang, and M. Zhong. Extremely high Cassie–Baxter state stability of superhydrophobic surfaces via precisely tunable dual-scale and triple-scale micro–nano structures. *J. Mater. Chem. A*, 7(30):18050–18062, 2019.

[17] R. Roy, J. A. Weibel, and S. V. Garimella. Re-entrant cavities enhance resilience to the Cassie-to-Wenzel state transition on superhydrophobic surfaces during electrowetting. *Langmuir*, 34(43):12787–12793, 2018.

[18] M. Nosonovsky and B. Bhushan. Why re-entrant surface topography is needed for robust oleophobicity. *Phil. Trans. R. Soc. A*, 374(2073):20160185, 2016.

[19] E. Bormashenko and G. Whyman. On the role of the line tension in the stability of Cassie wetting. *Langmuir*, 29(18):5515–5519, 2013.

[20] H.-Y. Guo, B. Li, and X.-Q. Feng. Stability of Cassie-Baxter wetting states on microstructured surfaces. *Phys. Rev. E*, 94(4):042801, 2016.

[21] B. Zhang and X. Zhang. Elucidating nonwetting of re-entrant surfaces with impinging droplets. *Langmuir*, 31(34):9448–9457, 2015.

[22] J. Wang, F. Liu, H. Chen, and D. Chen. Superhydrophobic behavior achieved from hydrophilic surfaces. *Appl. Phys. Lett.*, 95(8):084104, 2009.

[23] R. Hensel, R. Helbig, S. Aland, H.-G. Braun, A. Voigt, C. Neinhuis, and C. Werner. Wetting resistance at its topographical limit: The benefit of mushroom and serif T structures. *Langmuir*, 29(4):1100–1112, 2013.

[24] Y. Xue, S. Chu, P. Lv, and H. Duan. Importance of hierarchical structures in wetting stability on submersed superhydrophobic surfaces. *Langmuir*, 28(25):9440–9450, 2012.

[25] P. Lv, Y. Xue, Y. Shi, H. Lin, and H. Duan. Metastable states and wetting transition of submerged superhydrophobic structures. *Phys. Rev. Lett.*, 112(19):196101, 2014.

[26] A. Hemeda and H. V. Tafreshi. General formulations for predicting longevity of submerged superhydrophobic surfaces composed of pores or posts. *Langmuir*, 30(34):10317–10327, 2014.

[27] A. Albadawi, D. Donoghue, A. Robinson, D. Murray, and Y. Delauré. Influence of surface tension implementation in volume of fluid and coupled volume of fluid with level set methods for bubble growth and detachment. *Int. J. Multiph. Flow*, 53:11–28, 2013.

[28] K. Yokoi. A practical numerical framework for free surface flows based on CLSVOF method, multi-moment methods and density-scaled CSF model: Numerical simulations of droplet splashing. *J. Comput. Phys.*, 232(1):252–271, 2013.

[29] J. Wen, Y. Hu, A. Nakanishi, and R. Kurose. Atomization and evaporation process of liquid fuel jets in crossflows: A numerical study using Eulerian/Lagrangian method. *Int. J. Multiph. Flow*, 129:103331, 2020.

[30] A. Cassie and S. Baxter. Wettability of porous surfaces. *Trans. Faraday Soc.*, 40:546–551, 1944.

[31] T. Deng, K. K. Varanasi, M. Hsu, N. Bhate, C. Keimel, J. Stein, and M. Blohm. Nonwetting of impinging droplets on textured surfaces. *Appl. Phys. Lett.*, 94(13):133109, 2009.

[32] D. Hee Kwon and S. Joon Lee. Impact and wetting behaviors of impinging micro-droplets on superhydrophobic textured surfaces. *Appl. Phys. Lett.*, 100(17):171601, 2012.

[33] T. Bobinski, G. Sobieraj, M. Psarski, G. Celichowski, and J. Rokicki. Droplet bouncing on the surface with micro-structure. *Arch. Mech*, 69:177–193, 2017.

[34] R. Rioboo, M. Marengo, and C. Tropea. Time evolution of liquid drop impact onto solid, dry surfaces. *Exp. Fluids*, 33(1):112–124, 2002.

[35] D. Richard, C. Clanet, and D. Quéré. Contact time of a bouncing drop. *Nature*, 417(6891):811–811, 2002.

[36] Y. Shen, J. Tao, H. Tao, S. Chen, L. Pan, and T. Wang. Approaching the theoretical contact time of a bouncing droplet on the rational macrostructured superhydrophobic surfaces. *Appl. Phys. Lett.*, 107(11):111604, 2015.

[37] M. Pasandideh-Fard, Y. Qiao, S. Chandra, and J. Mostaghimi. Capillary effects during droplet impact on a solid surface. *Phys. Fluids*, 8(3):650–659, 1996.

[38] R. Hensel, A. Finn, R. Helbig, S. Killge, H.-G. Braun, and C. Werner. In situ experiments to reveal the role of surface feature sidewalls in the Cassie–Wenzel transition. *Langmuir*, 30(50):15162–15170, 2014.

[39] T. M. Schutzius, G. Graeber, M. Elsharkawy, J. Oreluk, and C. M. Megaridis. Morphing and vectoring impacting droplets by means of wettability-engineered surfaces. *Sci. Rep.*, 4:7029, 2014.

[40] J. Oliver, C. Huh, and S. Mason. Resistance to spreading of liquids by sharp edges. *J. Colloid Interface Sci.*, 59(3):568–581, 1977.

[41] J. B. Lee and S. H. Lee. Dynamic wetting and spreading characteristics of a liquid droplet impinging on hydrophobic textured surfaces. *Langmuir*, 27(11):6565–6573, 2011.

[42] C. D. Modak, A. Kumar, A. Tripathy, and P. Sen. Drop impact printing. *Nat. Commun.*, 11(1):1–11, 2020.

[43] L. Chen, E. Bonaccurso, P. Deng, and H. Zhang. Droplet impact on soft viscoelastic surfaces. *Phys. Rev. E*, 94(6):063117, 2016.

[44] Y. Liu, M. Andrew, J. Li, J. M. Yeomans, and Z. Wang. Symmetry breaking in drop bouncing on curved surfaces. *Nat. Commun.*, 6(1):1–8, 2015.

[45] Z. Yuan, J. Wen, M. Matsumoto, and R. Kurose. Anti-wetting ability of the hydrophobic surface decorated by submillimeter grooves. *Int. J. Multiph. Flow*, 131:103404, 2020.

Nomenclature

A_c : Top area of the cylinder-like shape [m^2]
A_d : Top area of the donut-like shape [m^2]
a : Pillar width or hole width [m]
b : Interval of the pillar or hole [m]
C : VOF function [-]
C_s : Sound speed in water [m/s]
D : Instantaneous spreading diameter [m]
D_0 : Initial droplet diameter [m]
E_{k0} : Initial kinetic energy [J]
E_{s0} : Initial surface energy [J]
E_{sm} : Surface energy at maximum stage [J]
F_Y : Young's force [N]
f_a : Air fraction [-]
f_s : Solid fraction [-]
$\boldsymbol{g}$: Gravitational acceleration [m/s^2]
H_{max} : Maximum penetration depth [m]
h : Pillar height or hole depth [m]
h_d : Thickness of the rim [m]
k : Water hammer coefficient [-]
N_h : Number of wetted holes [-]
P : Pressure [Pa]
P_0 : Ambient pressure [Pa]
P_a : Air pressure [Pa]
P_b : Breakthrough pressure [Pa]
P_C : Capillary pressure [Pa]
P_D : Dynamic pressure [Pa]
P_{hd} : Hydrodynamic pressure [Pa]
P_{hs} : Hydrostatic pressure [Pa]
β : Spreading factor [-]
Δ : Mesh size [-]
η : Penetration factor [-]
θ : Contact angle [°]
θ_a : Advancing contact angle [°]
θ_{app} : Apparent contact angle [°]
θ_C : Contact angle in Cassie state [°]
θ_Y : Intrinsic contact angle [°]
κ : Curvature [1/m]
μ : Viscosity [mPa · s]
ξ : Ratio of top areas [-]
ρ : Density [kg/m^3]
σ : Apparent contact angle [°]
Ψ : Intrinsic contact angle [°]

Subscripts

1 : State 1
2 : State 2
a : Air
l : Liquid
s : Solid
$h1$: Hole 1
$h2$: Hole 2
max : Maximum
MPS : Multi pillar surface
MHS : Multi hole surface

P_{t} : Total pressure [Pa]

P_{WH} : Water hammer pressure [Pa]

ΔP : Pressure difference [Pa]

R : Interface radius [m]

Re : Reynolds number [-]

t_{c} : Contact time [s]

t_{e} : Emptying time [s]

t_{r} : Receding time [s]

t_{s} : Spreading time [s]

u_0 : Initial velocity [m/s]

V : Volume [m^3]

We : Weber number [-]

W_{pin} : Energy loss of depinning [J]

W_{s} : Width of the structure [m]

W_{vis} : Viscous dissipation [J]

Chapter 7

Conclusions

7.1 Summary

To investigate the effect of micro-scale structures on the surface hydrophobicity and droplet wetting state, a coupled level-set and volume of fluid (CLSVOF) method based directional numerical simulation (DNS) was applied. The effectiveness of our numerical method was validated by comparing the numerical results with experimental results. The current numerical models were then extend to the following main tasks.

In Chapter 3, a uniform groove-textured surface was studied. Cases were conducted to evaluate the effect of the groove width and impinging velocity on the surface hydrophobicity and droplet wetting states. Numerical results reveal the following:

1. Droplet spreads freely in the parallel groove direction, but it jumps from the attaching ridge to the next ridge in the perpendicular groove direction (called a "jump-stick"), leading to an elliptical droplet in the top-view.

2. Compared with the non-bouncing behavior of a droplet impinging on a flat surface, droplets completely bounce off when impinging on surfaces with a large groove width, revealing a enhanced surface hydrophobicity.

3. As the groove width increases, the droplet exhibits a shorter spreading factor and shorter contact time, meaning that the surface hydrophobicity is gradually

enhanced. However, it is suppressed with a further increase in the groove width and the impact velocity, because the wetting transition from the Cassie state to the Wenzel state is obtained. This result demonstrates the surface hydrophobicity is weakened in the Wenzel state.

4. The wetting state of the droplet on a textured surface is determined based on the combined effect of the groove width and impact velocity. This finding provides information for following studies.

In Chapter 4, the behavior of an impinging droplet on a surface with a roughness gradient was investigated. The roughness gradient was created by gradually varying the groove width. Simulations were conducted to study the effect of the Weber number (We), the groove depth (D_{G}), and the groove width (W_{G}) on the rebound direction of a droplet. The results obtained from the simulation are summarized as follows.

1. Three types of rebound behaviors (vertical rebound, following, or against the roughness gradient) are observed when droplets impinge on a surface with a roughness gradient. The rebound behavior depends strongly on We, D_{G}, and W_{G}.

2. For an extremely small We, the small difference in contact angles on the left and right sides of the impingement center results in a vertical rebounding of the droplet. When We increases, the water hammer pressure increases, and the droplet rebounds following the roughness gradient owing to the unbalanced Young's force in a Cassie state. However, rebounding in the opposite direction is observed for a larger We due to the coexistence of the Cassie and Wenzel states.

3. The groove depth determines the critical impalement pressure and robustness against a liquid penetration. A larger groove depth and small We result in rebounding following the roughness gradient, whereas the droplet tends to rebound against the roughness gradient for a small groove depth and larger We due to an achievement of the partial Wenzel state.

4. A droplet impingement at a large groove width, that is, a small antiwetting pressure, tends to generate both Cassie and Wenzel states, resulting in rebounding against the roughness gradient.

In Chapter 5, a novel textured surface, with primary structures (higher) used to enhance the hydrophobicity and secondary structures (shorter) to prevent a wetting transition, was proposed. The deformation, penetration, and wetting transition of an impinging droplet on the novel surface were investigated. In addition, the wetting transition mechanism was studied based on the correlation of Laplace's law, Young's equation, and Gibbs extension. The main results are as follows.

1. When compared with the droplet behavior on surfaces masked with only primary structures, the secondary penetration is suppressed such that a stable Cassie state is obtained on surfaces with both primary and secondary ridges.

2. The liquid penetration factor and the emptying time decrease with an increase in the secondary ridge height. The impingement position, at the primary groove or the primary ridge, also plays a vital role in the wetting transition.

3. The increase in the Weber number (We), meaning a larger kinetic energy, leads to the occurrence of a secondary penetration. The value of We also influences the time scales owing to the abrupt change in the solid fraction when a liquid slides down the sidewall of the primary groove and then touches the secondary ridge.

4. The two-step wetting transition found in the numerical results is explained well by theoretical models based on the correlation of Laplace's law, Young's equation, and Gibbs extension.

5. This study provides developing guidelines of superhydrophobic surfaces when considering the stability of a Cassie state, one-step fabrication processes, and fabrication over large areas.

In Chapter 6, the stability of the Cassie state was studied on surfaces with multiple pillars (MPS) and multiple holes (MHS). A pressure analysis was presented to show the

fundamental reason for the liquid penetration and wetting transition. The robustness of the air pocket on the MHS was examined by releasing a droplet with an extremely large Weber number (We). A new model for predicting the maximum spreading factor ($\beta_{\max}$) was derived. The main results obtained are summarized as follows.

1. Compared with the MPS, the MHS not only enhances the surface hydrophobicity but also greatly stabilizes the Cassie state of an impinging droplet.

2. The varying pressure in the air pocket inhibits the depinning of the TPCL. This is the fundamental reason for obtaining a superstable Cassie state on the MHS.

3. Although a large We triggers the depinning of the TPCL in some holes, a significant number of liquid−air interfaces hang between structures, and a Wenzel state is not obtained on the MHS.

4. The new model for the maximum spreading factor ($\beta_{\max}$), considering the air cavity at center of the droplet and the energy loss of the TPCL depinning, is derived based on the law of energy conservation. The new model is in better agreement with experimental and simulation results than previously proposed models.

The findings in this thesis provide insight into the development of smart surfaces to repel water, manipulate the transportation of droplets, and stabilize the Cassie wetting state. Especially, the wetting stability of an impinging droplet on the navel surface and the surface with multi holes is well studied. The robust air pocket in the holes greatly prevents the liquid penetration, leading to a superstable Cassie state on the multi-hole surface, which would be a promising decoration to fabricate robust hydrophobic surfaces.

7.2 Suggestions for future research

Based on the findings in this thesis, we propose the following research to further advance this field.

1. In Chapter 2, we proposed three methods for imposing the contact angle into the boundary condition. Although one of the models was successfully adopted in this thesis, the effectiveness of the other two methods remains unclear. Efforts should be made to compare these three models to find the optimal one.

2. In Chapter 3, the effect of groove width on the surface hydrophobicity was investigated. However, the groove depth also influences the wetting state due to the liquid penetration. To fully understand the liquid behavior on textured surfaces, the depth of the groove or the height of the ridges should be studied further.

3. As described in Chapter 6, although a superstable Cassie state was obtained on surfaces with multiple holes, simulation results show that the droplet rim penetrates into the holes under large impinging velocities, which may induce a loss of the surface hydrophobicity. Future studies should pay closer attention to the robustness and durability of multi-hole surfaces under large impinging velocities.

4. In this thesis, the density ratio between liquid and air is approximately 30, which is much smaller than the real condition of approximately 1000. Because a realistic density ratio is preferable, this limitation should be taken away. Owning to the coarse mesh, the liquid film rupture near the solid surface is observed. To enhance the simulation efficiency, an adaptive mesh refinement scheme is promising.

5. In this thesis, the dynamics and wetting state of a droplet on surfaces with different micro-scale structures were investigated. In practical areas of application, heat transfer often takes place during the liquid-wall interaction, such as a dropwise condensation, evaporation, de-icing, and spray cooling. Hence, future work can focus on a combination of surface wettability and heat transfer.